Radiation Induced Order-Disorder Transformation

R.H. Zee

May 1981

UWFDM-418

Ph.D. thesis.

FUSION TECHNOLOGY INSTITUTE

UNIVERSITY OF WISCONSIN

MADISON WISCONSIN

Radiation Induced Order-Disorder Transformation

R.H. Zee

Fusion Technology Institute
University of Wisconsin
1500 Engineering Drive
Madison, WI 53706

http://fti.neep.wisc.edu

May 1981

UWFDM-418

Ph.D. thesis.

RADIATION INDUCED ORDER-DISORDER TRANSFORMATION

BY

RALPH HING-CHUNG ZEE

A thesis submitted in partial fulfillment of the
requirements for the degree of

DOCTOR OF PHILOSOPHY
(Materials Science)
at the
UNIVERSITY OF WISCONSIN-MADISON
1981

TABLE OF CONTENTS

TABLE OF CONTENTS (continued)

ABSTRACT

RADIATION INDUCED ORDER-DISORDER TRANSFORMATION

Ralph Hing-Chung Zee

Under the supervision of Professor Gerald L Kulcinski

Ordered alloy development is a vital part of of the design of a fusion reactor because of their superior mechanical properties compared to pure materials. The objective of this thesis is to develop a model for the radiation effect on ordered alloys and to conduct a systematic study of radiation induced order-disorder transformation in the ordered CuPd system.

A model for ordered alloys is presented which describes the combined effects of radiation disordering and radiation enhanced-ordering. The model uses the assumptions of Bragg and Williams ordering in a kinetic form. Point defect concentrations are introduced into the kinetics so that the effect of radiation enhanced diffusion can be described. Both time dependent and steady state solutions are presented. All the available data on irradiation of Cu_3Au with fast and thermal neutrons are reviewed. All the curves at a wide variety of temperatures are fitted successfully with the model using the same diffusion parameters throughout. The efficiency of reordering by vacancies is higher at earlier times in the case of thermal neutron irradiation because focussed replacement sequence events are the dominating disordering mechanism.

On the experimental side, CuPd ordered alloy of 52:48 atomic percent composition was irradiated using 14 MeV copper ions, 14.8 MeV neutrons and 1.8 MeV electrons.

In the ion irradiation study, samples were irradiated at the University of Wisconsin tandem accelerator and subsequently analyzed using the transmission electron microscope. Initially ordered CuPd samples were irradiated to doses between 0.05 dpa and 5 dpa from 23°C to 550°C and initially disordered samples were irradiated at 200°C and 250°C to doses of around 3 dpa. Below 200°C, the initially ordered material was completely disordered by such irradiation at a rate of 10^{-3} dpa/sec to doses as low as 0.3 dpa. This disordering process is accompanied by a change in crystal structure from an ordered B2 to a random f.c.c. phase. The disordered material is heavily twinned due to such a transformation. Irradiation of the same alloy above 250°C to a dose of 3 dpa and also at a displacement rate of 10^{-3} dpa/sec did not result in any disorder. Reordering due to vacancy migration is very fast at such high temperatures and dominates over the disordering process. However, an initially disordered sample irradiated at 250°C to 3 dpa remained disordered showing vacancies were still immobile in the disordered state at 250°C. An order dependent vacancy migration energy was proposed to explain such result. A vacancy migration energy for the ordered state of 0.6 eV was obtained by fitting the experimental result using the model. A post-irradiation annealing up to 310°C was conducted on two radiation disordered samples. This result indicates that the reordering process is

heterogeneous in nature similar to classical recrystallization.

Ordered and disordered CuPd samples were irradiated with fusion neutrons at RTNS-II up to a fluence of ~1.8×10^{17} n/cm^2 at 4.3°K. Resistivity measurement was used to monitor the degree of order of the material. The increase in resistivity due to irradiation in the ordered sample was about three times higher than that in the disordered one. A replacement to displacement ratio of 70 was obtained. Results of the isochronal annealing show that the amount of recovery due to interstitial motion depends on the size difference factor in a reversed manner (larger size difference prohibits interstitial reordering). Microscopy samples irradiated under similar conditions did not show any disordered zones.

Results of the 1.8 MeV electron irradiation at 80°K on an ordered CuPd sample gave a replacement to displacement ratio of 2.5. Annealing the irradiated sample at temperatures above 23°C resulted in recoveries of over 100%.

Approved: _____

G. L. Kulcinski

ACKNOWLEDGEMENTS

I would like to dedicate this thesis to my wife, Yvonne, without whose prayer and encouragement, this work would have been impossible.

I would like to extend my sincere appreciation to Professor Gerald Kulcinski, my present advisor, and Dr. Peter Wilkes, who helped initiate this project, for their continual support and guidance. Special thanks are due to Professors Wolfer, Perepezko and Dodd for their invaluable advise.

During the past years, I have also enjoyed the warm friendship of many of my fellow graduate students. Among them, Dr. R. G. Lott, Dr. E. Tjhia, R. W. Knoll, S. K. McLaurin, D. B. Bullen, R. L. Sindelar, D. L. Plumton and J. D. Lawrence deserve my special gratitude.

I am also grateful to Dr. J. H. Billen for his assistance in the irradiations and to the Nuclear Physics group for use of the accelerator. In addition, I would like to acknowledge R. Casper for his memorable friendship.

This work was supported by the Department of Energy under contract number DE-AS02-78ET-52019.

I. INTRODUCTION

A successful first wall material for either a fission or fusion device must be able to maintain good physical properties under severe neutron irradiation conditions. High purity materials have been shown to be unacceptable for such application and complicated alloy systems are believed necessary. Some alloy systems contain intermetallic compounds that may be ordered under thermal equilibrium conditions. Due to their superlattice structures, these ordered systems are well known for their low electrical resistivities[1,2,3] and hence high thermal conductivities. The hardness and ductility of these alloys have also been observed to increase with degree of order[4,5]. The presence of the superstructure tends to reduce the amount of void swelling[6] as well as irradiation induced creep and growth[7,8]. A depression of superconducting transition temperature has also been observed in superconductive alloys due to disordering[9,10]. This could strongly affect the performance of superconducting magnet in fusion systems like magnetic confinement. Therefore it is obvious that a good understanding of the behavior of such ordered phases under irradiation is vital in order to determine the acceptibility of any system for fusion application. At present, there is an urgent need of an unified model to describe such radiation induced order-disorder transformations. Also lacking is a systematic study of the effect of different types of irradiations on the ordered structure of a

particular system and a determination of the effect of damage characteristics on such transformations.

In this study, both the theoretical and experimental aspects of irradiation induced order-disorder transformations will be addressed.

In the theoretical area, the basic formulation of Dienes[11] will be used to develop a phenomenological model for order-disorder transformations under irradiation. The model will describe the variation of order as a function of dose at a given set of irradiation conditions. The intention of this model is to provide a better insight of the mechanisms involved in such a transformation and thus obtain some basic thermodynamic data such as migration energies of the point defects and the ordering energy by applying the model to available experimental results.

On the experimental side, the effect of irradiation on the ordered structure of 52:48 atomic percent copper-palladium system was studied. The alloy was irradiated with three different types of particles, namely 14.8 MeV fusion neutrons, 14 MeV copper ions and 1.8 MeV electrons. These three types of irradiation were chosen because of their different damage characteristics. When the results from these irradiations are compared, it is hoped that they will be able to shed some light on the effect of damage spectrum on disordering. The 14.8 MeV neutron irradiation was performed at 4.3°K followed by an isochronal annealing up to room temperature. The disordering rate due to irradiation as well as the point defect

annealing characteristics was obtained. A similar experiment was done using 1.8 MeV electrons at 80°K for comparison.

Copper-palladium alloy of 52:48 atomic percent composition was chosen because in its ordered state below 600°C, the system forms a CsCl (B2) type superlattice structure. Above this transition temperature, it not only disorders but also transforms into a new face-centered-cubic phase. So it would be of fundamental interest to see whether the ordered B2 phase undergoes an order-disorder transformation under irradiation. If it does disorder, it could be determined whether it maintains its basic body-centered-cubic structure or actually does through a phase transformation and becomes a new f.c.c. phase.

II. REVIEW OF RADIATION DAMAGE IN METALS

The second law of thermodynamics requires a system to minimize its free energy. One of the consequences of this law is that there always exists a certain concentration of point defects (interstitials and vacancies) at temperatures above absolute zero. However, irradiation can produce a supersaturation of such point defects when the energy transferred from the indicent particles to the lattice atoms exceeds a certain critical value. When a lattice atom is knocked out of its equilibrium position, it is called a displacement. The most common unit used in radiation damage to quantify such occurance is displacement per atom (dpa) which is defined as the average number of times each atom is knocked out its lattice site.

The damage structures produced by such high energy particles depend on the nature of the irradiation. Three types of particles are commonly used: neutrons, heavy ions and relativistic electrons. Energetic neutrons and ions are capable of transferring enough energy to the lattice atoms to produce secondary damage. Under such circumstances, it is profitable to study the bahavior of such primary knocked-on atoms (PKA's).

A. Neutron Irradiation

In an elastic collision, a neutron of energy E is capable of transferring to a lattice atom an amount of energy T given by (see e.g. Thompson[12]):

$$T = \Lambda E \sin^2(\Theta/2)$$

$$\Lambda = \frac{4(1+A)}{(1+A)^2} \qquad \text{(II-1)}$$

where A is the atomic mass of the target and Θ is the scattering angle in the center-of-mass frame. The maximum energy transfer, T_{max}, is achieved in a head-on collision given by:

$$T_{max} = \Lambda E \qquad \text{(II-2)}$$

If T_{max} is greater than the threshold energy of displacement E_d^{th}, a Frenkel pair is produced. This threshold energy depends strongly on the crystallographic orientation. For example, in copper, this energy is 23eV in the (100) direction but increases to 40eV in the (111) direction[13].

The probability that an incident neutron of energy E will transfer an amount of energy between T and T+dT to a lattice atom is given by the differential cross section $d\sigma(E,T)$. With an energy dependent neutron flux $\Phi(E)$, the production rate, $P_{PKA}(E,T)$, of PKA with energy between T and T+dT can be written as

$$P_{PKA}(E,T)dT = N\Phi(E)\frac{d\sigma(E,T)}{dT}dT \qquad \text{(II-3)}$$

where N is the number density of the target.

However, the PKA can receive sufficient energy to produce secondary displacements and these can result in large displacement

cascades. Different theories called Secondary Displacement Models have been proposed to calculate the amount of damage due to these high energy PKA's. Torrins and Robinson[14] modified the simple Kinchin and Pease[15] model and suggested the following:

$$\begin{aligned} \nu(T) &= 0 && \text{for } T < E_d \\ \nu(T) &= 1 && \text{for } E_d < T < 2E_d \\ \nu(T) &= \frac{0.8T}{2E_d} && \text{for } T > 2E_d \end{aligned} \qquad \text{(II-4)}$$

where $\nu(T)$ is the number of displacement induced by a PKA of energy T. The factor 0.8 comes from sub-threshold collisions. The displacement energy E_d depends on direction as discussed earier. Therefore, E_d in Equation II-4 should be the average value over all directions. An approximation with $E_d=(5/3)E_d^{th}$ where E_d^{th} is the minimum displacement energy along the easiest direction is generally used[16].

The displacement rate (dpa/sec) can now be written as:

$$K(\text{dpa/sec}) = N \int_0^{E_{max}} \Phi(E)dE \int_{E_d}^{\Lambda E} \nu(T) \frac{d\sigma(E,T)}{dT} dT \qquad \text{(II-5)}$$

So far, only elastic collision events, which dominate at low neutron energy, have been considered. However, when the neutron energy gets above around 1 MeV, other nuclear reactions such as (n,n'), (n,2n), (n,α), (n,p) and (n,γ) become very important. Equation II-5 can be generalized to include all possible reactions that may lead to displacements.

$$K = \int_0^{E_{max}} \Phi(E)\, dE \left\{ \sum_i \int_{E_d}^{\Lambda E} \nu(T) \frac{d\sigma_i(E,T)}{dT}\, dT \right\} \qquad \text{(II-6)}$$

where $d\sigma_i$ is the differential cross-section for the i-th type reaction. This equation is generally written as:

$$K = \int_0^{E_{max}} \Phi(E)\, \sigma(E)\, dE \qquad \text{(II-7)}$$

where $\sigma(E)$ is the total displacement cross-section defined as:

$$\sigma_d(E) = \sum_i \int_{E_d}^{\Lambda E} \nu(T)\, \frac{d\sigma_i(E,T)}{dT}\, dT \qquad \text{(II-8)}$$

In the case of monoenergetic neutron irradiation of thin target where the neutron energy essentially remains constant, the damage rate can be simplified further to the form:

$$K = \Phi\, \sigma_d \qquad \text{(II-9)}$$

This special criterion is satisfied in the fusion neutron irradiation of thin foil at RTNS-II.

Figure II-1 shows the total displacement cross-section as a function of incident neutron energy on copper[17]. Displacement cross-sections of different nuclear reactions are also given. The (n,c) cross-section includes all charged particles reactions such as (nα) and (n,p). Obviously for neutron energies above 2.5 MeV, elastic scattering quickly becomes only a minor contributor to displacement.

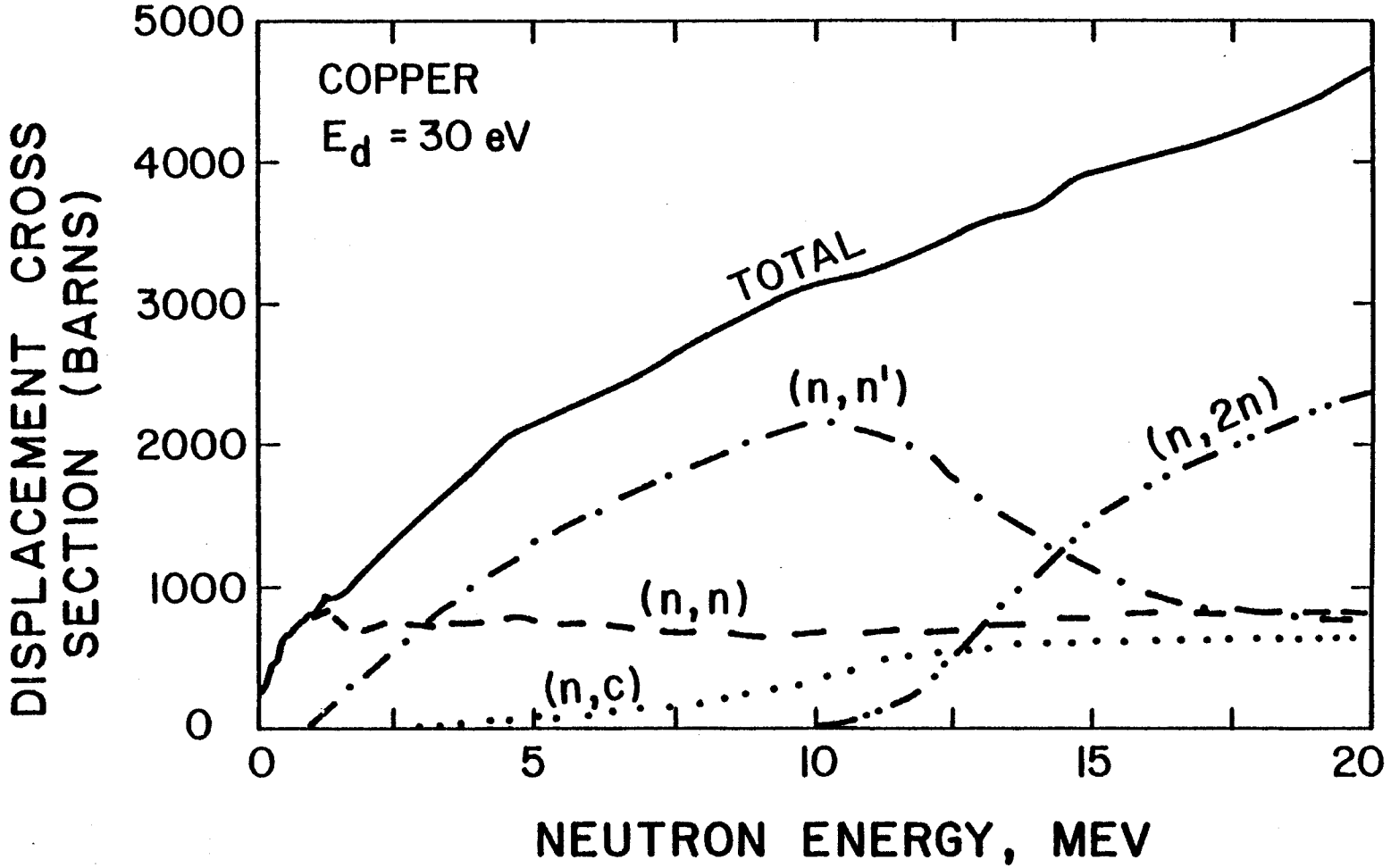

Figure II-1. Neutron displacement cross sections for copper showing contributions from various reactions[17].

B. Ion Irradiation

Effects of neutron irradiation on potential first wall materials for advanced reactors are not well known because of the long irradiation time required to accumulate the necessary damage in existing facilities such as RTNS and EBR-II. Heavy ion irradiation is widely used to simulate damages produced by neutrons. The neutron flux in a reactor typically produces about 10^{-6}dpa/sec. Modern high energy ion accelerators on the other hand are designed to give high beam current. Damage rates as high as 10^{-3}dpa/sec are routinely obtained. Therefore, in terms of displacement damage, ion irradiation is ideal for predicting the behavior of materials over the lifetime of a reactor.

However, extreme care must be exercised in interpreting the results from ion simulation works. Ions do not produce gases such as hydrogen and helium. This is especially critical in a fusion device where (n,α) and (n,p) cross-sections are very high (see Figure II-1). These insoluble gases are very mobile and have been proven to lead to dramatic property changes. Besides, the large difference in damage rates between ion and neutron irradiations can produce misleading data like the temperature shift in void swelling[18]. Both in the theoretical and experimental areas, great advancements have been made to solve these problems.

Ions lose their energy more rapidly than neutrons as they penetrate into the crystal. Therefore they only produce damage in a very narrow region (a few microns) near the surface. This makes the

experimental analysis more tedious. When a solid is bombarded with ions, the incident ions can lose their energy by two different mechanisms. They can transfer energy to the lattice atoms through nuclear interaction which can result in displacements. They can also lose energy by exciting or ionizing the orbital electrons of the lattice atoms. The latter process however will not result in displacement. A thorough theoretical treatment for damage calculation must include both processes.

Lindhard, Scharff and Schiott[19] had developed a theory, commonly known as LSS, for the energy loss of charged particles in a target using an energy partition approach. This model assumes that the nuclear and electronic energy losses are completely separable. It uses the Thomas-Fermi potential to describe the atom and assumes the target is amorphous.

LSS introduced two dimensionless parameters, reduced energy ε and reduced range ρ in their treatment.

$$\varepsilon = E/E_L$$
$$\rho = R/R_L \qquad \text{(II-10)}$$

where

$$E_L = Z_1 Z_2 e^2 \left(\frac{M_1+M_2}{a M_2}\right) \qquad \text{(Lindhard energy)}$$

$$a = 0.8853 \left(\frac{\hbar}{me^2}\right) (Z_1^{2/3}+Z_2^{2/3})^{-1/2} \qquad \text{(Screen length)}$$

$$R_L = \frac{(M_1 + M_2)^2}{4\pi a^2 N M_1 M_2}$$

N = atomic number density of target

M_1, M_2 = masses of incident and target atoms

Z_1, Z_2 = atomic numbers of incident and target atoms

E = incident ion energy

R = range of ion

Using a perturbation method for scattering in a screened coulomb field, LSS obtained an universal differential scattering cross section for nuclear collision given by

$$d\sigma = \pi a^2 f(t^{1/2})\, dt / (2t^{3/2}) \qquad (II\text{-}11)$$

where $t^{1/2} = \varepsilon \sin(\theta/2)$. θ is the center-of-mass scattering angle. Figure II-2 shows the functional dependence of $f(t^{1/2})$ on $t^{1/2}$ calculated numerically by LSS using a screened coulomb potential. Winterbon[20] derived an analytical approximation for $f(t^{1/2})$ given as

$$f(t^{1/2}) = \lambda t^{1/6} [1 + (2\lambda\, t^{2/3})^{2/3}]^{-3/2}$$

with $\lambda = 1.309$

The comparison of this approximation with LSS's exact solution is shown in Figure II-2 indicating the usefulness of Winterbon's result.

Using the reduced parameters, the nuclear stopping power

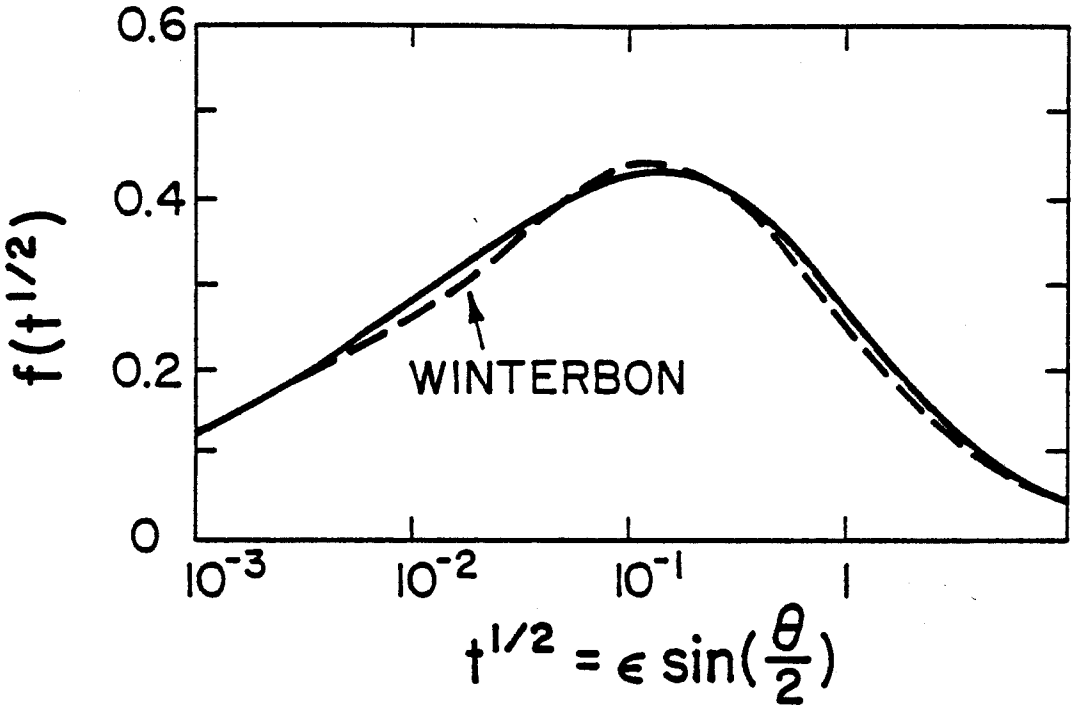

Figure II-2. Reduced differential cross-section calculated from Thomas-Fermi potential. Solid line:LSS numerical result[19]; dashed line: Winterbon's approximation[20].

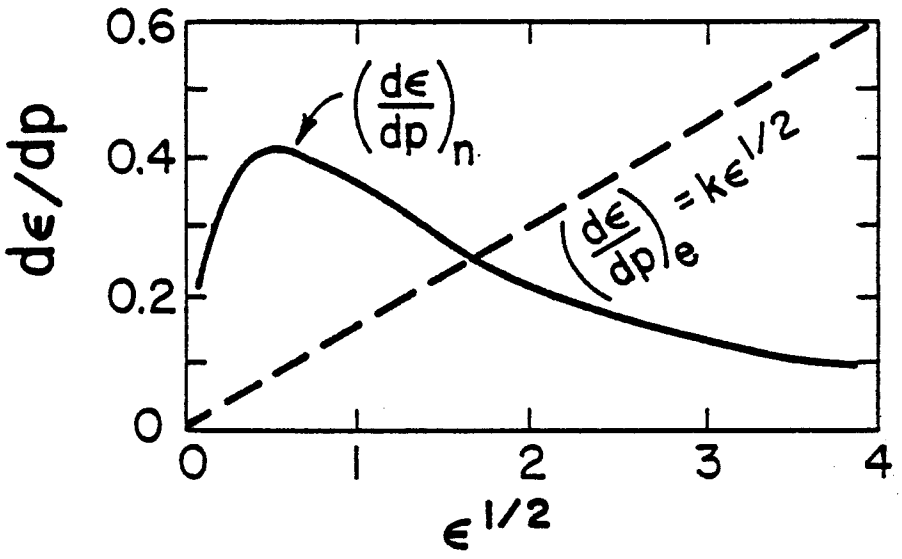

Figure II-3. Theoretical[19] stopping power for nuclear and electronic contributions in reduced units.

can be written as

$$\left(\frac{d\varepsilon}{d\rho}\right)_n = \int_0^E \frac{f(x)}{\varepsilon}\, dx \qquad \text{(II-13)}$$

where $x = t^{1/2}$

One restriction of this theory is that the incident ion energy has to be greater than a certain energy E_{lower} as dictated by the validity of the Thomas-Fermi potential. Values of E_{lower} for a number of systems are tabulated in Table II-1.

Lindhard and Scharff[21] calculated the electronic stopping power using electron-ion interaction theory. They assumed that the electrons in the target are excited in the form of electron gas and only those electrons near the Fermi surface are considered. The stopping power thus obtained is given by

$$\left(\frac{d\varepsilon}{d\rho}\right)_e = k\, \varepsilon^{1/2} \qquad \text{(II-14)}$$

$$\text{where } k = \frac{0.0793\, Z_1^{1/2}\, Z_2^{1/2}\, (A_1+A_2)^{3/2}}{(Z_1^{2/3}+Z_2^{2/3})^{3/4}\, (A_1A_2)^{3/2}}\; Z_1^{1/6}$$

Because of the basic assumption about free electron gas, Equation II-14 is only valid for ion velocity $v < Z_1 e^2/h$, or in terms of energy

TABLE II-1

Energy Limits For Various Ions On Copper And Palladium According To LSS Theory

Ions	E_{lower} (MeV)		E_{upper} (MeV)
	Copper	Palladium	
H	0.0029	0.0053	0.248
D	0.0030	0.0054	0.496
He	0.0063	0.011	2.50
C	0.022	0.037	27.0
N	0.028	0.045	46.5
O	0.033	0.053	63.5
Al	0.064	0.099	205.0
Ni	0.207	0.288	1238.0
Cu	0.224	0.309	1403.0
Nb	0.416	0.540	3261.0
Pd	0.517	0.658	4349.0
Ag	0.536	0.680	4543.0
Au	1.523	1.788	16561.0

$$E_{lower}(MeV) = 3.07 \times 10^{-5} Z_1 Z_2 \, (Z_1^{2/3} + Z_2^{2/3})^{1/2} \, (A_1+A_2)/A_2$$

$$E_{upper}(MeV) = 0.248 \, A_1 Z_1^{4/3}$$

$$E_{upper}(MeV) = 0.248 A_1 Z_1^{4/3} \qquad \text{(II-15)}$$

Figure II-3 shows the variations of the electronic stopping power (Equation II-14) together with nuclear stopping power (Equation II-13) with reduced energy. As the graphs indicates, the electronic contribution dominates at high energies while the nuclear energy loss is important at low energies due to its high interaction rate.

The energy of the ion at any position in the target can be found by integrating the nuclear and electronic stopping power over the distance travelled. Manning and Mueller[22] incorporated the results of LSS into a computer code (EDEP-I) to calculate the damage distribution in a material bombarded with ions. $S_D(x)$, the amount of nuclear energy loss per unit pathlength at a projected depth x is given by

$$S_D(x) = \int_x^\infty f(x')\, S_L[\, E_L(x'-x)]\, \frac{dR(x'-x)}{dx'}\, dx' \qquad \text{(II-16)}$$

where E_L is the average energy of the ions whose projected range is x,

$R(x)$ is the total range measured along the path of an ion,

$f(x)$ is the distribution function of the ion (a Gaussian is assumed).

and $$S_L(E) = N \int_{T_d}^{T_{max}} T\, \eta(T)\, d\sigma(T) \qquad \text{(II-17)}$$

η (T) is the fraction of PKA's energy dissipated in elastic process. Manning and Mueller[22] used the representation of Lindhard[23] for

$$\eta(T) = [\, 1 + k_s\, g(\varepsilon)\,]^{-1} \qquad \text{(II-18)}$$

Robinson[24] approximated $g(\varepsilon)$ as

$$g(\varepsilon) = \varepsilon + 0.40244\, \varepsilon^{3/4} + 3.4008\, \varepsilon^{1/6} \qquad \text{(II-19)}$$

where ε is the reduced energy corresponding to energy T.

The displacement rate K(x) at a depth x into the target can now be calculated using $S_D(x)$.

$$K(x) = \frac{\Phi\ 0.8\ S_D(x)}{N\ 2\ E_d} \qquad \text{(II-20)}$$

where Φ is the ion beam flux in unit of particles/cm^2. The factor 0.8 is the correction necessary for sub-threshold events that do not produce displacement.

As indicated in Table II-1, the upper energy limit for LSS, E_{upper}, theroy is rather low for incident ions lighter than carbon. Manning and Mueller code therefore,would not be applicable for high energy light ions. To solve this problem, Brice[25] had developed a 3-parameter semi-empirical formula for electronic stopping power by fitting experimental data and extended the LSS theory to much

higher energies.

The displacement profile for 14 MeV copper incident on pure copper is computed using the Brice code. The result is shown in Figure II-4 together with the copper ion distribution. The drop in displacement at the surface is due to energy transport by recoil atoms which is an extra feature of the Brice code compared to EDEP-I.

C. Electron Irradiation

Due to the light mass of electron, the PKA energy is so low that it is impossible for it to displace many more atoms in its path. This means that the cascade effect is rather unimportant and mainly isolated Frenkel defects are produced. For an electron to have sufficient energy to displace an atom, relativistic quantum mechanics must be used. It can be easily shown that the energy transfer from an electron of energy E to a lattice atom of mass M with a scattering angle Θ is[12]

$$T = T_{max} \sin^2(\Theta/2) \qquad \text{(II-21)}$$

where $T_{max} = \frac{2E\ (E+2mc^2)}{Mc^2}$

T_{max} being the maximum energy transfer and m the rest mass of the electron.

The cross section for producing primary displacement only

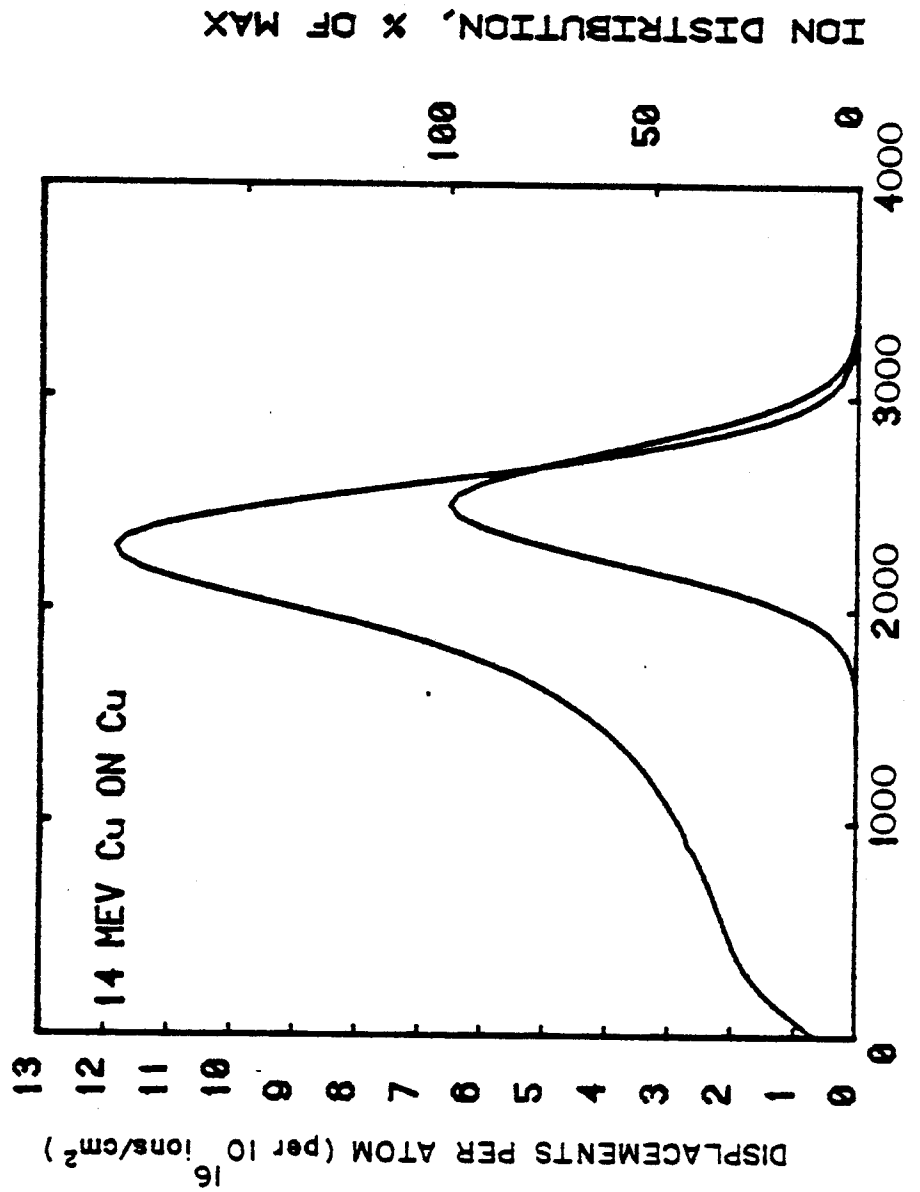

Figure II-4. Displacement profile of 14 MeV copper ions on pure copper as calculated using the Brice code[25]. Included is the ion distribution.

is given by

$$\sigma_p(E,T_d) = \int_{T_d}^{T_{max}} \frac{d\sigma(E,T)}{dT}\, dT \qquad \text{(II-22)}$$

where $d\sigma(E,T)$ is the differential scattering cross-section for an electron of energy E to transfer to a PKA an amount of energy T. The total displacement cross-section including secondary displacements from PKAs is simply

$$\sigma_{Total} = \int_{E_d}^{T_{max}} \nu(T)\, \frac{d\sigma(E,T)}{dT}\, dT \qquad \text{(II-23)}$$

where $\nu(T)$ is the secondary displacement model discussed in the previous section.

N. F. Mott[26-28] solved the Dirac wave equation[29] and obtained an infinite series for the differential scattering cross-section. McKinley and Feshback[30] and Curr[31] used the Mott formulation and arrived at analytical forms for this cross-section. The most commonly used one is that by McKinley and Feshback which has the form

$$\frac{d\sigma}{dT} = \frac{4\pi a_o^2 Z E_R^2}{m^2c^2} \left(\frac{1-\beta^2}{4} \right) \frac{T_{max}}{T} \qquad \text{(II-24)}$$

$$\left\{1 - \beta^2 \frac{T}{T_{max}} + \pi\alpha\beta \left[\left(\frac{T}{T_{max}}\right)^{1/2} - \frac{T}{T_{max}} \right] \right\}$$

where a_o is the Bohr radius ($0.53^{o}A$)

E_R is the Rydberg energy (13.56eV)

$\beta = v/c$

α is the fine structure constant ($Z/137$),

and Z is the atomic number

Oen[32,33] had calculated both the primary and total displacement cross-sections for 37 elements with electron energies from 0 to over 100 MeV using Mott's infinite series. Figure II-5 shows the displcement cross-section for copper with electron energies up to 10 MeV calculated with several different displacement energies. Oen had also compared his results with those of McKinley and Feshback. He found that McKinley and Feshback's approximation severely underestimated both cross-sections for high Z materials at high energies. However for low Z materials, their approximation is relatively good and is widely used.

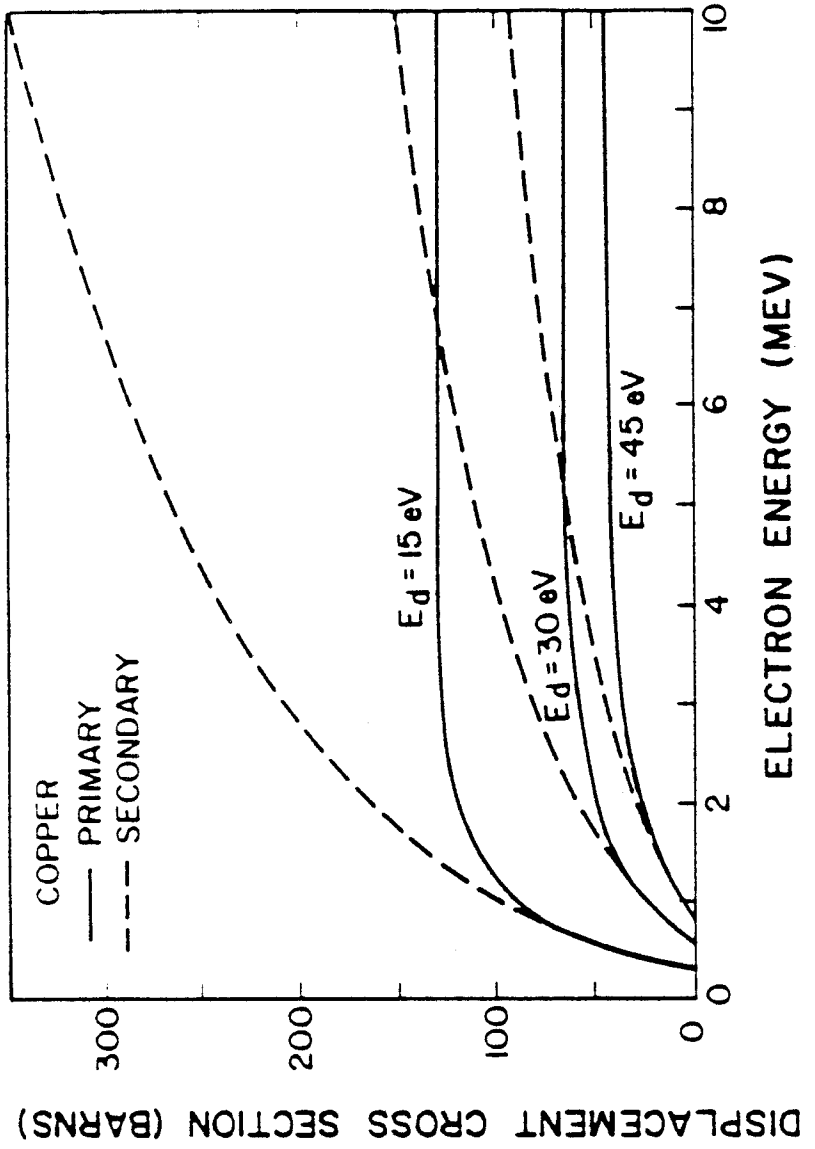

Figure II-5. Variation of primary and total displacement cross sections for copper with electron energy calculated using different displacement energies[32,33].

III. REVIEW OF ORDER-DISORDER TRANSFORMATION AND IRRADIATION EFFECTS

A. Order-Disorder Transformation

Since the discovery of supperlattice lines in Cu_3Au by Bain[34] and in Fe_3Si by Phragmen[35] and the subsequent analysis by Jones and Linde[36], numerous researches have been conducted to gain a better understanding of the superstructure system. Many conferences and a number of excellent review articles have been devoted to this area[37-43]. In most cases, the attention has been focussed on a phenomenon known as "long range order". As its name implies, it describes the macroscopic state of order of the system. In a binary system consisting of A and B type atoms, the ordered structure is made of two distinctive sublattices commonly denoted as α and β sublattices. In the case of perfect order, all the α sites are occupied by A atoms while β by B. When the system is completely disordered, the occupation probability becomes random. A critical transition temperature usually accompanies such transformation. Below this temperature, the system is highly ordered and renders disorder when the critical temperature is exceeded. There is another phenomenon called "short range order" which defines the local state of order. This short range order can exist above the critical temperature when long range order vanishes. Therefore short range order is of particular importance at these temperatures.

Many theories[42-47] have been proposed to predict and explain the formation of such ordered phases. The first of these is also the most widely used one developed by Bragg and Williams[42,43]. They used a thermodynamical approach to consider the state of long range order of a system. As discussed earlier, the long range order parameter, S, is defined such that S is zero when disordered and approaches unity when complete order is achieved. Bragg and Williams wrote S as

$$S = \frac{f_{A\alpha} - X_A}{1 - X_A} = \frac{f_{B\beta} - X_B}{1 - X_B} \qquad \text{(III-1)}$$

where X_A and X_B are the fractions of A and B atoms in the alloy. $f_{A\alpha}$ and $f_{B\beta}$ are the probabilities of finding an A and a B atom in an α and a β site respectively. By considering the atomic jump probabilities of the two types of atoms between their "right" and "wrong" sites, Bragg and Williams arrived at the following relationship:

$$\frac{f_{A\alpha} - f_{B\beta}}{f_{B\alpha} - f_{A\beta}} = \exp\left(\frac{V}{k_B T}\right) \qquad \text{(III-2)}$$

with $V = V_o S$

V is the ordering energy of the system. V_o is a constant. Bragg and Williams considered the ordering mechanism to be a cooperative one. When the system is completely random, all identity

of superstructure is lost and so does the driving force for ordering. Therefore V vanishes. As S approaches unity, the cooperative ordering energy also approaches its maximum value. Using the definition of S in Equation III-1, Equation III-2 can be written as

$$\left[\frac{1}{X_B\,(1-S)} - 1\right]\left[\frac{1}{X_A\,(1-S)} - 1\right] = \exp\left(\frac{V_o S}{k_B T}\right) \qquad \text{(III-4)}$$

Bragg and Williams then expressed the dependence of S as a single variable X

$$S = S(X)$$

where $X = V/kT$ (III-5)

They solved the system of Equations (III-3 and III-4) using the graphical method and obtained the thermal equilibrium values of S as a function of temperature.

Bragg and Williams had also calculated the amount of internal energy associated with ordering by considering the change in energy due to moving a certain number of A atoms to "right" and "wrong" sites. For convenience, they chose this energy E to be zero when S=1 since this corresponded to the state of minimum energy.

$$E(S) = E_o\,(1-S^2)$$

where $E_o = 0.5\,NV_oX_AX_B$ (III-6)

where N is the total number of atoms in the alloy and E_o is the energy required for the complete transformation.

Figure III-1 is a plot obtained by Bragg and Williams for the equilibrium S as a function of temperature in units of RT/E_o. The system chosen in this case is an AB system with $X_A=X_B=0.5$. The curve represented by open circle is from their calculation. The other two curves will be discussed later. S for this case varies continuously from unity to zero. This represents a second degree transformation.

Bragg and Williams had also solved Equations III-3 and III-5 for the AB_3 case. The result is shown in Figure III-2. Contrary to the AB system, this is a transformation of first degree since there is an abrupt drop in S at the critical temperature.

There are two main shortcomings of Bragg and Williams treatment just described. First, it only considers the alloy composition and says nothing about the actual lattice structure. Secondly, it has completely ignored the possibility for the presence of short range order. This short range order as discussed earlier can be very important above the transition temperature where S vanishes. In β-CuZn (β-brass), there is an analomous specific heat above the critical temperature which is due to the presence of short range order.

Seeing this shortcoming of Bragg and Williams, Bethe[44] later developed a theory for short range order using pair-wise interaction. He wrote the total energy of the alloy as

$$E = v_{AA}Q_{AA} + v_{BB}Q_{BB} + v_{AB}Q_{AB} \qquad \text{(III-7)}$$

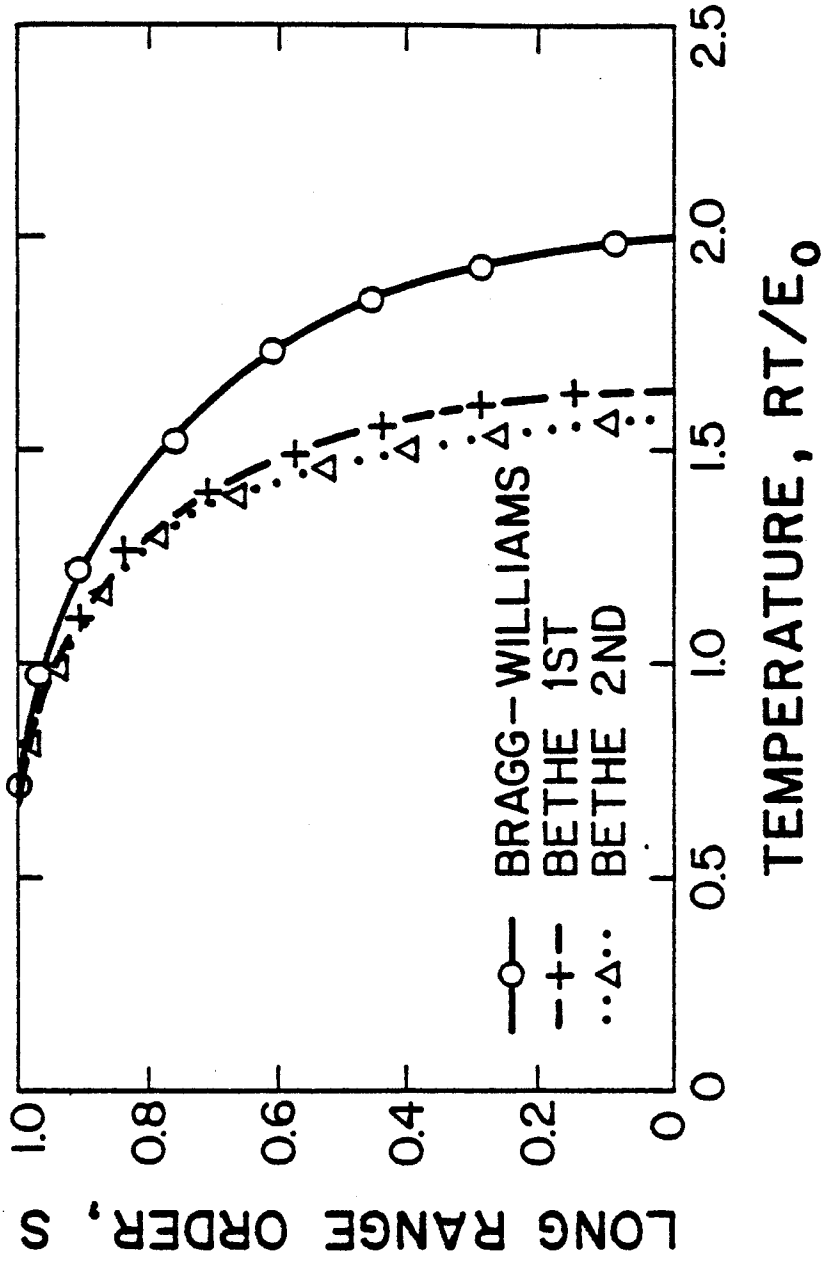

Figure III-1. Thermal equilibrium long range order parameter S for an AB system calculated by various authors.

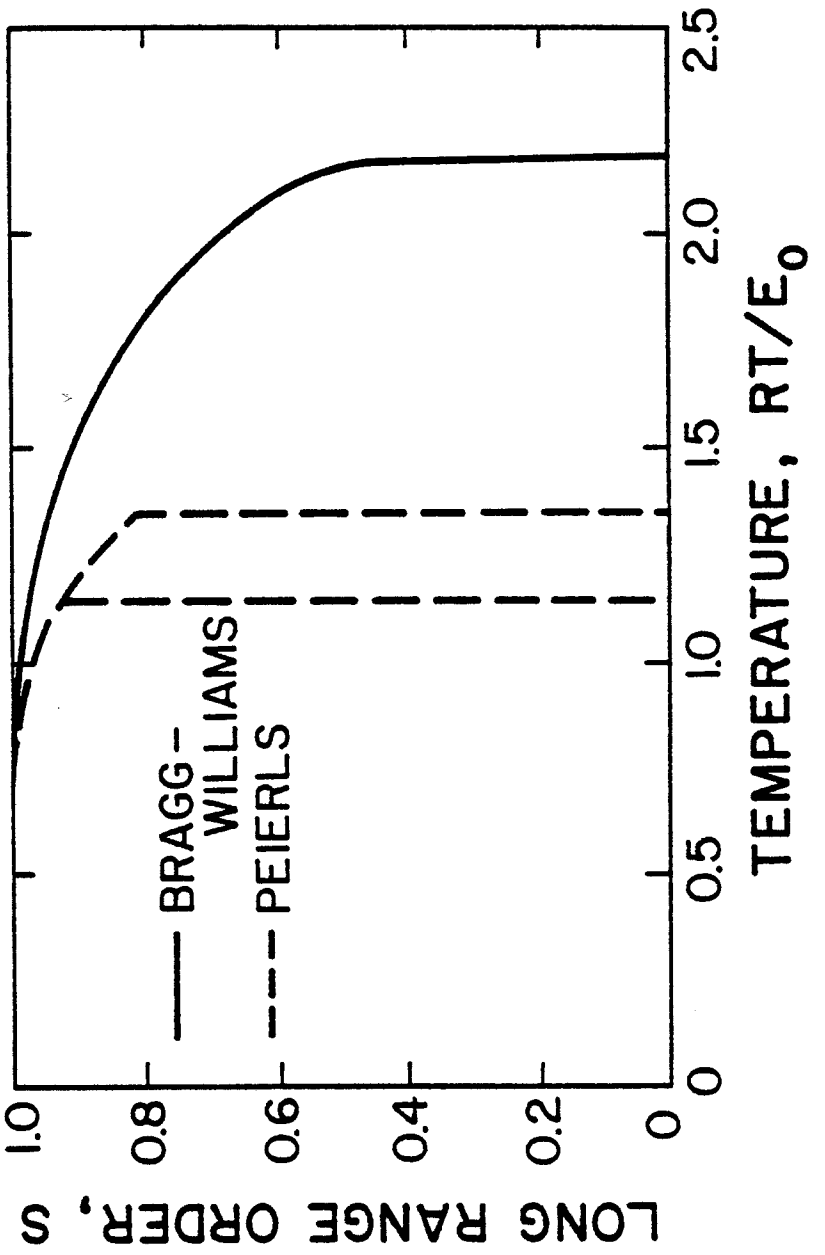

Figure III-2. Same as figure III-1 but for an AB_3 system.

where v_{AA}, v_{BB} and v_{AB} are the potential energies of the A-A, B-B and A-B pairs respectively while Q_{AA}, Q_{BB} and Q_{AB} are the numbers of such pairs. Even though there are three parameters in this equation, only one energy parameter v is important.

$$v = 0.5\ (v_{AA} + v_{BB}) - v_{AB} \qquad \text{(III-8)}$$

Like Bragg and Williams, Bethe has also claculated the energy required for the transformation. This can be written as

$$E_o = E(S=0) - E(S=1) = 0.25\ NZv \qquad \text{(III-9)}$$

where Z is the coordination number. Comparing this with Equation III-6, the following relationship between Bethe's and Bragg and Williams' approaches can be drawn

$$v = 2X_A X_B V_o / Z \qquad \text{(III-10)}$$

For an AB system with CsCl (B2) type superstructure, $V_o=16v$ while $V_o=32v$ for an AB_3 system with f.c.c. structure (Ll_2). Another link can be established between the two treatments in terms of short and long range order parameters σ and S

$$E(\sigma) = E_o\ (1-\sigma) \quad \text{(Bethe)}$$

$$E(S) = E_o\ (1-S^2) \quad \text{(Bragg-Williams)} \qquad \text{(III-11)}$$

and so $$\sigma = S^2 \qquad \text{(III-12)}$$

However experimentally it has been observed that a more realistic relationship is $\alpha > S^2$ because of the presence of antiphase domains.

Bethe had also calculated the long range order parameter as a function of temperature for an AB alloy. Two approximations were used. In the first, he only considered the nearest neighbor interaction whereas he extended it to second shell neighbor in the second one. The results of both approximations for a simple cubic structure (Z=6) are shown in Figure III-1. A similar set of curves can be obtained for the CsCl structure with Z=8.

Peierls[45] used the formulation of Bethe and did a similar calculation for the AB_3 case with a f.c.c. ($L1_2$) lattice. His result is shown in Figure III-2. Due to the complication of this calculation, Peierls was unable to determine the critical temperature exactly and had to settle for a range in which it must lie.

As shown in Figure III-1 and III-2, Bragg and Williams' theory as well and Bethe's predict that the order-disorder transformation in an AB system is always second degree in nature while an AB_3 system is always first. It should be pointed out that this rule should not be treated seriously since many AB systems are known to have first degree transformation (e.g. CuPd[48], MgCd[49], NiMn[50], CuAu[51]). As a matter of fact, most of the order-disorder transformation are first degree in nature. Experimental evidences seem to indicate the following: systems with either or both of their ordered and disordered structures being closed packed generally

exhibit first order transition (e.g. Cu_3Au[52], CuPd[48]). Second degree order-disorder transition normally involves both lattices to be non-closed packed (e.g. CuZn[53]). Nevertheless, this is just an observation and not a rule.

The degree of order of the alloy can be measured by various experimental techniques. The most generally used ones are superlattice reflection intensity[54,55] and electrical resistivity[56-60] methods. Other methods include magnetization measurement[56], change in dislocation spacing[61] and change in thickness fringes[62].

The diffraction intensity method makes use of the extra diffraction spots that arise due to the super-periodicity of the ordered phase. For a CsCl (B2) superlattice, the structure factor for scattering can be written as (see e.g. Cullity[54])

$$F_{fund} = (f_A + f_B) \text{ for } (h+k+l) = \text{even}$$

$$F_{super} = (f_A - f_B)S \text{ for } (h+k+l) = \text{odd} \qquad \text{(III-13)}$$

where h,k,l have their usual meaning in diffraction. Diffraction condition corresponding to F_{super} is generally forbidden in a random situation. Since the intensity of these reflections is proportional to the square of the structure factor, the degree of order S can be measured as:

$$S = [(I_s/I_f)_s/(I_s/I_f)_{s=1}]^{1/2} \qquad \text{(III-14)}$$

where $(I_s/I_f)_s$ is the ratio of the intensity of the superlattice spot to that of the fundamental one at order S. This method is very accurate when applied to x-ray powder diffraction. However, it suffers from the disadvantage that the intensities are also sensitive to orientation. Therefore extra care must be taken when applying Equation III-14 to diffraction of single crystal on the T.E.M.

Methods using resistivity measurement to monitor order will be discussed in chapter IV.

B. Kinetics of Order-Disorder Transformation

There are two distinctive types of kinetic processes with which an disordered system renders order when it is cooled down below the critical temperature. If the degree of order increases continuously and homogeneously with annealing time over the entire alloy, this is known as "homogeneous" or continuous ordering. On the other hand, if ordering proceeds by nucleation and growth of highly ordered domains in a disordered matrix, this is classified as "heterogeneous" ordering. Both types of transformation have been observed experimentally. Superstructured materials such as Ni_4Mo[63], CoPt[64] and FeCo[65-67] have been found to reorder homogeneously. Examples for heterogeneous ordering include Cu_3Au[68], CuAu[69-71], Fe_3Al[72], Cu_3Al[72], CuPt[73,74], NiMn[50,75] and CuPd[48]. Heterogeneous ordering is much more commonly observed than its counterpart. According to classical thermodynamics, a heterogeneous process is

associated with the first degree transformation and homogeneous process with the second degree.

The basic theory for the homogeneous transformation is relatively well developed. Unfortunately not much theoretical work has been done on the heterogeneous ordering process even though it is the generally observed one. In the following sections, models for the two processes will be discussed along with some experimental observations.

1. Homogeneous Ordering

The x-ray result that relates to such transformation is the graduate shifting of the fundamental line positions from the disordered ones to the ordered ones. This is accompanied by a graduate shifting and an increase in intensities of the sharp superlattice lines.

The effort to investigate the kinetic process of which a system orders itself by means of homogeneous ordering was poineered by the work of Dienes[11]. He used the chemical rate theory approach and considered the opposing rates for the ordering and disordering processes. He described the order-disorder transformation as

$$A_\alpha + B_\beta \underset{k_o}{\overset{k_d}{\rightleftharpoons}} A_\beta + B_\alpha \qquad \text{(III-15)}$$

where A_α and B_β denote A and B atoms on α and β sites which

correspond to the ordered condition. K_o and K_d are the rate constants for ordering and disordering reactions. Dienes wrote these rate constants simply as

$$K_o = \nu_o \exp(-U/k_BT)$$

$$K_d = \nu_d \exp[-(U+V)/k_BT] \qquad \text{(III-16)}$$

where U and U+V are the energy barriers for the two opposing reactions. The ordering process is more energetical favorable by an amount of energy V which is the ordering energy. Denoting the number of either site being occupied by the anti-structure (wrong) atoms as X, Dienes obtained

$$\frac{dX}{dt} = \frac{K_d}{(N_A+N_B)} (N_A - X)(N_B - X) - \frac{K_o}{(N_A+N_B)} (X)^2 \qquad \text{(III-17)}$$

where N_A and N_B are the number of A and B atoms in the alloy. Using Bragg and Williams' definition of long range order S and $V=V_oS$, he arrived at an expression for ordering (or disordering) rate as

$$\frac{dS}{dt} = \nu \exp\left(\frac{-U}{k_BT}\right) \{ X_AX_B(1-S)^2 - \exp\left(\frac{-V_oS}{k_BT}\right) [S + X_AX_B(1-S)^2]\}$$

(III-18)

where ν is the attempt frequency. This ordering rate (dS/dt) vanishes at S=0 since the driving force for ordering (V) disappears

at that condition. This implies that the ordering process must be initiated by small fluctuation. This is in agreement with the assumption that ordering is a cooperative phenomenon.

The thermal equilibrium degree of order can be obtained by setting Equation III-18 to zero. The result obtained this way agrees with that from Bragg and Williams. Dienes also found that the transformation of the AB system is associated with a second order transformation while AB_3 with first as Bragg and Williams did. This is not surprising since the basic assumptions used in both theories are identical.

The basic differential equation for ordering by Dienes (Equation III-18) is of a second order non-linear type and does not have an analytical solution. Nowick and Weisberg[76] expanded this equation using the Taylor series up to third order and obtained an analytical solution as

$$\frac{1 - S}{1 - S_e} = \left\{ \begin{matrix} \coth \\ \tanh \end{matrix} \right\} (\alpha t + \beta) \qquad \text{(III-19)}$$

where S_e is the thermal equilibrium order and t is of course time. The coth function applies when $S < S_e$ (ordering) and the tanh function when $S > S_e$ (disordering). β is the constant of integration. Treating α as the rate constant, Nowick and Weisberg arrived at an approximated formula for at large S or low temperatures

$$\alpha = \nu (X_A X_B)^{1/2} \exp[-(U+V_0/2)/k_B T] \qquad \text{(III-20)}$$

Rothstein[77] also had obtained a similar rate constant

Vineyard[78] on the other hand attacked the same problem from a different angle. He used a statistical method starting with a set of distribution probability and ended up with two sets of similar results. The first set is for ordering with pair exchange mechanism just like Dienes did. The second set uses vacancy diffusion as a mean for ordering. For the former case, he obtained

$$\left.\begin{matrix} K_o \\ K_d \end{matrix}\right\} \sim 8\nu \exp\left[(-U \pm 7vS)/k_B T\right] \quad \text{for AB case}$$

$$\left.\begin{matrix} K_o \\ K_d \end{matrix}\right\} \sim 12\nu \exp\left[(-U \pm 3vS)/k_B T\right] \quad \text{for } AB_3 \text{ case} \qquad \text{(III-21)}$$

Comparing this with Equation III-16, one finds that $V_o=14v$ and $V_o=6v$ for AB and AB_3 cases respectively.

As mentioned earlier, there are only a few ordered systems that transform homogeneously. But since all these theoretical treatments employ a phenomenological approach, some idea of activation energy for reordering can be obtained by applying these models to existing experimental data even though the detailed reordering mechanisms are quite different.

Dienes[11] applied his model to the CuZn (β -brass) and Cu_3Au systems and suggested that the Bragg Williams ordering energy should have the form $V=V_o(S+0.5S^3)$ instead of $V=V_oS$ in order to obtain a better fit to the experimental data at equilibrium.

Before Dienes developed his model, he used a even simpler approach to study the ordering kinetics. He[79] used the equation

$$\frac{dS}{dt} = K(1 - S)^{\gamma} \qquad \text{(III-22)}$$

where K is again the rate constant and γ determines the order of reaction. He applied this to a resistivity experiment on CuAu and determined the activation energy to be 1.24eV with γ =3 (third order).

Quimby and Weisberg[80] used the approximation of Nowick and Weisberg (Equation III-19) and determined the reaction rate constant α from an ordering experiment at elavated temperatures on Cu_3Au by measuring the Young's modulus of a quenched wire. They obtained an activation energy defined by Equation III-20 as $U+1/2V_0$ to be around 2eV. Feder, Mooney and Nowick[96] using precision lattice parameter measurement method also on Cu_3Au obtained an agreeing 2.08eV for the same activation energy.

A similar experiment using x-ray diffraction technique was performed on Ni_3Mn by Kirk and Cohen[81]. They found the rate constant α (Equation III-19) to be related to an activation energy of 2.5eV. A similar value of 2.5eV was obtained by Wolfe[75] in NiMn.

It should be noted that the activation energy (Q) obtained by such phenomenological analysis consists of three independent terms. In the case of reordering by vacancy migration, this energy includes the formation energy and migration energy (self diffusion) of vacancies as well as half the ordering energy (0.5V).

The results above, with the exception of Dienes, give an activation energy Q around 2.2eV.

Brinkman, Dixon and Meechan[82], by separating the formation and migration energies in Q, obtained an estimated migration energy of vacancies to be 1.19eV in Cu_3Au. This is in good agreement with migration energy of vacancies in pure materials. Brinkman in the same analysis also arrived at a vacancy formation energy of 0.88eV. This set of energy values together with a Q of 2.3eV gives an ordering energy V of about 0.3eV in good agreement with that obtained by Bragg and Williams.

Buckley[66-68] had studied the ordering mechanism by annealing previously quenched FeCo alloys. He found by using x-ray and T.E.M. methods that this alloy reordered homogeneously at temperatures between 500 and 600^{o}C. This process was then followed by domain coalescence.

Okamoto and Thomas[63] used T.E.M. and F.I.M . techniques to study the ordering kinetics of Ni_4Mo. They also saw a continuous change with no evidence of nucleation and growth of ordered domain taking place. Ralph[64] had also observed similar experimental result in the initial ordering stage of CoPt. These are some of the few experimental evidences indicating the occurence of homogeneous ordering.

2. Heterogeneous Ordering

This type of ordering mechanism is analogeous to classical nucleation and growth. The x-ray result that relates to such a process is the simultaneous appearance of discrete fundamental lines of both the ordered and disordered states along with an increase in intensity of the superlattice lines at fixed positions.

Not much theoretical work has been done in this area. Rudman[83] used the kinetic theory of recrystallization of Turnbull[84] and treated the ordered domain growth as grain growth. He obtained an expression for growth rate G as

$$G = \frac{ea}{h} \Delta F(T)\ C_v \exp \frac{-E_m + T S_D}{k_B T} \qquad \text{(III-23)}$$

where e is the base nature logarithm and a is the lattice parameter. E_m and S_D are the energy and entropy for diffusion. $\Delta F(T)$ is the free energy change for disordering at temperature T. In this model reordering is assumed to be due to vacancy motion and therefore G is directly proportional to the concentration of vacancy C_v.

Even though the theoretical treatment for such ordering mechanism is not well developed, extensive experimental results have been obtained that are related to such transformation. Marcinkowski and Zwell[68] had used the T.E.M. technique to study the ordering effect of Cu-Au alloys close to Cu_3Au composition. They found definite evidence of a two phase region in the phase diagram. The

existance of such region indicates that the transformation belong to that of classical nucleation and growth. Tong and Wayman[69] had seen similar result on ordering of CuAu film.

As mentioned earlier, Buckley[65-67] found that the FeCo system underwent homogeneous ordering at temperatures between 500 and 600°C. However, he also noticed that the same system reordered by nucleation and growth of ordered domains at grain boundaries at lower temperatures. This example examplifies the complexity of the mechanisms involved in ordering.

Fe_3Al alloy also exhibits first degree transformation with nucleation and growth as the main reordering path. Lutjering and Warlimont[72] observed ordered nuclei of Fe_3Al forming in the disordered matrix after proper heat treatment. They saw identical result with Cu_3Al system as well.

C. Order-Disorder Transformation Under Irradiation

Since it was shown by Siegel[85] more than thirty years ago, that neutron irradiation could disorder ordered Cu_3Au, many experiments had been directed at the area of radiation induced order-disorder transformation. Many reviews and conferences have been devoted to the understanding of such phenomenon[83,86]. The results of these extensive investigations show that irradiation can either disorder or reorder the alloy system dependent upon the instantaneous degree of order and other irradiation parameters such as temperature, dose rate and type of irradiation. Due to the inherent complication of such alloy systems,

all the basic parameters such as formation and migration energies of point defects are not as well defined as in the case for pure materials. Therefore, in almost all cases, a phenomenological approach had to be taken.

Liou and Wilkes[87] used the approximation Nowick and Weisberg[76] made of Dienes'[11] theory for an irradiation situation. They assumed that the reordering process was controlled by the diffusion of vacancies which was enhanced by irradiation. The degree of order of the system under irradiation as a function of time is given by:

$$S(t) = 1 - p + \frac{p - q}{1 - \frac{S_o+q-1}{S_o+p-1} \exp(Zt)} \qquad \text{(III-24)}$$

where

$$Z = \varepsilon^2 K^2 + 4x[x + \varepsilon K/(1 - S_e)]^{1/2}$$

$$p = (-\varepsilon K + Z)(1 - S_e)/(2x)$$

$$q = (-\varepsilon K - Z)(1 - S_e)/(2x)$$

where ε is the replacement to displacement ratio and x is the reaction rate constant. K is the displacement rate and S_e is the equilibrium long range order parameter. The rate constant depends strongly on the concentration and mobility of vacancies and they obtained the following expression for x

$$x = \nu \left(\frac{X_A}{X_B}\right)^{1/2} (Z_\beta/2)(Z_\alpha+Z_\beta-2) C_v \exp(-E_m^v/k_BT) \exp(-V_o/2k_BT) \qquad \text{(III-25)}$$

C_v is the concentration of vacancies under irradiation and V_o is the ordering energy. E_m^v is the vacancy migration energy.

Zee and Wilkes[88-90] later used the same assumption and solved the differential equation of Dienes[11] (equation III-18) numerically. This model will be discussed in detail in the next chapter. Butler[91] had worked along the same line for electron irradiation since his main interest was in HVEM. The result he obtained was very similar to those discussed above.

The second law of thermodynamics requires that any alloy system to minimize its free energy. An ordered inter-metallic compound may be stable with other phases due to its low free energy in its ordered state. However, irradiation can disorder the order phase resulting in a new steady state value of order which may be quite different from the thermal equilibrium value. Under this condition, the free energy of the ordered phase may increase. A new free energy balance between the adjacent phases will be established which may cause a modification of the phase diagram.

Liou and Wilkes[87] had used the expressions for free energy as a function of S obtained by Guggenhiem and Tagaki[92-94] for the CsCl structure and McGlashan[95] for the $L1_2$ structure and calculated the new free energy of the ordered phase at the steady state value of S under irradiation at different temperatures. They also assumed that irradiation did not affect the free energies of the surrounding phases which did not possess any superlattice structure. Figure III-3 shows the computer calculation for the phase diagrams of the Ti-Ru system with

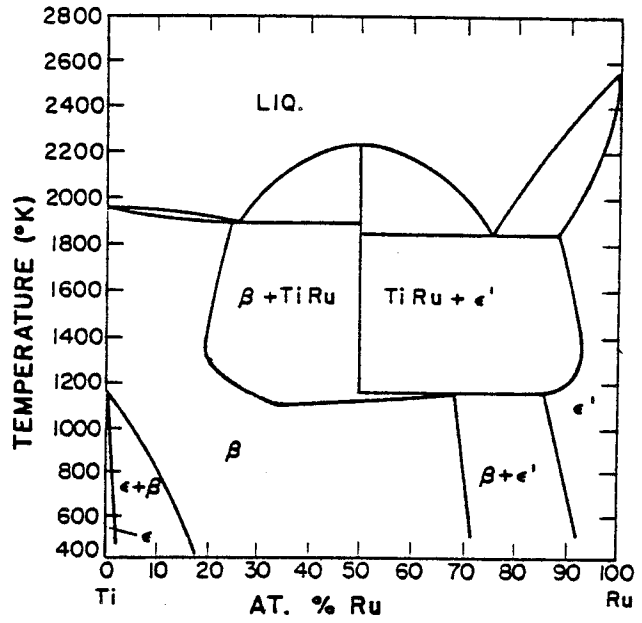

Figure III-3a. The phase diagram for Ti-Ru system as modified by irradiation at a rate of 10^{-3}dpa/sec with $\varepsilon = 10$. A constant sink density of $10^{11}/cm^2$ is used.

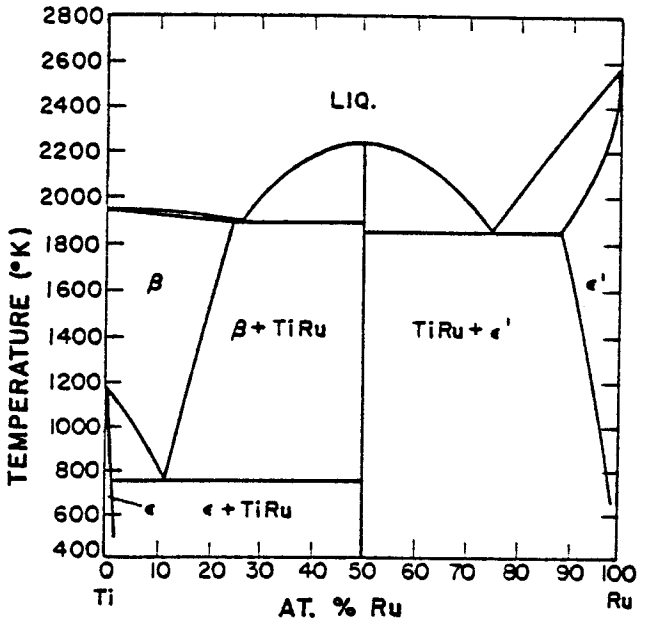

Figure III-3b. Same as 3a but at thermal equilibrium.

and without irradiation. At a displacement rate of 10^{-3}dpa/sec, irradiation disorders the ordered TiRu phase at temperatures below 1100^{o}K and raises its free energy above the common tangent of the and ε' phase. A new two phase region of ($\beta + \varepsilon'$) also appears. Irradiation has little effect at higher temperatures due to high reordering rate.

On the experimental side, Schulson[86] had written an excellent review in this area of order-disorder transformation induced by irradiation. Table III-1 gives a summary of the experimental work in this area. This table is by no means exhaustive. However, it does represent the main highlights in this vast field.

It is now well accepted that point defect migration is the main mechanism for reordering. Therefore, main interest in order-disorder transformation under irradiation lies in three different temperature regimes: low, high and intermediate. At low enough temperature where point defects are immobile, radiation can only disorder the superlattice structure. At high temperature where point defects are mobile but vacancy concentration is still rather low, irradiation can produce excess vacancies and hence enhance reordering. At intermediate temperature, both disordering and reordering processes occur simultaneously and a balance between the two processes is established.

Irradiation disordering was first discovered by Siegel[85] by irradiating initially ordered Cu_3Au with fast neutrons at 310^{o}K. He found that the order had almost completely disappeared at a dose of about 0.1dpa. His observation was made using resistivity measure-

TABLE III-1

Summary of Experiments on Order-Disorder Transformation Under Irradiation

Alloy	Irrad. Particles	Irrad. Temp.(K)	Max. Fluence	Analy. Techn.	Ref.	Observations
Cu_3Au	.05MeV Neutrons	313	3.3×10^{19} n/cm^2	ρ	85	ρ increases (disordering) in ordered sample. No change in initially disordered sample.
	Fast Neutrons	473	2×10^{18} n/cm^2	ρ	58	ρ decreases (ordering) in disordered sample.
	Thermal-Fast Neutrons	423	2×10^{17} n/cm^2	ρ	97	ρ decreases in partially ordered sample. Reordering rate is proportional to thermal neutron flux.
	Fission Neutrons	308-379	7×10^{18} n/cm^2	ρ	98	ρ increases in ordered sample. No change observed in disordered sample.
	Fast Neutrons	4	10^{18} n/cm^2	ρ	56	ρ increases linearly with neutron fluence.
	Fast Neutrons	423	10^{18} n/cm^2	ρ	56	ρ initially decreases then increases with fluence.
	Thermal Neutrons	308	5×10^{17} n/cm^2	ρ	56	ρ decreases with fluence (ordering).

TABLE III-1 (cont.)

Alloy	Irrad. Particles	Irrad. Temp.(K)	Max. Fluence	Analy. Techn.	Ref.	Observations
Cu_3Au	Thermal Neutrons	353	$5x10^{18}n/cm^2$	ρ	59	ρ of ordered sample decreases initially and then increases while disordered sample decreases.
	Thermal Neutrons	308-379	$10^{18}n/cm^2$	ρ	98	ρ of disordered sample decreases; ρ of ordered sample increases.
	Fast Neutron	4	$10^{16}n/cm^2$	ρ	102	ρ increases with fluence; Isochronal annealing shows large recovery at above 300°K.
Cu_3Au	1 MeV Electrons	88	$3.4x10^{19}e/cm^2$	ρ	101	No change in ρ during irradiation. Anneal at 300°K shows slight recovery.
	1 MeV Electrons	333	$10^{18}e/cm^2$	ρ	101	No change in ρ during irradiation at 333°K. 3% recovery after 373°K anneal.
	1 MeV Electrons	310	$3x10^{17}e/cm^2$	ρ	60	No change in ρ during irradiation. Small recovery by annealing at 373 and 403°K.
	1,1.5MeV Electrons	20	$10^{18}e/cm^2$	ρ	102	ρ increases in both ordered and disordered samples. Isochronal annealing to 480°K shows peaks and over 100% recovery.

TABLE III-1 (cont.)

Alloy	Irrad. Particles	Irrad. Temp.(K)	Max. Fluence	Analy. Techn.	Ref.	Observations
Cu_3Au	33 MeV Alphas	93 & 493	----	ρ	103	ρ increases in both temp. irradiations of two ordered samples. Disordering rate is 6 times higher at low temperature one.
	9 MeV Protons	173	$5x10^{21} p/m^2$	ρ	82	ρ increase in ordered sample due to irradiation is 6 times higher than disordered. Small recovery to 130°K annealing
	5-100KeV Cu ions	300	$10^{11}/cm^2$	TEM	104 105	Disordered cascades observed.
	Fission Neutrons	300	$10^{17} n/cm^2$	TEM	106	Disordered cascades observed.
	Fusion Neutrons	300	$2x10^{16} n/cm^2$	TEM	106	Disordered cascades observed.
CuZn	Fast Neutrons	4	$10^{16} n/cm^2$	ρ	100	Increase in ρ due to irradiation. Isochronal anneal shows peaks at 120 and 300°K.
	1.5 MeV Electrons	20	$4.5x10^{17} e/cm^2$	ρ	107	ρ increase is large compared to pure material during irradiation. Annealing peaks at 40, 65, 90°K followed by continuous annealing.

TABLE III-1 (cont.)

Alloy	Irrad. Particles	Irrad. Temp.(K)	Max. Fluence	Analy. Techn.	Ref.	Observations
CuZn	33 MeV Alphas	173	$23uAhr/cm^2$	ρ	108	ρ increases linearly with dose. 100% recovery after annealing to 300°K.
Ni_3Mn	Thermal Neutrons	5	$10^{18}n/cm^2$	M	56	Disorder by [110] replacement sequences, 130repl/450eV recoil.
	Fast Neutrons	5	$10^{18}n/cm^2$	M	56	Disorder by random cascade mixing 8800replacement/200eV PKA.
	.5-3MeV Electrons	10	$5x10^{17}e/cm^2$	M, ρ	57	Disorder by irradiation. 2.2 repl per displacement.
Zr_3Al	1 MeV Electrons	130-775	44dpa	TEM	55	Completely disordered at 1dpa at temperatures below 375°K. Intermediate order obtain at 575-775°K after few dpa.
	0.5-2MeV Ar ions	30-693	28dpa	TEM	111 112	Complete disordered after 3dpa at below 693°K. Transition to amorphous at low temperatures.
	0.5-2MeV Ar,C,N	30-850	28dpa	TEM	113	Disordered zones observed. Fluence required to completely disorder the structure is proportional to temperature. Same is true for transition to amorphous state.

TABLE III-1 (cont.)

Alloy	Irrad. Particles	Irrad. Temp.(K)	Max. Fluence	Analy. Techn.	Ref.	Observations
Zr_3Al	0.5-2MeV Ar ions	40-753	28dpa	TEM	6	5% swelling due to lattice parameter change by disordering. Transition to amorphous state.
	1 MeV Electrons	320	1dpa	TEM	6	Same as above.
Ni_4Mo	1 MeV Electrons	450-900	40dpa	TEM	114 115	Radiation induced enhanced reordering observed.
	1 MeV Electron	673	10^{21} e/cm^2	TEM	116	Radiation induced enhanced reordering observed.
FeAl	1.25 MeV Electrons	436-591	10^{21} e/cm^2	TEM	62	Length of [111] replacement collision sequence is about 7.
	Fission Neutrons	25	2×10^{18} n/cm^2	ρ	117	Disorder due to irradiation. 15% recovery below 300°K. 80% recovery below 550°K.
FeNi	Fast Neutrons	568	3×10^{19} n/cm^2	M	118	Radiation enhanced reordering.

TABLE III-1 (cont.)

Alloy	Irrad. Particles	Irrad. Temp.(K)	Max. Fluence	Analy. Techn.	Ref.	Observations
Ni_3Al	1 MeV Electrons	144-775	26dpa	TEM	119	Complete disordered at 1dpa below 250°K. Intermediate S attained from 313-440°K. No disorder seen at high temperatures. Void at 26dpa at 775°K.
U_3Si	Neutrons	333	0.1 - 1dpa	D_x	120	Radiation induced volumatric change due to disordering. Annealing from 250 to 500°C results in complete reordering.
	Neutrons	373	$7x10^{17}$ fission/cm^3	D_e	121	Complete transition to amorphous at 10^{17}fissions/cm^3. Annealing above 500°C recovers the order.
	2 MeV Ar ions	333	$10^{17}/cm^2$	D_x	122	Complete disorder at 10^{15}ions/cm^2.
Nb_3Sn	Fission Fragment.	313	$2x10^{15}/cm^2$	D_x	124	Complete disordered due to irradiation. Complete recovery at 1070°K.
	25 MeV Oxygen	30	$10^{17}/cm^2$	T_c	9	Lowering of T_c from 12°K to 1°K due to irradiation.

TABLE III-1 (cont.)

Alloy	Irrad. Particles	Irrad. Temp.(K)	Max. Fluence	Analy. Techn.	Ref.	Observations
V_3Ga	Fast Neutrons	333	10^{19} n/cm^2	T_c	125	Linear suppression of T_c with dose and over 100% recovery of T_c at 773°K.
Nb_3Ge Nb_3Sn	Fast Neutrons	20	10^{18} n/cm^2	T_c, ρ	123	Increase in ρ and suppression of T_c due to irradiation disordering. Recovery in T_c and above 280°K.
Nb_3Ge Nb_3Sn	Fission Fragment	65	5×10^{20} n/cm^2	T_c, ρ	123	Increase in and decrease in T_c due to irradiation. No recovery up to 425°K.
Nb_3Ga Nb_3Ge Nb_3Al Nb_3Pt Nb_3Sn	Fast Neutrons	423	10^{20} n/cm^2	T_c, D_n	10 126	All samples shows suppression of T_c and order with dose. Start to show recovery between 673 and 773°K.

Anaylsis techniques: ρ - Resistivity, M - Magnetization, D_x - X-ray diffraction, D_n - Neutron diffraction, T_c - Superconducting transition temperature.

ment. Carpenter and Schulson[55] irradiated ordered Zr_3Al with 1MeV electrons in the HVEM and found that at temperatures below 320°K, the superstructure was completely destroyed at around 1dpa. Howe and Rainville[111] also irradiated Zr_3Al but using Argon ions at 30-40°K. They found similar disordering effect except complete disorder was attained at a lower dose of 0.3dpa. Sweedler and Cox[10], using neutron diffraction technique, noticed that Nb_3Al could be disordered by bombarding it with fast neutrons at temperatures as high as 413°K to a dose of 0.1dpa. Numerous experiments have yield similar result. In monitoring the decrease in S in Ni_3Mn with neutron fluence, Aronin[110] had fitted his result to an exponential decay curve governed by:

$$S = S_0 \exp (-A\Phi t) \qquad \text{(III-26)}$$

where S_0 is the initial degree of order and Φ is the neutron flux and t is irradiation time. A is a parameter related to the efficiency of disordering. Other authors had also successfully fitted their disordering data using this simple expression.

Experimental evidence for radiation induced reordering is also well documented. Glick[59] and Cook[98] independently irradiated ordered and disordered Cu_3Au with reactor spectrum neutrons at about 350°K. Both observed that the resistivity of the disordered sample decreased (indicating an increase in S) while the resistivity of the initially ordered sample increased. However, Cook and Cushing also found that fast neutron irradiation did not enhance reordering even

in the disordered specimen. Blewitt and Coltman[58] also showed that fast neutron irradiation could enhance reordering in a disordered Cu_3Au sample but at a higher temperature of 423°K. They found that the reordering rate under such irradiation was 10,000 times higher than expected thermally. These results show that both thermal and fast neutrons are capable of enhancing reordering but the former one is more effective at lower temperatures due to different damage characteristics of the two irradiations.

Adams[60] and Dixon[101] had independently irradiated ordered Cu_3Au with 1MeV electrons at temperatures of 315°K and 333°K respectively. Both irradiations reached a maximum dose of around 10^{-5}dpa. They recorded no change in order due to irradiation. But a post-irradiation anneal at 373°K resulted in a resistivity value lower than that obtained by thermal treatment without irradiation. Electrons are not very effective in producing disorder. However, such irradiation does produce an excess of vacancies and at temperatures where these vacancies are mobile, they migrate and produce "excess" order.

Evidence of radiation induced reordering has also been found in superconducting A-15 alloys. For instance, Francavilla[125] found that T_c (transition temperature to superconducting state) increased from 14.1 to 14.5°K upon fast neutron irradiation at 333°K to 0.01dpa followed by annealing above 773°K.

At intermediate temperatures where reordering and disordering rates are of the same magnitude, intermediate degree of order can be reached under irradiation. Such phenomenon has been predicted by

various theories[87,91] and confirmed by experimental evidence. Kirk[56] and Cook[98] irradiated Cu_3Au at around 150°C and 100°C with fast neutrons and found that the degree of order of the material had levelled off to an intermediate steady state value.

Carpenter and Schulson[55] found that when their Zr_3Al was irradiated with 1 MeV electrons in the HVEM at temperatures above 575°K, it also reached a steady state degree of order. Howe and Rainville[112] also irradiated Zr_3Al but with high energy argon ions and found similar effect. But they showed that with ion irradiation, a higher temperature was required for the order system to reach a non-vanishing steady state order value compared to electron irradiation. This is because of cascade effect. In ion irradiation, a large percentage of vacancies are trapped in the cascade zones thus preventing them to migrate. In electron irradiation, isolated vacancies are produced. These vacancies are free to move and therefore very effective in reordering.

IV. MODEL FOR RADIATION INDUCED ORDER-DISORDER TRANSFORMATION

A. Introduction

Experiments have shown[97-126] that during irradiation, previously stable alloys may undergo phase transformations. Second phase particles may dissolve or new ones form. One mechanism that has been proposed to explain phase dissolution is radiation disordering[87-90]. It has been demonstrated that the free energy change involved in this process is often comparable to the free energy of formation of alternative phases and irradiation modified phase diagrams have been calculated on this basis. The process of radiation disordering has long been known to occur and has recently been reviewed[90]. However, enhanced radiation ordering is also a common observation so that the situation is evidently not simple. A model which permits calculation of both ordering and disordering rates under irradiation has recently been proposed[87] and it is the purpose of this chapter to apply this model to all the available data on irradiation of Cu_3Au. This system has been irradiated more than any other ordered alloy in the literature and good thermal ordering data is also available.

We demonstrate here that all the available data can be satisfactorily fitted with this model, using the same parameters for the diffusional behavior of the alloy throughout.

B. The Radiation Disorder Model

When an energetic particle interacts with the lattice atoms of a metal to produce a cascade of displacements, it is well known that many point defects are produced. In the process, many more atoms can change position (replacements) than are displaced to produce Frenkel defects. In an ordered alloy, such replacements may produce disorder. This disorder can make cascade regions visible in the electron microscope[104-106].

In addition to these local cascade replacements, replacement collision sequences can also produce disorder. This occurs when a chain of atoms is displaced forward leaving a vacancy behind and an interstitial at the forward end. Since each atom moves one atomic jump a previously ordered row may become disordered. Such rows are not of course visible on the electron micrographs. This type of disordering can also occur when the energetic particle is unable to produce cascades.

In all these damage processes point defects are produced and at temperatures where they are mobile, enhanced diffusion occurs. Since ordering is presumed to occur by such point defect motion, the kinetics of the ordering process will also be enhanced. Radiation disordering theory must be able to predict both ordering and disordering rates under irradiation.

Before ordering changes can be described, it is necessary to choose some way to measure the order itself. Again we choose the long range order parameter of Bragg and Williams[42,43],

$$S = \frac{f_{A\alpha} - X_A}{1 - X_A} \qquad \text{(IV-1)}$$

where $f_{A\alpha}$ is the probability that an A atom will be on a site in the α sublattice and X_A is the fraction of A atoms. This parameter takes no account of how the disordered atoms are arranged and in particular ignores short range order. However, unlike thermal ordering where short range order is critical, most irradiation disordering is random. This is because the energetic knock-on atoms have energies larger than the ordering energy and are thus likely to be little influenced by it. Hence, this ensures that the model will not be applicable to an initially disordered alloy which is likely to develop order by domain nucleation.

1. Radiation Disordering

If the replaced atoms are exchanged randomly, then the disordering rate due to irradiation is obviously dependent upon the instantaneous order

$$\left(\frac{dS}{dt}\right)_{irr} = -\varepsilon K S \qquad \text{(IV-2)}$$

where ε is the number of replacements per displacement and K is the number of displacements per second. Equation IV-2 only requires that at long times S should tend to zero.

The fact that in a single set of replacements, atoms are not replaced randomly (as in a replacement sequence), does not matter

as long as successive sets are randomly spaced, so that no correlation occurs between neighboring sets. Departure from randomness in a single set only changes the magnitude of ε, not the form of the equation. Because Equation IV-2 is so general, it has been derived for and found to fit many different irradiation disorder situations.

Theoretical values for the replacement ratio ε have varied greatly from 1 to 1000, and this is a topic of great interest currently from the point of view of cascade studies. The calculation is very difficult requiring first a determination of the number and size distribution of cascades and then estimates of the replacements and displacements for each size of cascade. For fast neutrons, values of around 100 seem reasonable while for thermal neutrons values somewhat below this are expected ($\varepsilon \sim 10$). One MeV electrons generally give $\varepsilon \sim 1$.

2. Enhanced Thermal Ordering

Although the thermodynamics of ordering have been thoroughly studied, the kinetics of ordering have been the subject of very few papers. In a classic paper, Dienes[11] used chemical rate theory for a "reaction" in which a pair of wrong or antistructure atoms transform to a right or ordered pair. The result differs from the usual chemical rate result in that increase in the degree or order (extent of reaction) increases the ordering rate. This is, of course, the essence of the ordering reaction as a cooperative process.

In order to use Dienes' theory to describe the radiation

enhanced thermal ordering rate ($dS/dt_{thermal*}$), it is necessary to introduce the point defect concentrations. We first assume:

i) Interstitial motion in Cu_3Au does not change the degree of order. The large size difference between the atoms makes this reasonable and it is justified experimentally by the absence of ordering in stage I annealing.

ii) Ordering proceeds by a vacancy mechanism. The increased ordering rates under irradiation are good evidence for this.

The rate constants can be written as:

$$k_o = (\nu_v/2)\, C_v\, (Z_\alpha + Z_\beta - 2)\, \exp[(-E_m^o/k_BT)]\, (Z_\beta/X_A) \qquad \text{(IV-3)}$$

$$k_d = (\nu_v/2)\, C_v\, (Z_\alpha + Z_\beta - 2)\, \exp[-(E_m^o+V_oS)/k_BT](Z_\beta/X_A)$$

k_o and k_d are the rate constants for ordering and disordering jumps respectively. ν_v is the vacancy attempt frequency and V_oS is the ordering energy at order S. V_o is a constant.

The point defect concentration is introduced into the rate constants by assuming that the pair exchange occurs by successive vacancy jumps. The energy barrier to pair exchange then becomes the energy barrier to vacancy motion (E_m^o) in the double vacancy jump. The frequency is the vacancy attempt frequency divided by two for a double jump. The probability of a vacancy being in position to make the exchange is $(Z_\alpha + Z_\beta - 2)C_v$. The term in brackets is the number of sites around the pair, Z_α being the number of α sites around a β site and Z_β the number of β sites around an α site. C_v is the

vacancy concentration.

With these changes, we can now write the ordering rate as:

$$\left(\frac{dS}{dt}\right)_{thermal}^{*} = \left(\frac{\nu v}{2}\right)\left(Z_\alpha + Z_\beta - 2\right)C_v \exp\left(-E_m^o/k_BT\right)\left(\frac{Z_\beta}{X_A}\right) \quad \text{(IV-4)}$$
$$\left\{X_AX_B\left(1-S\right)^2 - \exp\left(-V_oS/k_BT\right)\left[S + X_AX_B\left(1-S\right)^2\right]\right\}$$

As we have noted, irradiation increases the vacancy concentration C_v and so enhances dS/dt. To include this effect, we use the rate theory of Brailsford and Bullough[128] to obtain C_v. The use of this theory implies that the point defects have reached their steady state concentrations under irradiation. Initially, a constant dislocation density (ρ_d) was used which is quite reasonable for long irradiation times when the sink density has reached a steady state value. However, at earlier times of irradiation, defect sinks formed by cascade collapse and loop nucleation are still evolving which implies that ρ_d increases with dose. The sink density rise can generally be expressed as

$$\rho_d(t) = \rho_d^o + \int_o^t \left(\dot{\rho}_d\right)_{t'}\, dt'$$
$$\left(\dot{\rho}_d\right)_{t'} = \left(d\rho_d/dt\right)_{t=t'} \quad \text{(IV-5)}$$

ρ_d^o is the initial sink density and $\left(\dot{\rho}_d\right)_{t'}$ is the growth rate at time t'. To first order, we assume that ρ_d rises linearly with time.

$$\rho_d(t) = \rho_d^o + \dot{\rho}_d t \quad \text{(IV-6)}$$

ρ_d of course depends on irradiation conditions. The vacancy concentration when the sink density is varying is:

$$C_v(t) = \frac{C_{ve}}{2} - \frac{Z_i D_i \rho_d(t)}{2\alpha} + \left\{\left(\frac{C_{ve}}{2} + \frac{Z_i D_i \rho_d(t)}{2\alpha}\right)^2 + \frac{K_v D_i Z_i}{Z_v D_v \alpha}\right\}^{1/2} \qquad \text{(IV-7)}$$

D_v is the vacancy diffusion coefficient and is governed by $D_v = D_{ov}\exp(-E_m/kT)$. ($E_m$, the vacancy migration energy is not necessarily the same as the ordering jump barrier E_m^o). D_i is the interstitial diffusion coefficient, Z_i and Z_v are the bias factors for the two defects, α is the recombination constant, C_{ve} is the thermal equilibrium vacancy concentration. $C_v(t)$ can now be inserted into Equation IV-4 to obtain the enhanced thermal reordering rate.

3. The Order Rate Equation

The actual ordering rate is a balance between radiation disordering rate of Equation IV-2 and the radiation enhanced ordering rate of Equation IV-4 giving

$$\frac{dS}{dt} = \frac{dS}{dt}_{irr} + \frac{dS}{dt}_{thermal^*} \qquad \text{(IV-8)}$$

where the terms on the R.H.S. are obtained from equation (IV-2) and (IV-4) .

Results from equation IV-8 using the parameters of Table IV-1 are shown in Figure IV-1. The choice of these particular values will be discussed in the next section. Here certain general features of the results are considered.

Figure IV-1 shows the variation of dS/dt together with that for its components dS/dt_{irr} and $dS/dt_{thermal*}$. The latter is identical in form to $dS/dt_{thermal*}$ obtained by Dienes except for a multiplying factor which contains the enhanced vacancy concentration. This varies with temperature as shown in Figure IV-2. At higher temperatures near the order transition temperature the multiplying factor approaches unity as there are so many thermal vacancies that the irradiation increase in their concentration is negligible. Radiation then makes little difference and the thermal ordering rate dominates. At lower temperatures the enhanced ordering rate is the dominant rate as Figure IV-1 shows. In this region enhanced ordering under irradiation will be observed. If the temperature is lowered still further, although the enhancement in vacancy concentration increases, vacancy mobility decreases and eventually disappears. Under these conditions the ordering rate is small and the disordering dominates. The most interesting temperature region is where radiation ordering and disordering rates have the same magnitude.

It is obvious from the dS/dt curves that no useful information can be obtained from change-of-slope measurements of ordering rates at fixed S values. Figure IV-3 shows dS/dt for fixed S values plotted

Table IV-1

Parameters Used in Fitting Cu_3Au Data

Vacancy motion energy	E_m	=	0.8 eV
Vacancy ordering motion energy	E_m^o	=	0.84 eV
Vacancy pre-exponential diffusion coefficient	D_{ov}	=	7.8×10^{-5} m^2/s
Vacancy formation energy	D_{fv}	=	1.28 eV
Vibrational frequency	ν_v	=	$\nu_i = 10^{13}$ Hz
Interstitial motion energy	E_{im}	=	0.12 eV
Interstitial pre-exponential diffusion coefficient	D_{oi}	=	7.8×10^{-7} m^2/s
For fast neutrons			
Vacancy loss fraction	f_v	=	0.95
Replacement to displacement ratio	ε	=	80
For thermal neutrons			
Vacancy loss faraction	f_v	=	0.0
Replacement to displacement ratio	ε	=	20
Dislocation bias for interstitials	Z_i	=	1.02
for vacancies	Z_v	=	1.0
Recombination coefficient	α	=	$10^{21}/m^2 \times D_i$
Copper concentration	X_A	=	3/4
Ordering energy	V_o	=	0.35 eV

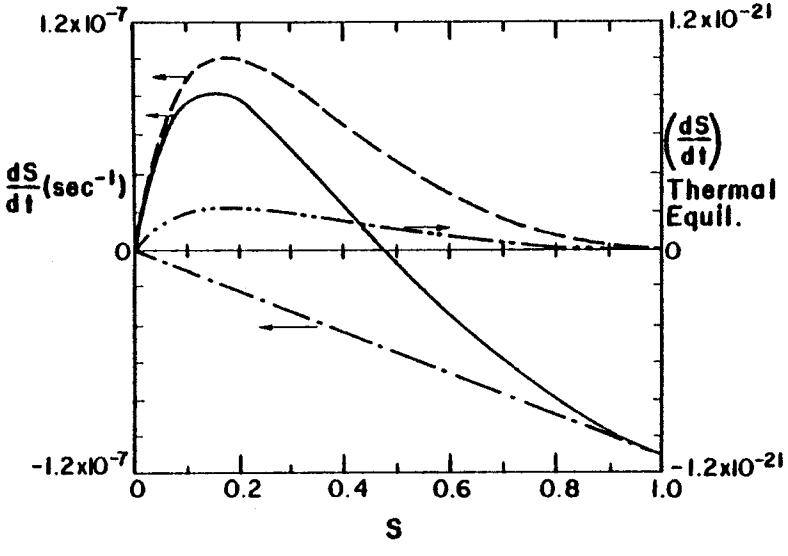

Figure IV-1. The rate of change of order as a function of order S under fast neutron irradiation condition at 27°C. The irradiation rate was 1.4×10^{-9} dpa/sec and ρ_d was $1.7 \times 10^{13}/m^2$.

-.-.- Disordering rate
----- Enhanced ordering rate
Sum of the above
-···- Thermal ordering rate in the absence of irradiation, for comparison. (different scale)

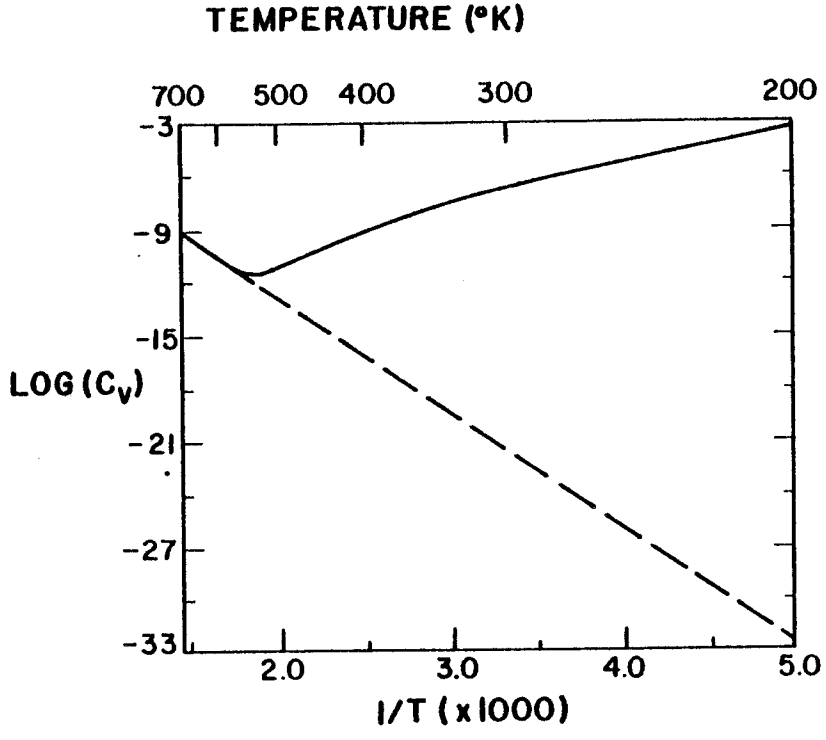

Figure IV-2. Enhanced vacancy concentration caused by fast neutron irradiation. The equilibrium concentration is shown in the dashed line. The parameters used are those in Table IV-1 with $\rho_d = 1.7 \times 10^{13}/m^2$ and $K = 1.4 \times 10^{-9}$ dpa/sec.

against the reciprocal of temperature. Since dS/dt can be either positive or negative no Arrhenius plot can be meaningful. In fact, the slope of such a plot can vary anywhere from $-\infty$ to $+\infty$. Over limited temperature ranges certain values of activation have been extracted[129] but the results, as this analysis shows, are meaningless.

Figure IV-1 also indicates that the ordering and disordering rates balance each other to give dS/dt=0 over a wide range of S values, depending on temperature. These values of S define a steady-state condition under irradiation where no further change in order takes place. These steady-state values (S_∞) were determined by setting Equation IV-8 equal to zero and solving numerically. The results are shown as a function of temperature for fast and thermal neutrons in Figure IV-4a.

The various temperature range effects are clearly visible. At high temperature the thermal equilibrium curve is approached. As the temperature decreases the order remains high due to the enhanced ordering from excess vacancies. As these become immobile at still lower temperatures radiation disordering dominates to give low S_∞ values. It is clear that there is a narrow temperature range over which S_∞ changes very rapidly. This range is itself strongly dependent on the rate and type of irradiation (i.e., upon εK). Figure IV-4a shows a plateau in the S_∞ values in the mid-range for the fast neutron case. This arises from the vacancy behavior. At very low temperatures the enhanced vacancy concentration is very large because the immobile vacancies cannot diffuse to sinks and can

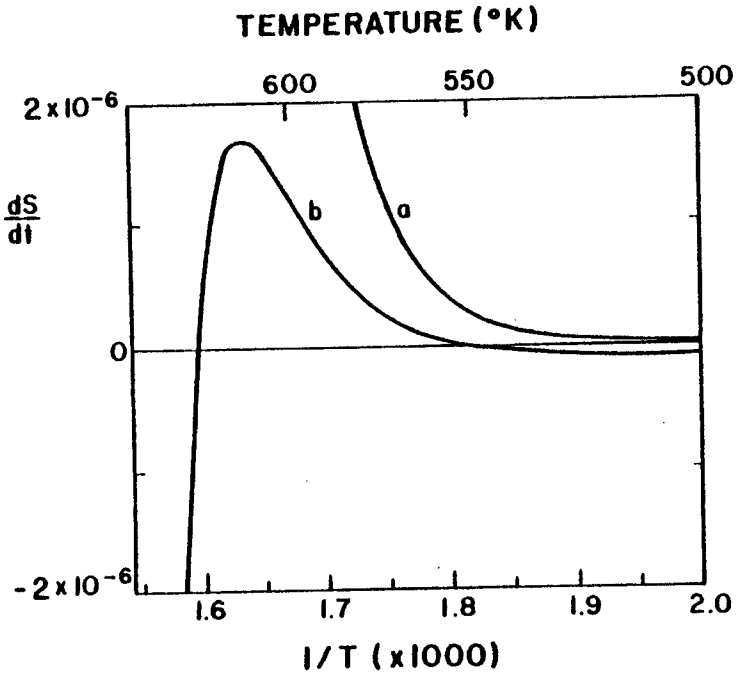

Figure IV-3. The order/disordering rate under fast neutron irradiation as a function of reciprocal temperature for (a) S=0.8 and (b) S=0.87. The parameters used were $\rho_d = 1.7 \times 10^{13}/m^2$ and $K = 1.4 \times 10^{-9}$dpa/sec.

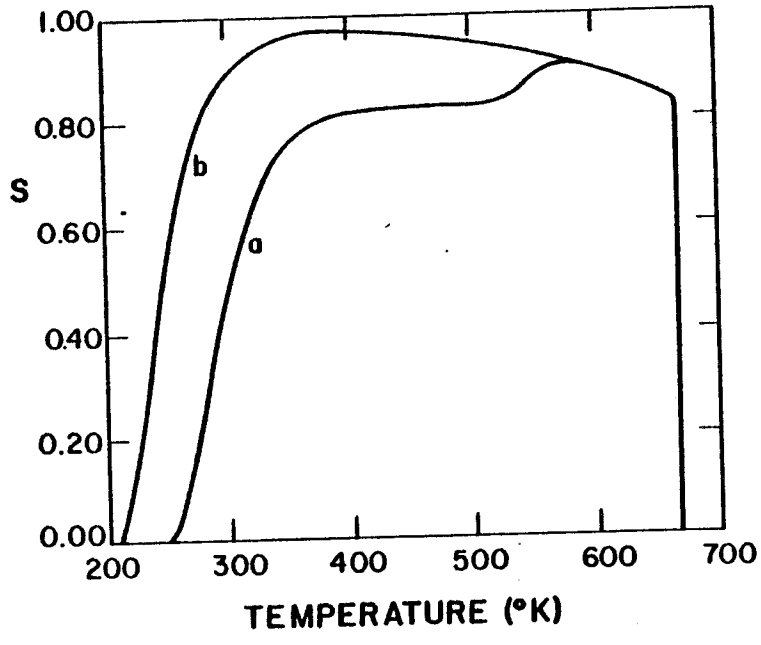

Figure IV-4a. The steady state degree of order, S, as a function of temperature for (a) fast and (b) thermal neutrons.
(a) $\rho_d = 1.7 \times 10^{13}/m^2$, $K = 1.4 \times 10^{-9}$dpa/sec
(b) $\rho_d = 10^{12}/m^2$, $K = 2.5 \times 10^{-10}$dpa/sec.

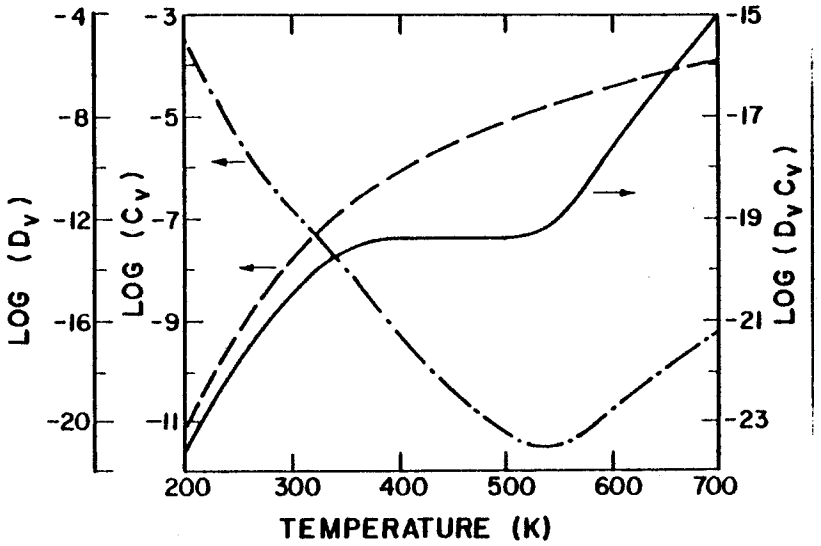

Figure IV-4b. Matrix diffusion parameter ($D_V C_V$) for fast neutrons as a function of temperature (solid line). Note the plateau which gives rise to the plateau in figure IV-4a line (a). This arises from the balance between a falling vacancy concentration (dot and dashes) and a rising vacancy diffusion coefficient (dashed line).

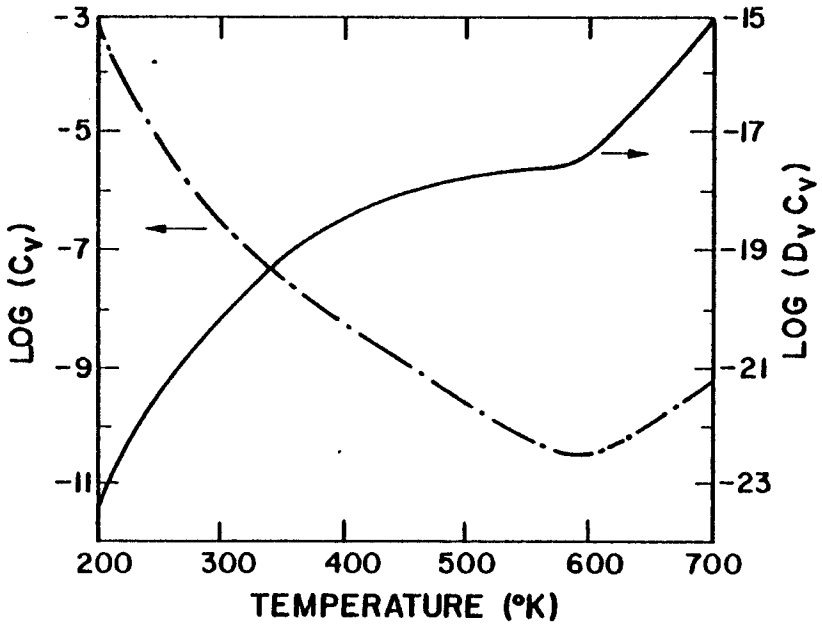

Figure IV-4c. As for 4b but for thermal neutrons. Note the absence of a well-defined plateau (even with a logarithmic scale).

only be removed by recombination with the interstitials (Figure IV-2). However, in spite of this high concentration,the diffusion of matrix atoms remains low because of low vacancy mobility (Figure IV-4b). In the intermediate range the matrix diffusion (D_vC_v) remains constant with temperature increase because the falling vacancy concentration is balanced by the increasing mobility (Figure IV-4b). The enhanced ordering rate follows the matrix diffusion closely in this range giving a similar shape of the S_∞ curve of Figure IV-4a to the diffusion curve in Figure IV-4b. At some low value of S_∞ the whole idea of long range order will break down. At this value the alloy will nucleate new ordered domains on reordering, rather than growing back into the original large domains by a gradual increase in S. This critical value of S is not known. (Experiments are not possible by thermal treatment since values of S in Cu_3Au between S=0.8 at T_c and S=0 are unobtainable by this means).

The rate equation IV-8 can only be solved by numerical methods for long range order as a function of time using $S=S_0$ at t=0 as a boundary condition where S_0 is the initial order. Many numerical integration routines are available. In this work, the Episode package[130] was used. A typical set of results in the middle temperature range is shown in Figure IV-5. These curves can be compared directly with experimental results of order parameter under irradiation.

No experimental values of order parameter determined directly from diffraction experiments on irradiated samples are available in

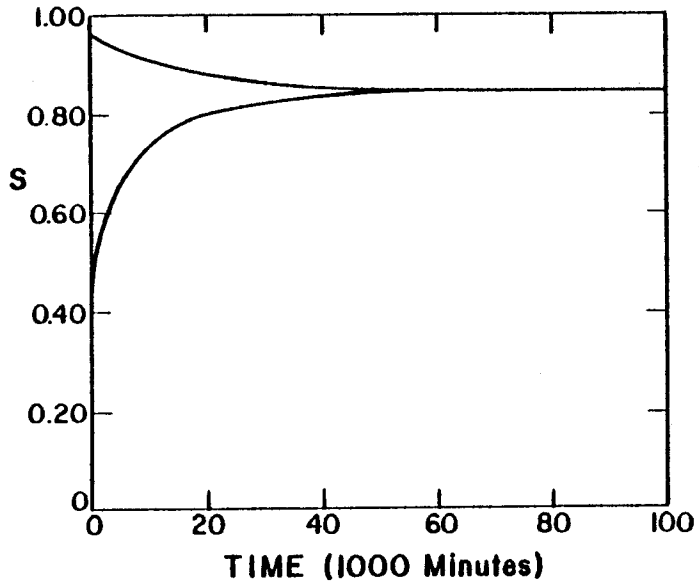

Figure IV-5. A typical set of time-dependent results with the parameters of table IV-1 and $K=1.4\times10^{-9}$dpa/sec, $\epsilon=80$ and $\rho_d=1.7\times10^{9}/cm^2$.

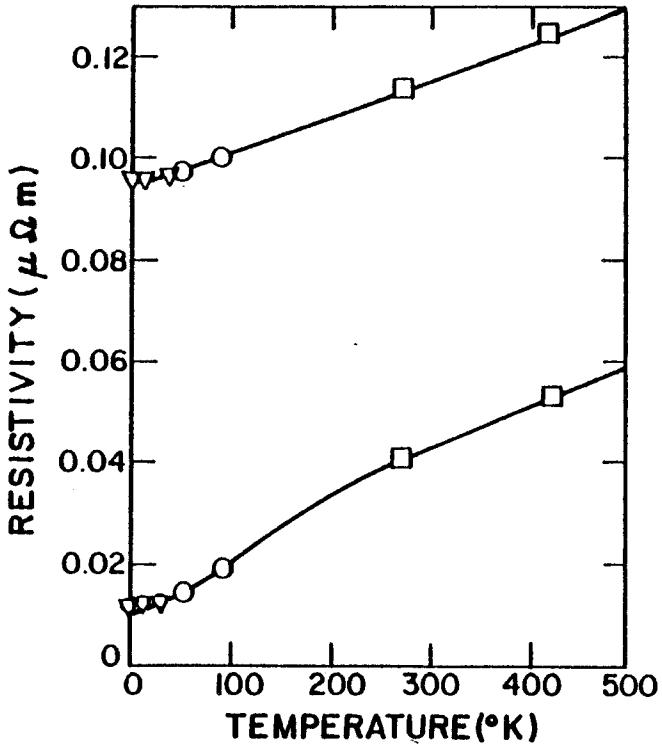

Figure IV-6. The resistivity as a function of temperature for the disordered state (upper curve) and the ordered state (lower curve).
o from ref. 56
□ from ref. 3
▽ from ref. 133.

the literature. However, several experiments using electrical resistivity as a measure of order have been reported.

C. Resistivity and the Order Parameter

There are two theories for the variation of S with electrical resistivity ρ. The first due to Muto[131] (model A) gives

$$\rho_S = \Delta\rho\ (1-S^2) + \rho_{S=1} \qquad \text{(IV-9)}$$

(where $\Delta\rho = \rho_{S=0} - \rho_{S=1}$)

The second theory due to Landauer[132] (model B) applies to a mixture of two phases and was applied to irradiated and ordered Cu_3Au by Cook and Cushing[98]; it is expressed in conductivity terms:

$$\sigma_s = \frac{1}{4}\{(3X_2-1)\sigma_2 + (3X_1-1)\sigma_1 + \qquad \text{(IV-10)}$$

$$[((3X_2-1)\sigma_2 + (3X_1-1)\sigma_1)^2 + \varepsilon\sigma_1\sigma_2]^{1/2}\}$$

where X_1 is the fraction of material with conductivity σ_1 and X_2 similarly with σ_2.

This approach is of doubtful validity in an ordering alloy where disorder involves individual atoms being misplaced. A treatment like that of Muto which treats scattering from individual anti-structure atoms seems more reasonable. In addition to these two theories, Cook and Cushing (model C) used a modification of Landauer's model, for which they did not claim high accuracy:

$$\sigma_S = \chi_1\sigma_1 + \chi_2\sigma_2 \qquad \text{(IV-11)}$$

All three models apply at constant temperature. Since $\rho_{s=1}$ and $\rho_{s=0}$ will have different temperature scattering the temperature coefficients are expected to be different. In addition, well ordered Cu_3Au has an anomalous resistivity minimum[3] below about 100°K. Since the various resistivity measurements have been made at a variety of different temperatures, it is first necessary to determine $\rho_{s=1}$ and $\rho_{s=0}$ as functions of temperature. From the data of Passaglia and Love[3] at low temperatures and of Blewitt[133,56] at 0°C and 150°C it is possible to do this (Figure IV-6). The resistivity anomaly[3] is clearly shown in the ordered alloy. In the disordered alloy it is much less. Taking these limits for each temperature for which data exists and using the information on the heat treatments it was possible to eliminate models B and C. Blewitt's "partially ordered" sample was quenched from 375°C after a long equilibration. From the experimental equilibrium order curve this should give a value of $S \sim 0.85$. It cannot be less than 0.75 which is the minimum value below T_c. Using the resistivity given by Blewitt of 3.7 μΩ m at 4°K and 7.7 μΩ m at 150°C we estimate a value of S=0.83 in good agreement with the equilibrium measurement. Theories B and C gave S=0.39 and S=0.23 respectively. Similar results were obtained for these two theories using other resistivity data, in all cases the S values were far too low. On the other hand, Muto's model (A) gave sensible values for S in the range 0.8-1.0 after long time aging below T_c.

In all subsequent analysis, therefore, Equation IV-9 was used together with Figure IV-6 to determine S from the resistivity reported.

D. Fitting the Experimental Data

As is well known the Bragg-Williams model predicts low values of S when compared with experiment. Since our approach is phenomenological, we have chosen to use a value of V_o=0.35eV which gives a good fit to the equilibrium order parameter S_e as shown in Figure IV-7. In this way we obtain a correct value for the thermal ordering rate in the absence of irradiation. However, the T_c obtained from this value of V_o by Bragg-Williams equilibrium theory will be larger than the experimental value. We simply cut off the curve at this latter temperature T_c=663^{o}K.

The clearest and most complete data is that of Kirk and Blewitt[56,133]. This includes resistivity versus irradiation time for two S_o values in a predominantly fast neutron flux at 150^{o}C and 4^{o}K, and one S_o value for a primarily thermal neutron flux at 135^{o}C. These are shown in Figure IV-8 with the theoretical curves fitted from our theory.

The 4^{o}K data (Figure IV-8a) are fitted with the disordering rate only (Equation IV-2). The only variation in these two curves is due to differing S_o and this is fixed from the resistivity data. Both curves must have the same value of εK, so these data offer a severe test of the disordering model. Agreement is satisfactory, the small deviations probably being due to small deviations from a

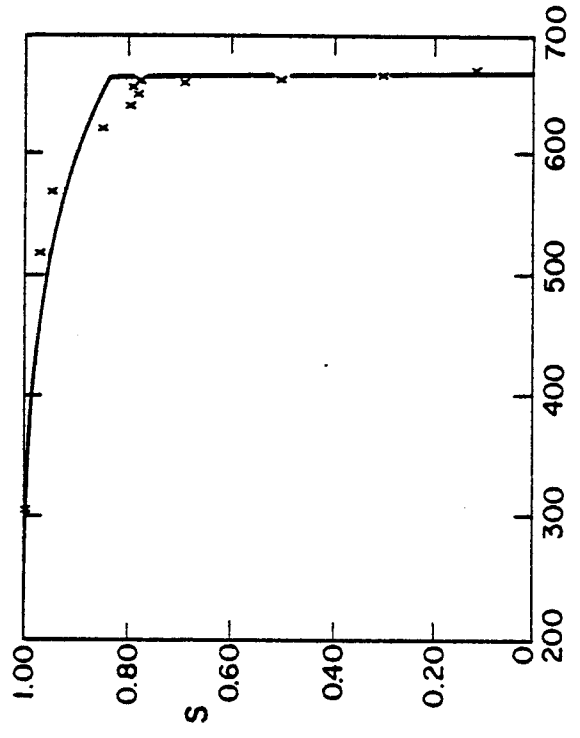

Figure IV-7. Thermal equilibrium order curve as a function of temperature with V_o=0.35eV. The experimental data are from Keating and Warren[134].

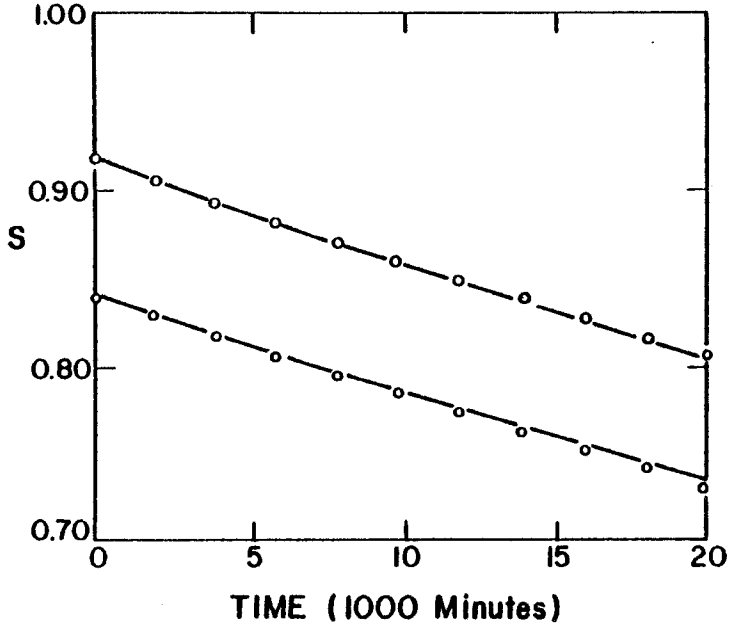

Figure IV-8. The change of order during fast neutron irradiation of Cu_3Au at 4°K from Kirk and Blewitt[56] (points). The two curves represent different starting values of the order parameter. The lines represent a data fit using the parameters in table IV-1 and K = 1.4×10^{-9}dpa/sec. and ε=80.

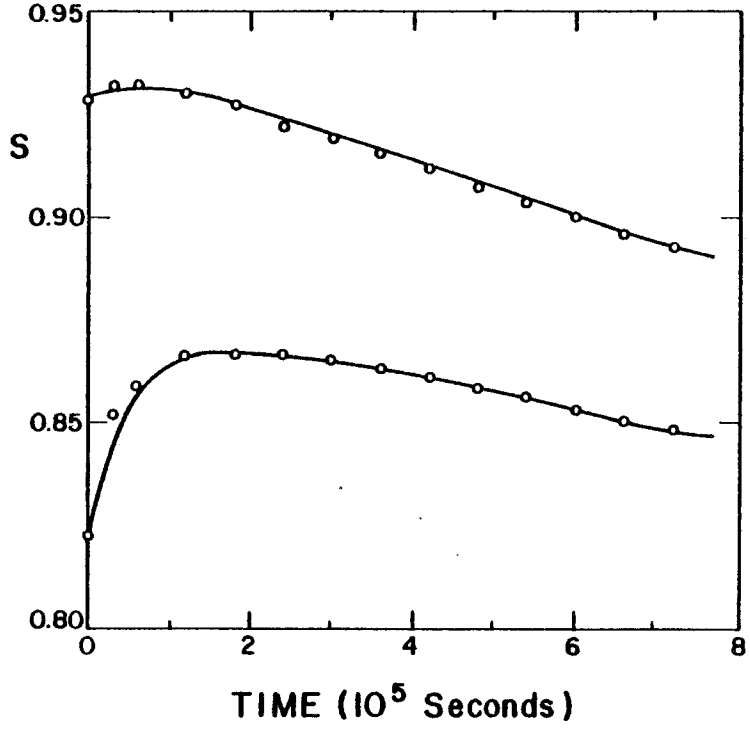

Figure IV-9. The change of order during fast neutron irradiation of Cu_3Au at 150°C from Kirk and Blewitt[56] (points). The lines show a data fit using parameters in table IV-1 with K=1.4×10^{-9}dpa/sec. Variations of sink density of the two curves are shown in figure IV-10 and 11.

quadratic resistivity dependence on S.

To separate ε and K we need an independent estimate of the displacement rate K. This has been discussed by Kirk and Blewitt[56] in their own analysis of their data.

Using primary displacement cross sections of 3 barns and 5.5 barns for copper and gold, respectively, and displacement thresholds of 25 eV and 45 eV, the fast neutron irradiation rate of 2×10^{16} neutrons/ m^2 /sec gives a displacement rate of 1.4×10^{-9} dpa/sec. For the ε K values taken from Figure IV-8 this give ε =80.

With these values of ε and K, the high temperature data can be fitted. The pre-exponentials in the diffusion coefficients D_{ov} and D_{oi} and the interstitial motion energy E_{im} were taken from copper data[135]. The vacancy motion energy was taken from Cu_3Au literature[82,96,100] to lie in the range 0.8-1.2eV. The energy of motion for an ordering jump E_m^o was chosen to be slightly larger than E_m.

Determination of C_v also requires evaluation of the cascade loss fractions f_i and f_v for interstitials and vacancies, respectively. These are not well known but have been discussed by Wollenberger[136] who presents data supporting a value of f_v=0.7 for copper under fast neutrons at low temperature (55-140^{o}K). Kirk and Blewitt suggested a value of 0.95 from their experiment at 150^{o}C. We take this latter value for f_v and f_i. The results are not sensitive to small changes in these parameters.

The lower curve of Figure IV-9 shows the fitting of Kirk and Blewitt's data for the partially ordered Cu_3Au irradiated with fast

neutrons at an irradiation temperature of 150°C. The replacement to displacement ratio used is 80 which is typical for fast neutrons. The sink density is approximated to increase linearly with time at a rate of 5400/cm^2/sec after an incubation period with constant sink density of 10^7/cm^2 as shown in Figure IV-10. The sink then saturates at a density of 2.17×10^9/cm^2.

The fitting of the model to the initially highly ordered Cu_3Au is shown in the upper curve of Figure IV-9. The irradiation temperature is again at 150°C. The rate of sink density increase used was 2700/cm^2/sec after an incubation period with constant sink density of 10^7/cm^2 as shown in Figure IV-11. Again it is obvious that an excellent fit to the data is obtained at all doses. The lower sink density increase rate required for the ordered sample compared to the partially ordered one arises because the ordering energy ($V=V_oS$) is higher at higher order and this makes the structure more resistant to defect sink formation. The sink density will of course eventually saturate but at a dose well beyond that used in this work.

With a constant defect sink density ($\sim 10^8$/cm^2) the initial transient of both curves cannot be matched as shown in our earlier work[88]. In that case, the degree of order for both samples decreases from the very beginning and only the data taken from 2×10^5 seconds onward can be fitted successfully.

However, with the sink density increasing linearly with dose, there are very few defect sinks ($\sim 10^7$/cm^2) initially. The vacancy

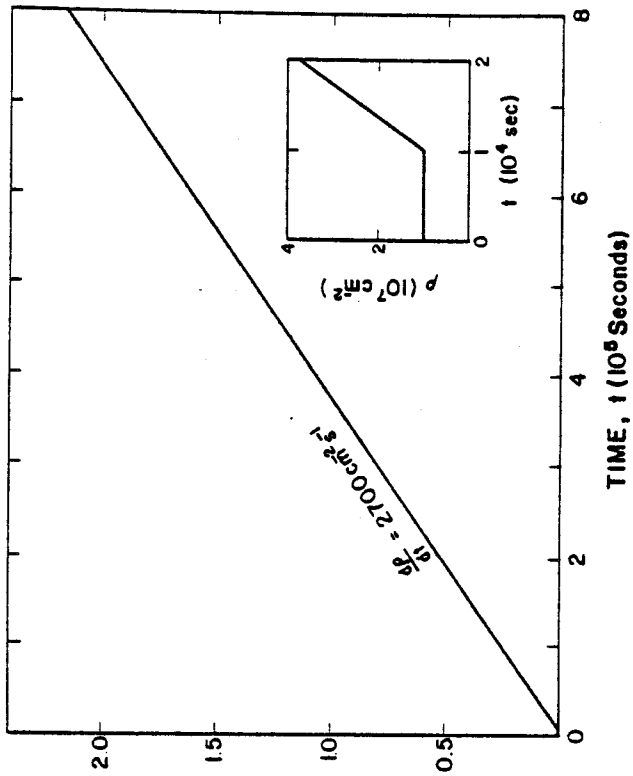

Figure IV-11. As for figure IV-10 but for the initially highly ordered case (upper curve of figure IV-9).

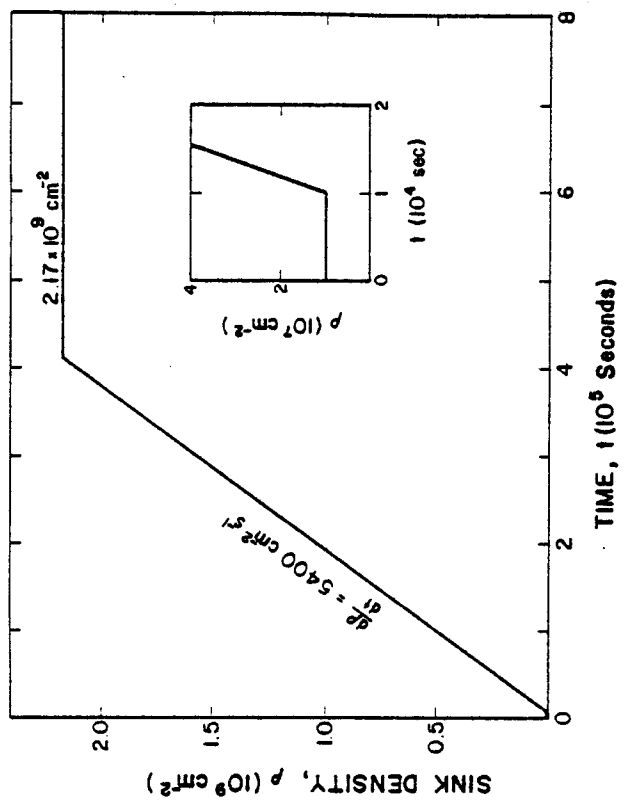

Figure IV-10. Sink density variation under fast neutron irradiated Cu_3Au for the initially partially ordered case (lower curve of figure IV-9).

concentration is then governed by recombination only and is very high. Since the reordering rate is proportional to the vacancy concentration, this results in a reordering rate higher than the disordering rate in the beginning. Therefore the order of the material increases initially. But as the sink density builds up with dose, the vacancy concentration drops according to Equation IV-7 resulting in a decrease in the reordering rate. When the rate of reordering falls below that of disordering, the curve will turn around and the degree of order will decrease as shown in Figure IV-9.

The incubation period at constant sink density was required to produce the good fit shown in each case. A sink density displaying an incubation period is characteristic of dislocation loop formation. Theoretical estimates of nucleation dose for this process are available[137-139] but at much higher dose rates and temperatures than those used in Figure IV-9. Nevertheless, the incubation doses obtained in these studies agree very well with those shown which are needed to fit the ordering data.

Transmission electron microscopy studies by Jenkins and Wilkens[105] of Cu_3Au irradiated with energetic copper ions have shown that both vacancy loops and disorder cascade patches were formed in the cascades. The formation of such defects would suggest that the sink density should rise from the very beginning without any incubation. However, this experiment was performed at room temperature while Kirk and Blewitt's neutron irradiation was done at 150°C. At these high temperatures, the cascade debris is expected to anneal out

quickly leaving nucleated interstitial loops as the dominant sinks.

The length of the transient is a measure of the time needed for the dislocations to dominate as sinks. It is clear that ρ_d is changing much more slowly than the order parameter. (This is why one can speak meaningfully of a steady-state order even when the dislocation density is varying.) In fact, the dislocation density will steadily increase and saturate after several dpa. In contrast, order steady-state is reached after $\sim$0.01 dpa. This implies that our so-called steady-state order will change somewhat with the dislocation density, tending to drift slowly lower with very long irradiation times.

This suggestion for the transient also explains why it has a larger magnitude for specimens with lower order. In such specimens the vacancies during their extended lifetime at the beginning of reaction meet more wrong atoms than in more highly ordered samples. All this is automatically accounted for in the model.

The model described was designed for the three dimensional ordering diffusion of point defects appropriate to the fast neutron case. Thermal neutrons, however, predominantly disorder by replacement collision sequences. A replacement collision sequence consists of a row of atoms all displaced one atomic jump from their original positions causing a previously ordered row to become disordered.

In Figure IV-12, the thermal neutron irradiation data are fitted with the same model used for fast neutrons (dash line). The irradiation temperature is at 135°C and the displacement rate is

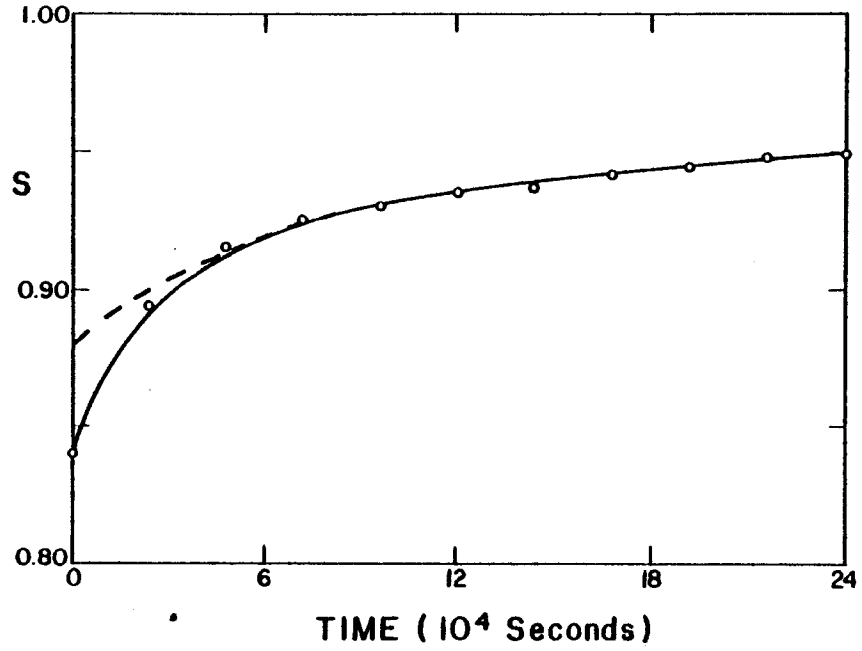

Figure IV-12. The change of order during thermal neutron irradiation of Cu_3Au at 135°C from Kirk and Blewitt[56]. using ε=20, K=2.5x10^{-10}dpa/sec and sink density increase of 500/cm^2/sec. The solid line uses an enhanced vacancy reordering multiplier of [2.3 exp(-t/60000) + 1] (see text).

2.5×10^{-10} dpa/sec. A replacement to displacement ratio of 20 is used. The dashed line shows the best fit possible using a linear rise of sink density of $500/cm^2/sec$. As expected, it is found that the entire curve cannot be fitted successfully by using any reasonable linear increase of sink density.

Since each faulted row of the replacement collision sequences can be easily ordered by one vacancy moving along it, it is probably that the ordering rate is much higher than in the case of fast neutrons where the cascades cause disordering of three dimensional regions. In the fast neutron case, only wrong atoms on the surface of the cascade are adjacent to the ordered matrix which defines the proper sublattice. Only vacancies moving along this layer have the high efficiency of reordering characteristic of the replacement collision sequences. Therefore, it is obvious that the reordering rate in the case of thermal neutron irradiation needs to be modified such that it is higher at early times and approaches the normal value when overlapping of replacement sequences begins.

To model this effect, the reordering rate was multiplied by a factor of $[2.3 \exp(-t/60000) + 1]$ where t is the irradiation time in seconds. This means that the vacancy is more than three times as effective in reordering at the start. Each vacancy then has to reorder on the average about three disordered pairs in each sequence. This implies that the average replacement sequence length is around six pairs (or 12 atoms). Since an ε value of 20 is used, this means each displacement induces one to two such sequences, which is quite

reasonable.

With this modification, the initial transient in the thermal neutron case can also be fitted successfully as the solid line of Figure IV-12 shows. The sink density increase is taken as $500/cm^2/sec$ with initial sink density of $10^7/cm^2$.

The remaining data for irradiation of Cu_3Au in the literature is much older and reactor dosimetry was less complete. Sufficient details of the nature and magnitude of the fluxes are, therefore, lacking. However, we were able to fit all these data successfully with our model using the same defect parameters established above. The only parameters changed were ρ_d and K.

Figure IV-13 shows the fitting to the fast neutron irradiation of Cu_3Au ato 40°C of Siegel[85]. The best fit was obtained using an initial sink density of $10^7/cm^2$ and a linear rise rate of $35000/cm^2/sec$. In this case, no incubation period was necessary since the irradiation was carried out at low enough temperature that cascade debris could survive and become the dominant sink. This is in agreement with the observation of Jenkins and Wilkens discussed above.

In Figure IV-14, the data of Cook and Cushing[98] during fast neutron irradiation of Cu_3Au is shown. The irradiation temperatures were 106°C (upper curve) and 35°C (lower curve). The damage rate was $3x10^{-9}$ dpa/sec. The upper curve was fitted with a sink density rise rate of $5500/cm^2/sec$ after an incubation period of 10^4 seconds of $10^7/cm^2$ of defect sink. The lower curve used a linear sink density increase of $6000/cm^2/sec$ from an initial density of $10^7/cm^2$ without

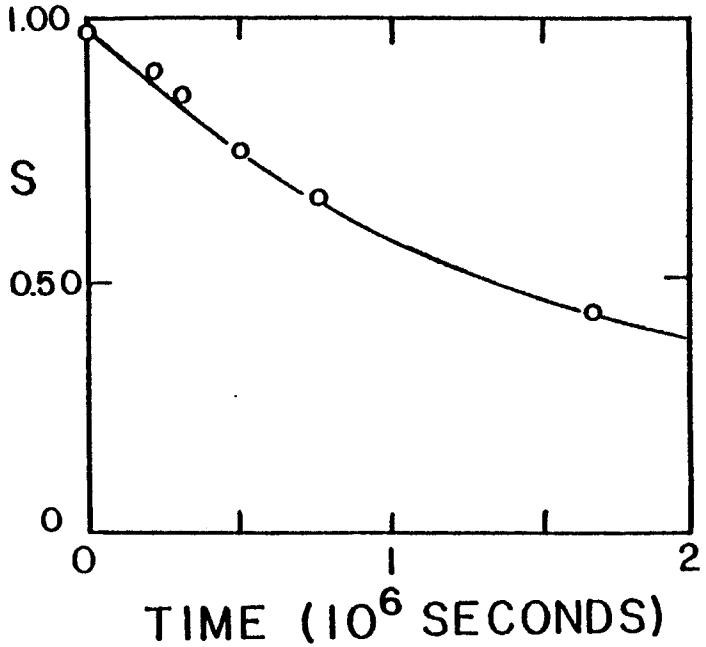

Figure IV-13. The fast neutron irradiation data of Cu_3Au by Siegel[85] at 40°C is represented by open circles. It is fitted using $K=8\times10^{-9}$dpa/sec and a linear sink density rise rate of 35000/cm^2/sec. The initial sink density used is 10^7/cm^2.

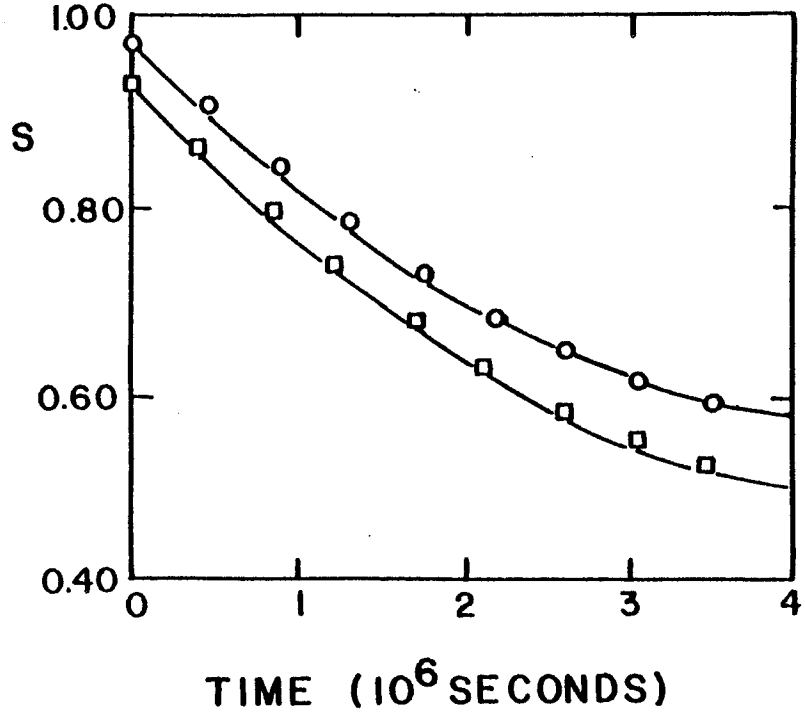

Figure IV-14. The data of Cook and Cushing[98] for fast neutron irradiated Cu_3Au at a damage rate of 3×10^{-9}dpa/sec is shown. The upper curve (106°C) is fitted with $\dot{\rho}_d=5500$/cm^2/sec with a 10^4seconds incubation period. The lower curve (35°C) is fitted with $\dot{\rho}_d=6000$/cm^2/sec with no incubation. Initial sink density for both cases is 10^7/cm^2.

any incubation. Again the model provides an excellent fit to the experimental result.

The experiments of Siegel and Cook and Cushing were performed at higher fluxes and lower temperatures than the work of Kirk and Blewitt. At lower temperature the vacancies become less mobile and recombination then becomes more important than flow to dislocation even at high sink density. This makes the initial transient negligible.

E. Discussion

The successful fitting of such a varied collection of data with similar parameters in a straight forward phenomenological model is remarkable. It should not be thought that this is because the curves can be fitted with a wide range of different parameter combinations. In fact the choice of the key parameters is very narrowly restricted.

The ordering energy V_o is fixed by the requirement of matching the thermal equilibrium order at low and intermediate temperatures. The multiple εK is fixed by the low temperature experiments. The diffusional parameters are not well known (D_{ov}, D_{oi}, E_{im}, E_v^o, E_{vf}, α). The interstitial diffusion however must be rapid at these temperatures which implies that the exact value of motion energy E_{im} is less important than the fact that it is small. D_{ov} and ν can be adjusted to compensate for a change in vacancy motion energy E_m and hence it is possible to match the same data at a given temperature with various combinations. However, it is impossible to match the data at

different temperatures in this way. In fact the strong temperature variation very closely limits the values of E_m and E_m^o to those given in Table IV-1. However, it is possible to decrease E_m and simultaneously increase E_m^o in such a way that the quality of fit only decreases slowly. From the current data therefore we can only fix their combination precisely. The current values are accurate to $\pm$0.05eV, but the combination is better than that. However, with more data at steady-state it should be possible to fix these energies very precisely since the shape of the predicted S versus temperature curve varies strongly with such changes. Since the same parameters used for the time dependent curves were used to determine the steady-state order curves of Figure IV-4, we believe that the latter give an accurate prediction. The only remaining variation is the slow change in the dislocation density as radiation proceeds. This variation has been experimentally observed and the modelling used in this work is quite reasonable.

From the point of view of our model the current data is very incomplete. An ideal experiment would be to irradiate Cu_3Au for longer times at a wide range of temperatures. Each flux should also be used at low temperatures (below room temperature) to determine εK. It is essential that all experiments begin with large domain size and a well defined order parameter. The dislocation density variation should be monitored also. With this information our model could be tested much more completely. The results so far suggest that these experiments could provide accurate data for point defect behavior in Cu_3Au and detailed information on cascades as a function of temperature.

There is an urgent need for an experimental test of Muto's model relating resistivity and the long range order parameter.

We note also that radiation is a very useful tool in the study of order/disorder reactions. The enhanced ordering rate could well be used to produce more completely ordered materials at lower temperatures where the thermal reaction is too slow to go to completion. In addition, lower values of S can be obtained by low temperature irradiations than can be obtained by thermal treatments. This will permit the study of ordered alloys over a much wider range of S than has been used hitherto.

V. EXPERIMENTAL TECHNIQUES

A. Copper-Palladium Alloy

In all the experimental work in this thesis, copper-palladium alloy of 52:48 atomic percent composition was used. The thermal equilibrium phase diagram of this system is shown in Figure V-1[140]. The copper-palladium system has a first degree order-disorder transformation at a composition between 40 and 50% palladium. The maximum transition temperature (600°C) occurs just below 50% palladium.

In its ordered state (β -CuPd), the alloy possesses a CsCl (B2) type superstructure. At the transition temperature, besides undergoing an order-disorder transformation, it also changes its basic crystal structure to a face-centered-cubic type structure (α -CuPd) (also called A1 structure). The solid-liquid transformation occurs at about 1250°C for the 50:50 composition.

The alloy was melted at the University of Wisconsin. Marz grade copper and marz grade palladium were purchased from Material Research Corporation with their impurity contents listed in Table V-1. A starting ratio of 55 atomic percent of copper was used to anticipate the excess loss of copper during melting because of its higher vapor pressure. The mixture was placed in an alumina crucible and melted three times in a sealed induction furnace (TOKATRON) back-filled with high purity argon gas. The ingot was turned over in between melts to ensure complete mixing.

TABLE V-1

Impurity Content of Marz Grade Copper and Palladium as Received from Material Research Corporation

	Copper* (wt. ppm)	Palladium (wt. ppm)
C	<10.0	------
O	2.0	------
Al	1.0	<10.0
Mg	<0.10	<10.0
S	0.50	------
Ca	0.40	------
Fe	0.80	20.0
Cu	Major	<10.0
Si	0.30	40.0
Cr	0.30	------
Zn	4.50	------
Zr	<0.10	<10.0
Ag	0.50	------
Rh	------	<10.0
Pt	0.10	<10.0
Pb	0.70	------

* Copper also contains 0.10 wt.ppm of H, N, Na, P, Cl, K, Ti, Ni, Ca, Nb, Mo, Pd, In, Sn, Sb, Ta, W, Au.

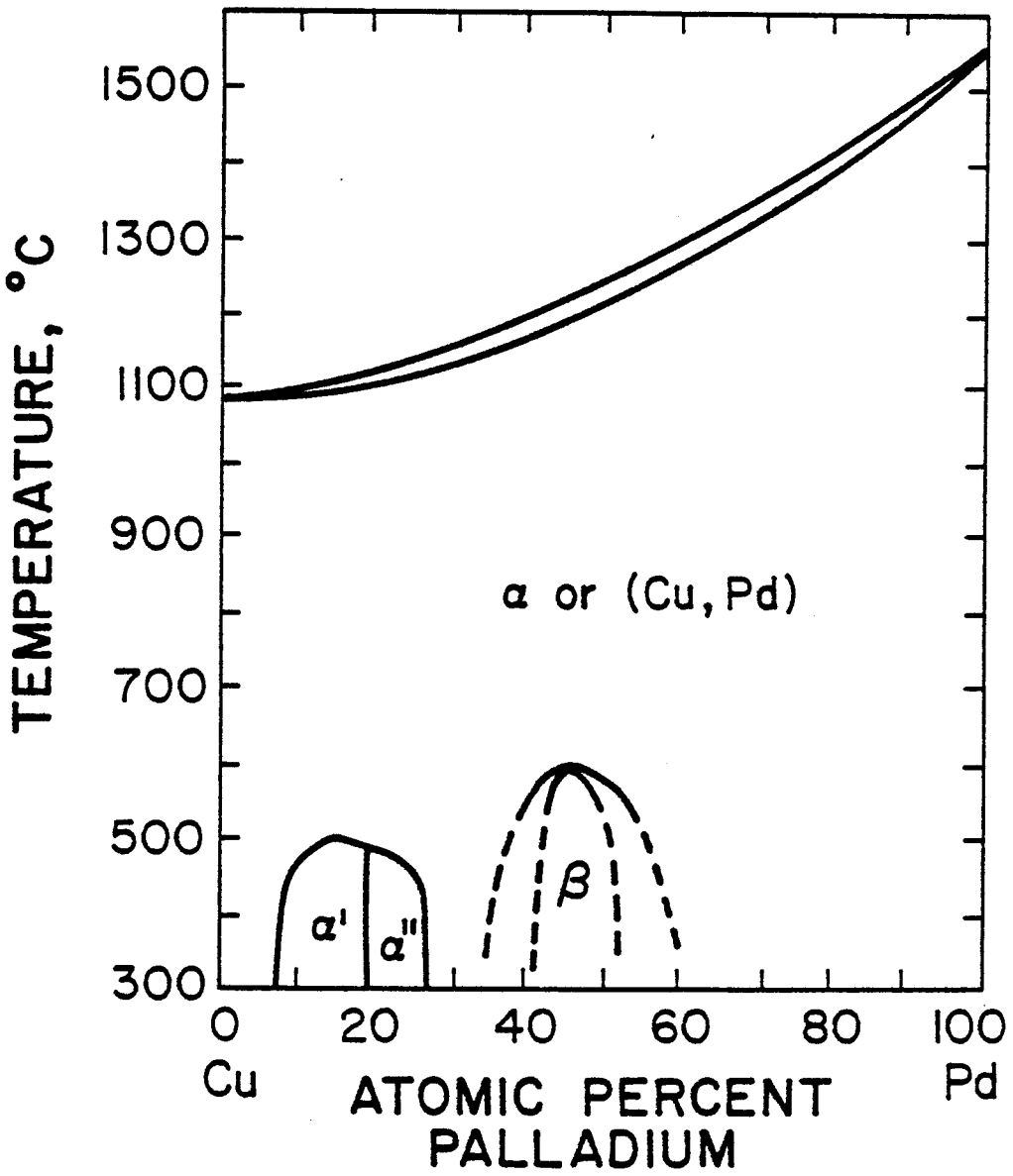

Figure V-1. Thermal equilibrium phase diagram for the Copper-Palladium system[140].

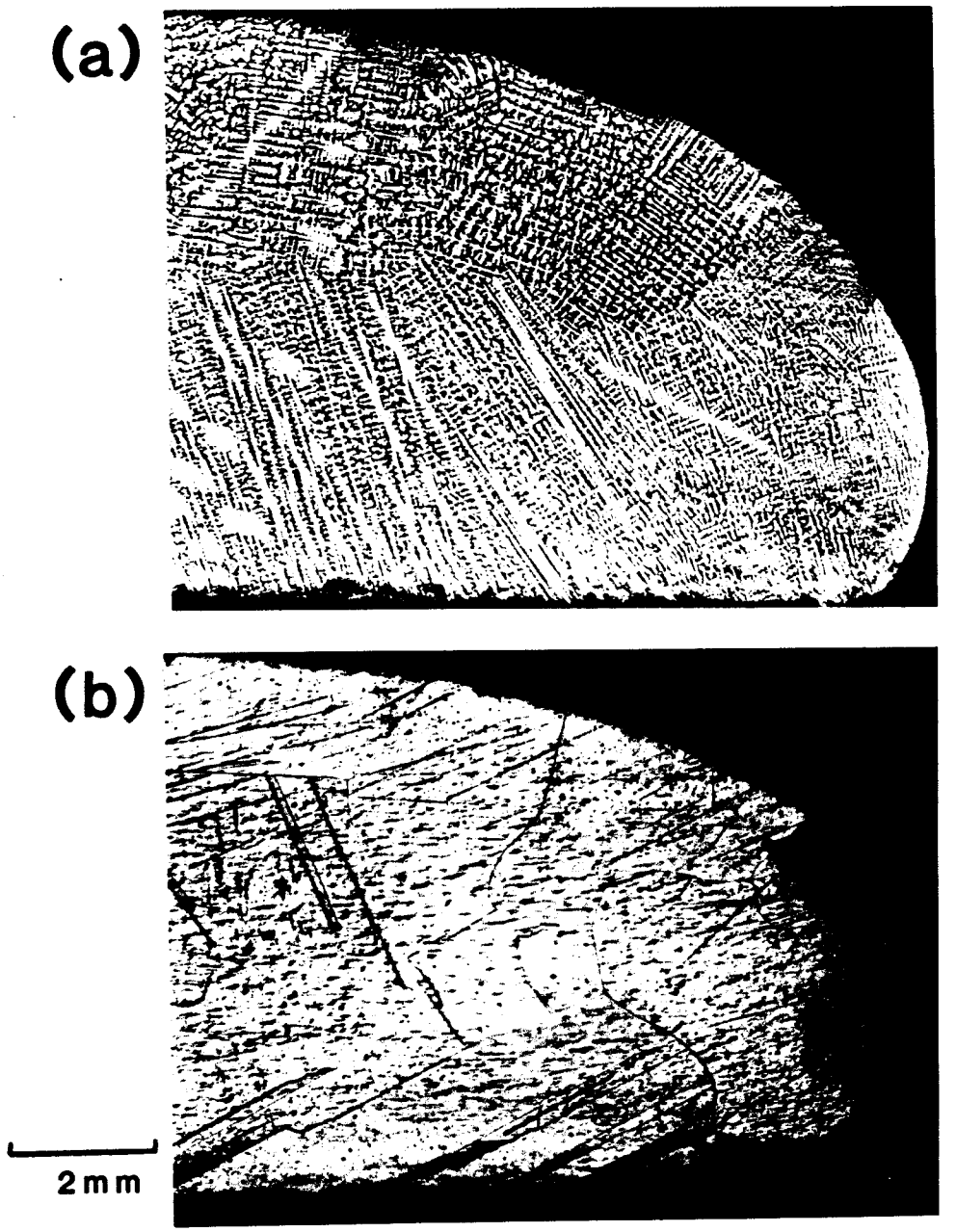

Figure V-2. Optical micrographs of the CuPd alloy showing (a) dentritic structure as casted and (b) after homogenization at 1050°C for 100 hours (notice the large grain size after this process).

The ingot as casted had a dendritric structure as shown in Figure V-2a. It was then sealed in a quartz tube back-filled with argon gas and homogenized at 1050°C for 100 hours in a horizontal furnace. The final structure consists of grains around 2mm in diameter as shown in Figure V-2b. The ingot was then step-rolled down to a final thickness of 0.4mm with quenches in between rolls. The quenching procedure involves holding the alloy in argon gas at 800°C for one hour to remove all the cold work introduced by rolling and then water-quenched. These quenches are necessary since the material in its ordered state is very brittle and is likely to break in the rolling process. Discs of a 3mm diameter were punched from the sheet for heavy ion irradiation. A slice of the sheet was sent to Lawrence Livermore Laboratory[141] where it was rolled further down to 0.04mm. Resistivity samples were made by slicing this 0.04mm sheet into 4cm long and 0.4mm wide foils.

The composition of the 0.4mm sheet was analysed by two independent techniques: neutron activation and chemical analysis. The former was done using the University of Wisconsin Reactor Laboratory while the latter by Anderson Laboratory. Both analysis give agreeing results of about 48 atomic percent palladium.

The following annealing procedure was used to obtain highly ordered specimen. Twelve 3mm diameter microscopy discs separated by quartz spacers were sealed in quartz tube back-filled with helium gas. It was annealed in a horizontal furnace to 800°C for two hours. Then the temperature was lowered to 600°C followed by a slow cooling

to 100°C over a period of eight days. Highly ordered foil specimens for resistivity measurement were also obtained using the same method.

Presence of order structure in these samples was confirmed by the observation of strong superlattice reflections in the transmission electron microscope as well as their low resistivity values.

To obtain disordered samples, the quartz tube containing the samples (either discs or foils) were quenched from 800°C into ice water instead of the slow cooling. These samples have higher resistivity values than the ordered ones. Their diffraction patterns also indicate they are disordered.

B. Heavy Ion Irradiation

Most of the experimental work was involved in studying the effect of 14 MeV copper ions on the ordered structure of CuPd. Post-irradiation analysis was done on all the samples using the JEOL 100B transmission electron microscope. Initially ordered samples were irradiated from 23°C (room temperature) to 550°C using a Tandem accelerator. Samples at 23°C, 67°C and 110°C were irradiated to different doses to study how the alloy approaches the final damage state. Two damage rates were used on the 23°C samples to examine what effect, if any, the dose rate had. Two samples, one at 200°C and the other at 250°C, were irradiated in their disordered state to see if such irradiation is capable of enhancing reordering.

1. Irradiation Facility

The University of Wisconsin Tandem Van de Graaff was used to perform all the heavy ion irradiation. This system has been described in detail elsewhere[142]. The 3mm diameter samples were bombarded with 14 MeV copper ions. Figure V-3 shows schematically the main components of the facility. A Source of Negative Ions by Cesium Sputtering (SNICS) developed by Smith and Richards and improved by Billen[143] was used to produce negative copper ions. These ions were injected into the beam tube at about 20 KV and then deflected 90° by an electrostatic mirror into the low energy end of the machine. The heavy ions were accelerated until they reached the N_2 gas stripper canel located at the terminal. The stripper was used to provide charge exchange with negative ions to produce positive ions. The beam was accelerated again through the high energy section. The total energy attained in the tandem system is given by

$$E = (q + 1)V \qquad (V\text{-}1)$$

where q is the charge state of the ion after stripping and V is the operating terminal voltage. After emerging from the accelerating beam tube, the ion beam then passed through an analyzing magnet and impinged on the sample in the target area. Due to the small charge to mass ratio of the ions, the analyzing magnet was only capable of deflecting the beam by about 1/4°. This magnet together with a set of quadrupole lenses and slits were used to select the appropriate

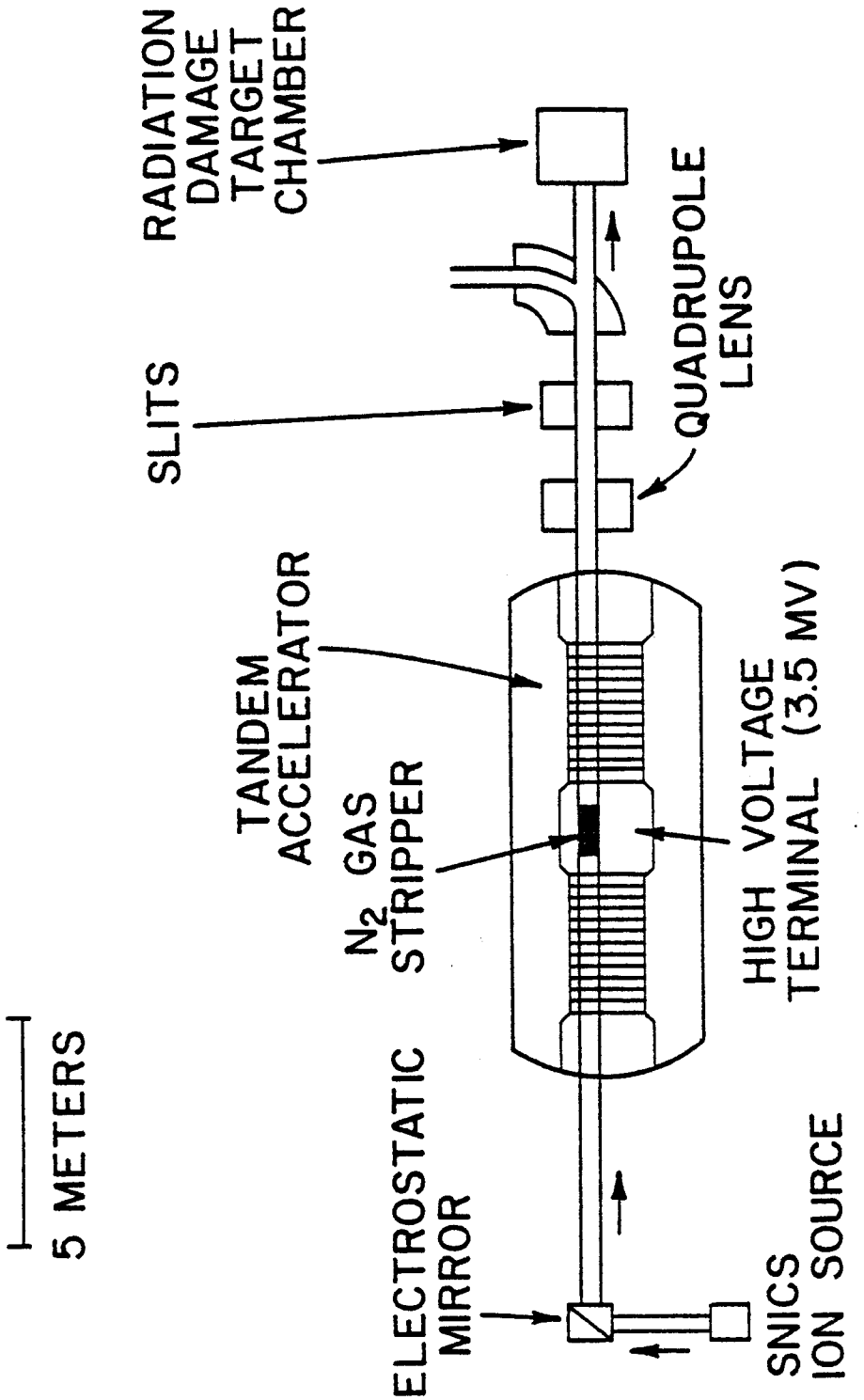

Figure V-3. Schematic of the University of Wisconsin heavy ion irradiation facility.

charge state. This charge state, q, was determined by elastic scattering of the beam through 90° by a thin gold foil and detected by a solid state detector. In this experiment, the terminal potential was maintained at 3.5 MV and a charge state of 3 was selected giving an overall beam energy of 14 MeV. Before irradiating the sample, by moving the sample out of the beam path, the beam intensity at position before and after the sample could be determined by the mask cup and the exit Faraday cup respectively. During irradiation, the mask cup was replaced by a 3mm diameter mask aperture to define beam on target.

The sample area was evacuated by a 600 liter/sec Getter Ion Pump. This high vacuum chamber was connected to the main beam tube through two intermediate pumping stages as shown in Figure V-4. The vacuum of the first pumping stage was maintained by a 200 liter/sec diffusion pump with a liquid nitrogen cold trap while the second (or intermediate) pumping stage was pumped by a 300 liter/sec orbitron pump. These three pumping stages were separated by pumping impedences to insure proper vacuum isolation. During irradiation, the sample chamber was maintained at a pressure below 10^{-8} torr.

2. Sample Holders

All the heavy ion irradiations were done at temperatures between 23°C and 550°C. To cover this wide temperature range, two

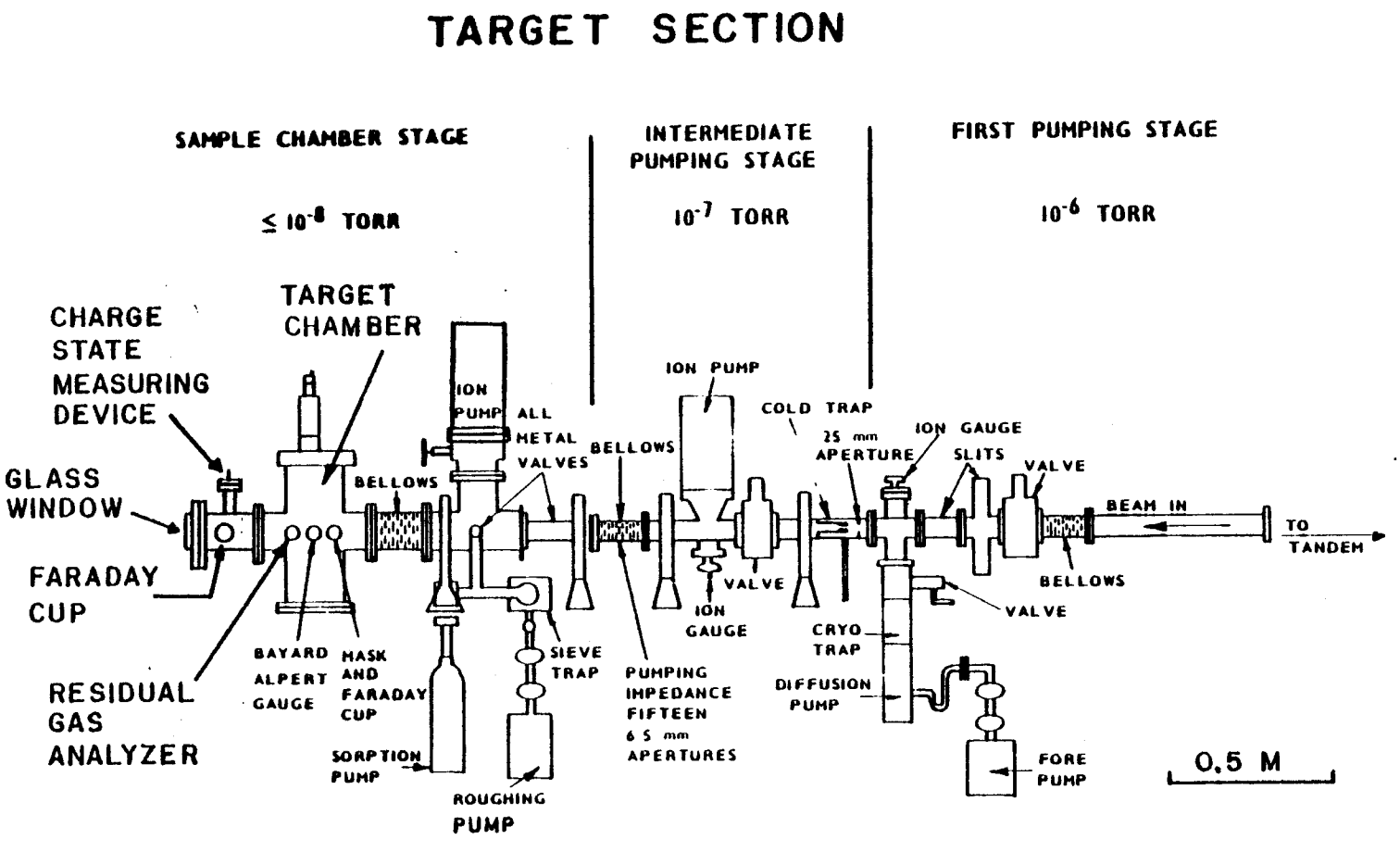

Figure V-4. Target section of the U.W. Heavy Ion Irradiation Facility.

sample holders are needed: a low temperature holder[144] that operates between 23°C and 110°C and a high temperature holder[145] between 200°C and 550°C.

Figure V-5 is a photograph showing the low temperature holder[144]. It consisted of a long 23mm diameter aluminum rod which could hold up to eight 3mm diameter specimen discs. Each specimen was individually clamped in the holder by a hollow stainless steel screw. The temperature of the sample was sensed with a chromel-alumel thermocouple through a well conductive path. This good thermal conduction was also crucial to minimize the amount of temperature rise due to beam heating. The temperature was controlled by comparing the sample temperature to a set reference value. The error signal was used to drive a thermoelectrical modulus clamped at the other end of the aluminum rod. The entire assembly was electrical isolated and connected to a current integrator so that the total beam dose on the sample could be determined. The holder was suspended from an adjustable bellows which allowed vertical movement so the individual sample could be brought into the beam path. Three clearence holes were provided so that the beam could pass through the target area. This was necessary for making charge state measurement as well as using the exit cup to check the beam intensity.

The high temperature holder[145] with its heater assembly is shown in Figure V-6. This holder could accommodate up to eight 3mm diameter discs. Each disc was mounted on individual tantalum

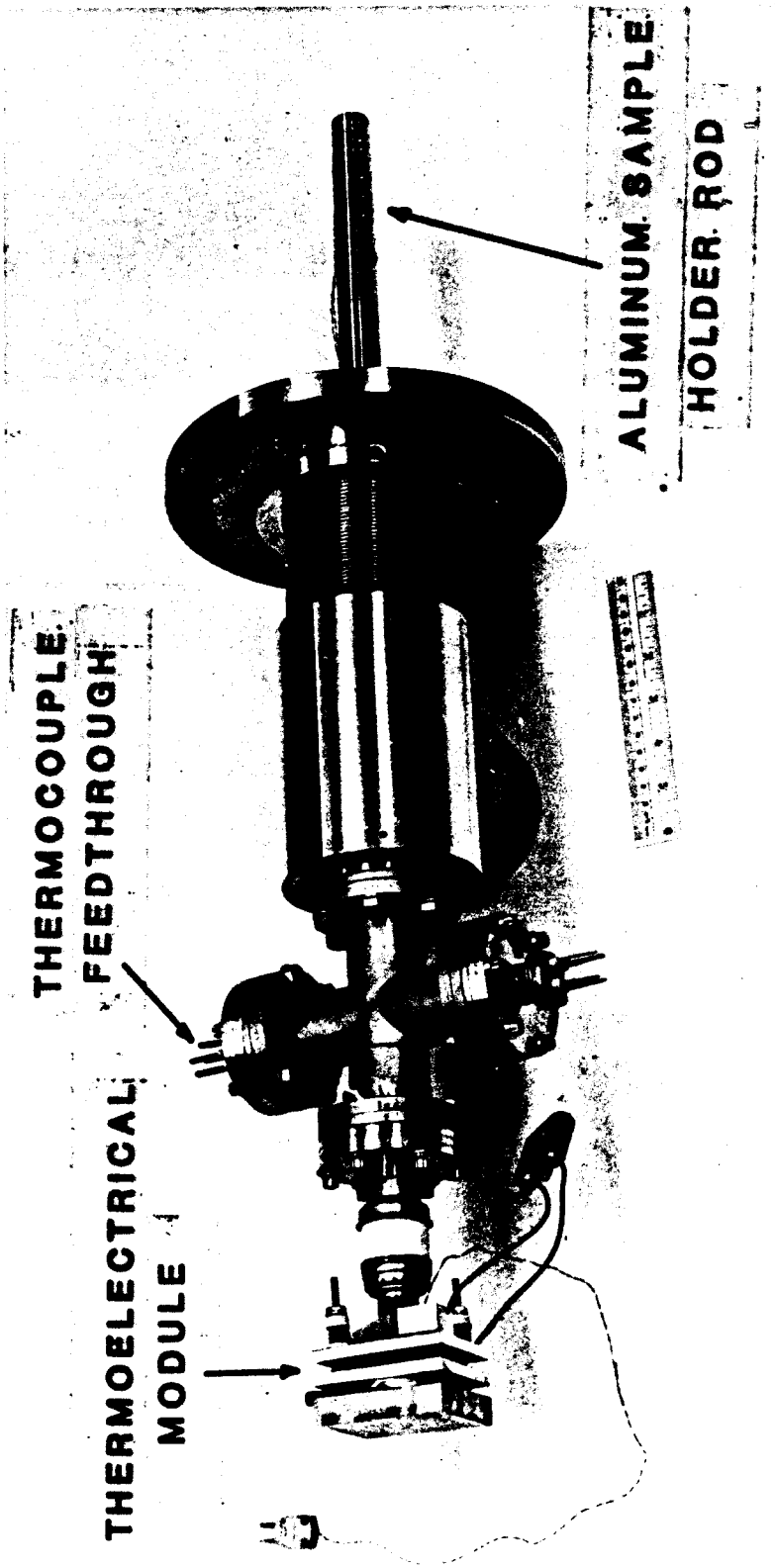

Figure V-5. Sample holder for low temperature ($23^{o}C$ to $110^{o}C$) ion irradiation.

holder. These eight individual tantalum holders were welded symmetrically (at 45° apart) onto a 10 cm diameter stainless steel disc forming a carrousel arrangement. This carrousel was attached to a bellows and high vacuum rotary feedthrough assembly enabling the assembly to rotate and translate vertically.

The temperature of each sample was sensed by a chromel-alumel thermocouple. A 0.3mm thick tantalum plate was tightly sandwiched between the holder and the sample to provide a good thermal conductive path. This helped to reduce the effect of beam heating.

The heating elements consisted of two 0.025mm tantalum sheets that subtend an angle of 40° separated with a 1cm gap as shown in Figure V-7. The heater sheets had 0.6mm diameter holes for the beam to pass through and for alignment purpose. The sample temperature was controlled manually by adjusting the amount of A.C. current to the heater via an isolated transformation.

In this arrangement, only the sample under irradiation was heated by rotating it into the heater position. The other seven samples were kept away from the hot zone and maintained at much lower temperatures. This system can prevent undesirable post-irradiation (or pre-irradiation) annealing.

The entire carrousel was electrically insulated so that the total beam current could be measured in the same manner discussed earlier for the low temperature holder.

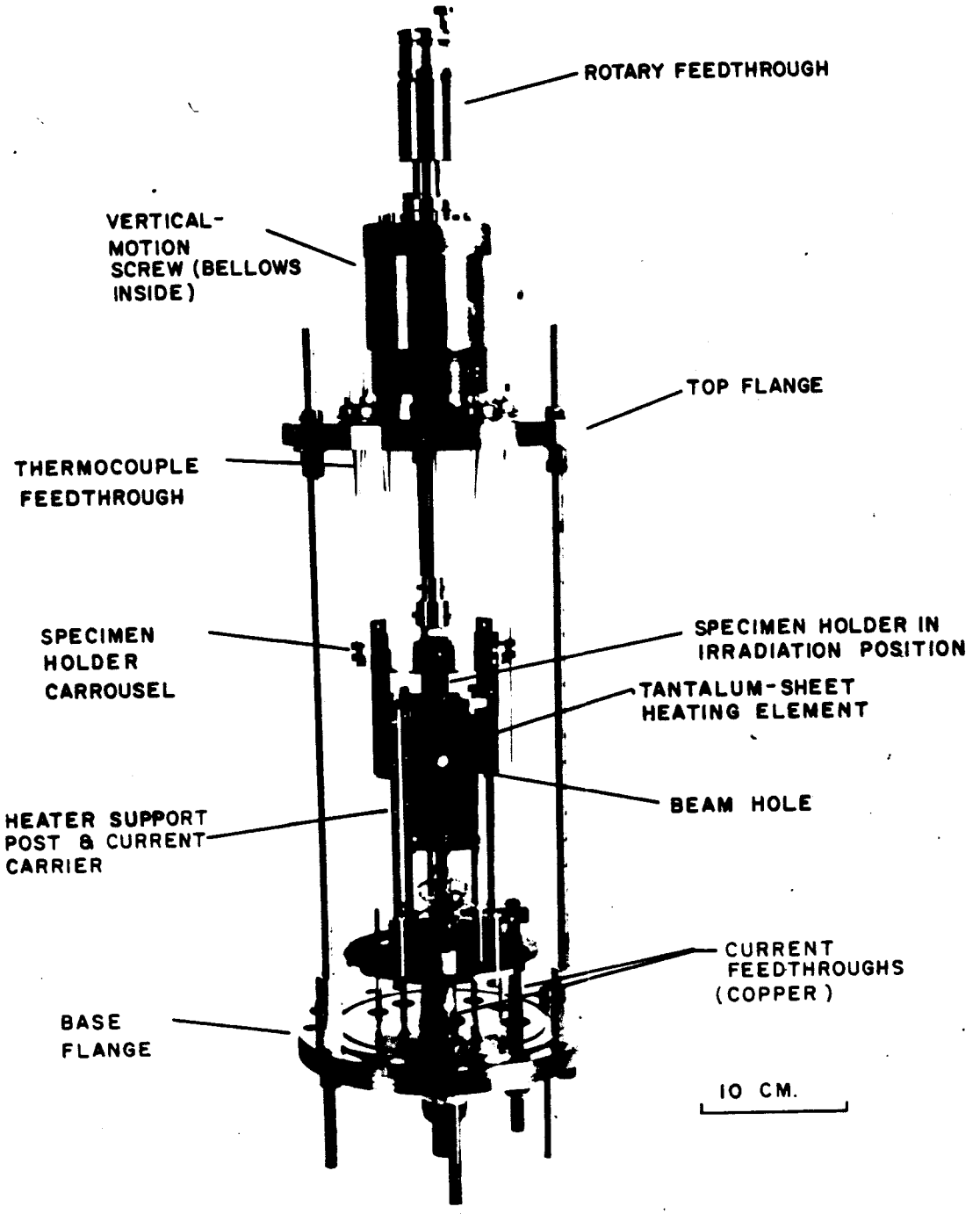

Figure V-6. Sample holder for high temperature ($200^{o}C$ to $550^{o}C$) ion irradiation.

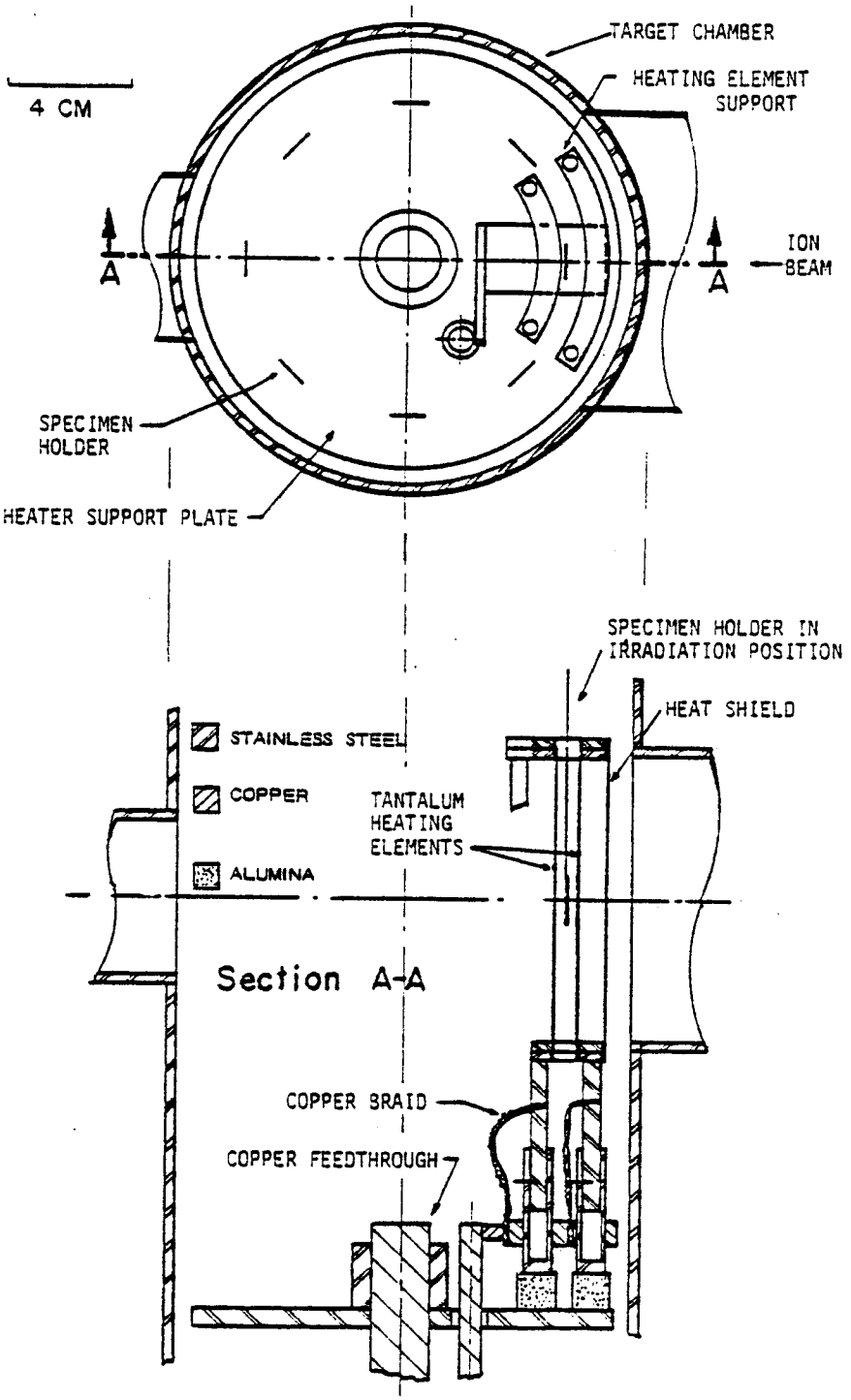

Figure V-7. Top and cross-sectional view of the target chamber with the high temperature holder in place.

3. Pre-Irradiation Sample Preparation

After the 3mm diameter discs had been properly heat treated as described in section V-A, they were then mounted securely on an epoxy polishing holder. They were then first hand polished with 600 grid emery cloth followed by polishing on a rotating table with 0.3 micron alumina powder. At this stage, the sample surface was relatively flat but full of scratches. They were then placed in the Syntron polishing machine with the same 0.3 micron alumina polishing powder for four hours. After this process, the samples were very flat and only a few fine scratches remained. To remove the surface cold-work introduced by mechanical polishing, the samples were electropolished in a 10% perchloric acid and 90% acetic acid solution for two minutes at room temperature. The amount of material removed in this process was about 2 microns. The samples are now ready to be irradiated.

4. Post-Irradiation Sample Preparation

The displacement profile produced from 14 MeV copper on CuPd is shown in Figure V-8. The Brice code[25] was used to calculate separately the damage profile for 14 MeV copper on pure copper and pure palladium with average displacement energy of 34eV and 50eV respectively. The damage profile for CuPd alloy system was then calculated by taking the arithematical mean of the two curves. This method was employed because the Brice code becomes extremely

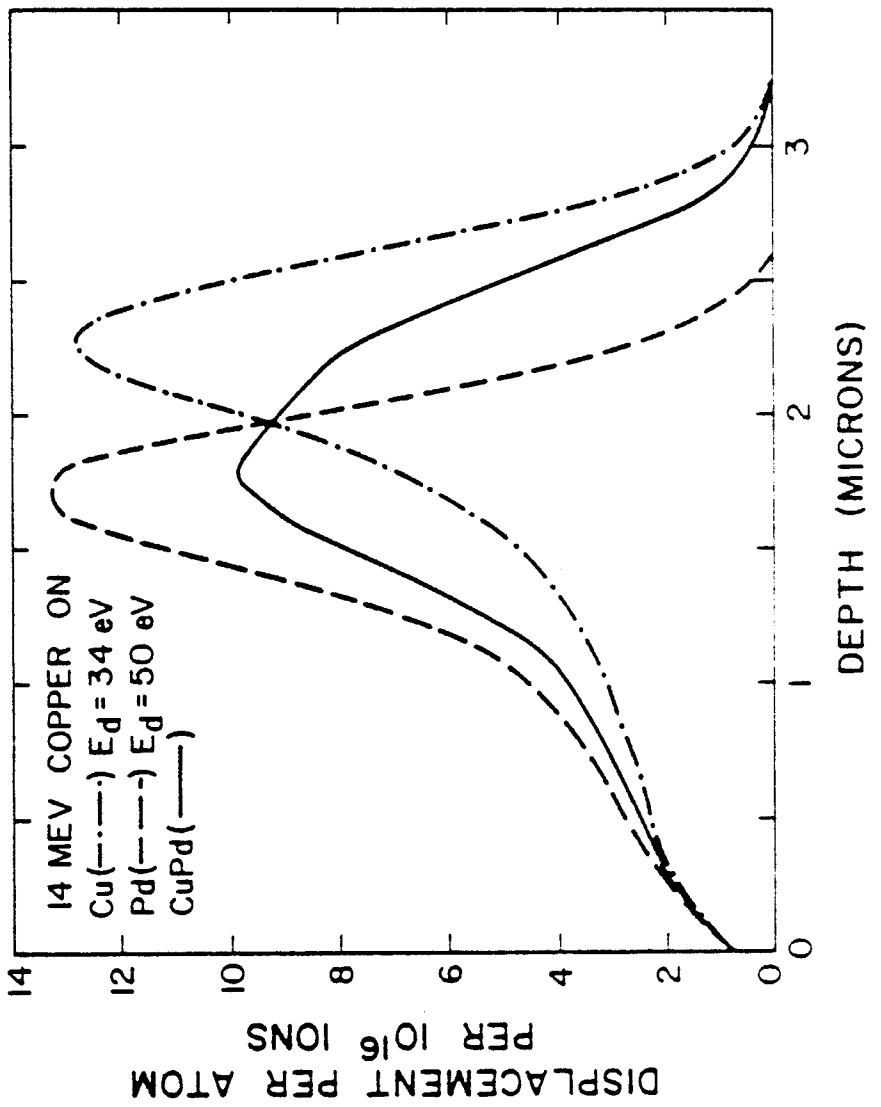

Figure V-8. Displacement profiles calculated using the Brice code for 14 MeV copper ions on Cu, Pd and CuPd.

expensive to run when applied to any alloy system irradiated with high energy ions. This approximation is quite valid because the main parameters of the code are the number density, the atomic number and atomic mass of the target. These parameters of CuPd are about the mean values of its components.

As shown in Figure V-8, only the first 3 microns of the material is damaged. It is desirable to examine the irradiated structure at a depth of around 1 micron where the damage profile is relatively flat but also far enough from the surface to eliminate any surface effect.

After irradiation, the outer portion of the sample was lacquered off with "Microshield" to expose only the central area. It was then electropolished at 23°C in a 10% perchloric acid and 90% acetic acid solution at 10V for thirty seconds. This process removed about 1 micron of the material as determined by counting the number of fringes shift in an interference microscope. The accuracy of this method was around ±0.2 micron. The polished surface was then lacquered off completely and the sample was back-thinned from the other side to perforation using the jet polishing techniques at room temperature. A polishing solution containing 25% perchloric acid and 75% acetic acid was used.

The specimens were then examined in a JEOL 100B transmission electron microscope operated at 120KV.

Post-irradiation annealing was performed on two samples. In-situ annealing inside the JEOL 100B was not possible due to the

malfunctioning of the hot stage. Therefore, annealing was done inside a ultra high vacuum furnace using radiactive heating (for a complete description of this furnace, see Ph.D. thesis of Weber[109]). The sample was loaded into a tantalum holder and heated to the desired temperature. The overall temperature fluctuation and uncertainty was about ±5°C. The system pressure at any time was maintained below 10^{-7} torr to avoid oxidation and other contaminations.

C. Fusion Neutron Irradiation

The 14.8 MeV fusion neutron irradiation was performed at the Rotating Target Neutron Source (RTNS-II) at Lawrence Livermore Laboratory[141] using resistivity measurement to monitor the degree of order. Two foil specimens, one highly ordered and one disordered were irradiated at 4.3°K to an integrated fluence of about 2×10^{17} neutrons/cm^2 with an average flux of $\sim10^{12}$ neutron/cm^2/sec. This will provide a measurement of the disordering rate alone since reordering process is inactive at such a low temperature. The samples then underwent an isochronal annealing up to room temperature to study the behavior of point defects. Six 3mm microscopy discs were also irradiated.

The samples were cooled by a commercially available "helitran" cryostat modified to hold six foil specimens. Figure V-9 shows the top view of the cold finger with all the samples in place.

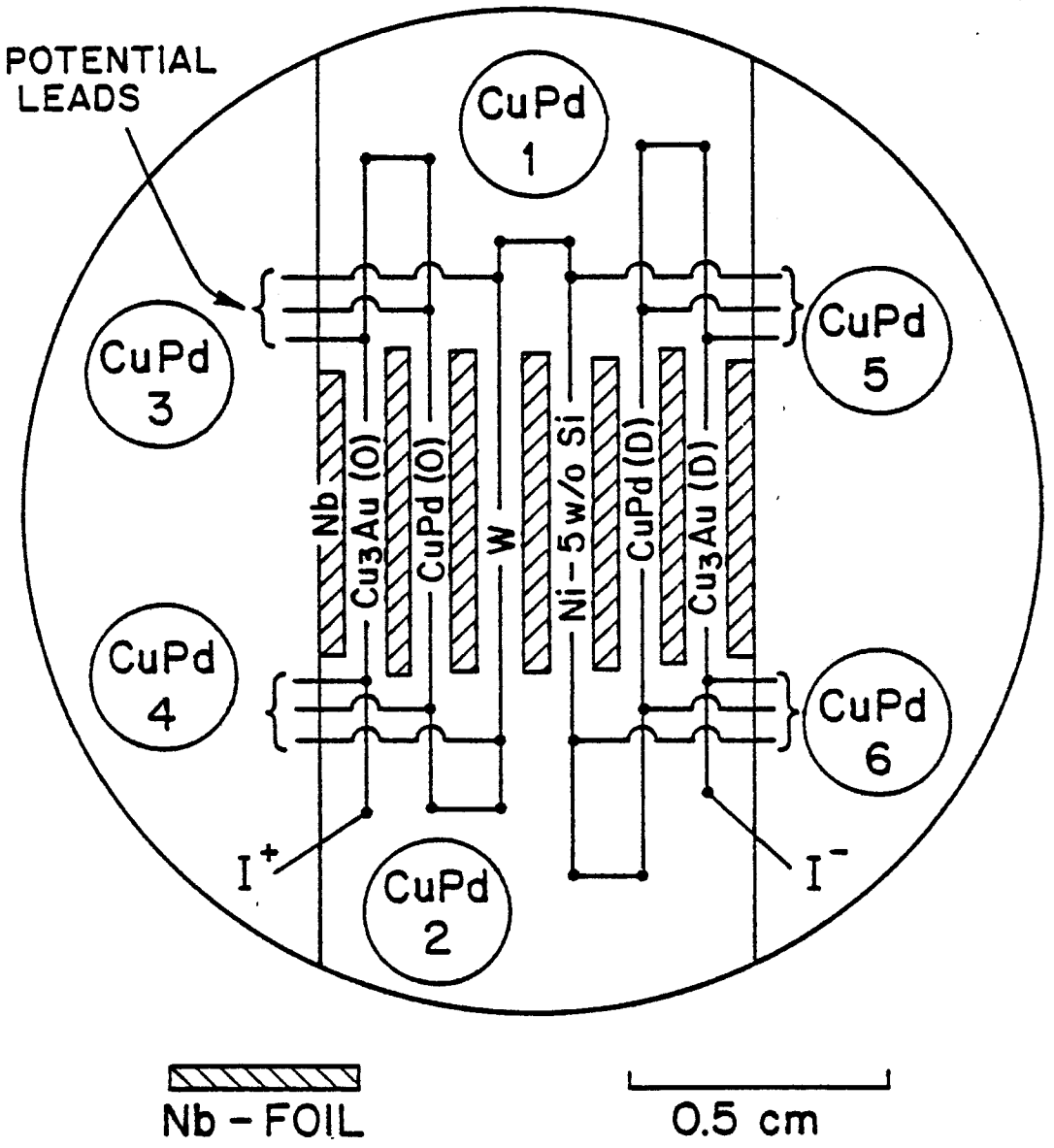

Figure V-9. Sample arrangement on the cold finger for 14.8 MeV neutron irradiation. Also shown are niobium dosimetry foils and six ordered CuPd microscopy samples.

The cold finger of the cryostat was made from a copper block. It was first coated with a thin layer of eproxy for electrical insulation. The six samples were then cemented on to ensure good thermal contact. In this run the six samples include a pair of ordered and disordered CuPd foils, a pair of ordered and disordered Cu_3Au foils, a tunsten foil and a Ni-Si foil. Copper wires were used to connect all the samples in series to provide a continuous current supply for 4-point resistance measurement. A set of potential leads were spot welded to each sample to measure the voltage drop.

The temperature of the cold finger was monitored by a pair of carbon glass resistors (CGR) from 4 to 50°K and by copper-constantan thermocouples from 50°K to room temperature. The cryostat was cooled by pumping liquid helium from a 100 liter dewar into the cold finger through a flexible transfer line. The measured temperature values had an uncertainty of $\pm$0.02°K.

The resistance of each sample was measured by a computerized data acquisition system. This system uses a Vidar 520 Digital Voltmeter and a Digital Equipment Corp. LSI-11 computer. The resistance of each sample was measured 10 times in both current directions to eliminate any emf induced by dissimilar junctions. The resistance value measured with this system had an uncertainty of less than $\pm$0.05%. The computer also measured an internal standard resistor, the carbon glass resistor and the thermocouple readings for temperature measurement as well as neutron count. A complete of such reading was taken once every 15 minute during irradiation.

The total fluence on each sample was measured by the activation of seven niobium foil sandwiched between samples as shown in Figure V-9. The niobium foil was activated by the nuclear reaction $^{93}Nb(n,2n)^{92}Nb$ with a cross section of 458 mbarn. Neutron output during irradiation was recorded using a proton recoil counter.

After irradiation, the samples were annealed isochronally to room temperature. A small heater was mounted on the cold finger for annealing.

Six 3mm-diameter discs of ordered CuPd were also irradiated in the same run. These discs were cemented on different locations of the cold finger as shown in Figure V-9. Each disc was covered with a niobium foil to measure the total neutron fluence. After irradiation, these samples were electropolished and examined under the TEM at University of Wisconsin.

The 14.8 MeV fusion neutrons were produced by the RTNS-II irradiation facility (for a brief description of this system, see reference 153). A 400KV Crockcroft-Walton air insulated accelerator was used to produce a 150mA dueteron beam. Fusion neutrons were produced by the D-T reaction of this deuteron beam with a copper target coated with titanium tritide. The target rotated at 5000rpm and continuously cooled by running water to prevent overheating.

To convert the measured resistances (R) to resistivity values (ρ) the following equation is used.

$$\frac{R}{\rho} = \frac{L}{A} = \frac{dL^2}{W} \qquad (V\text{-}1)$$

where L is the gauge length of the foil measured between the voltage leads. A is the cross-sectional area, W is the weight of the specimen and d is the density of the material. The density can be obtained by using the lattice parameter data measured experimentally using x-ray technique.

D. Electron Irradiation

Electrical resistivity measurement was used to determine the change in degree of order of an ordered CuPd foil under electron irradiation.

In the heart of the irradiation system was a Van de Graaff electron accelerator. This accelerator could produce an electron beam between 1 and 2 million volts at a maximum current of 300 microampere. Figure V-10 shows schematically the beam line components of the accelerator facility in proper sequence. The accelerator (2UEH) was made by National Electrostatic Corp. It was a single ended machine with two charging motors each driving two pelletron chains to charge the high voltage terminal to the desired voltage. To provide power for the electron source and various supplies in the high voltage terminal, a 400 hertz generator capable of delivering 500 watts of power was used. This generator was driven by a 3 horsepower motor at the ground terminal via a lucite rod.

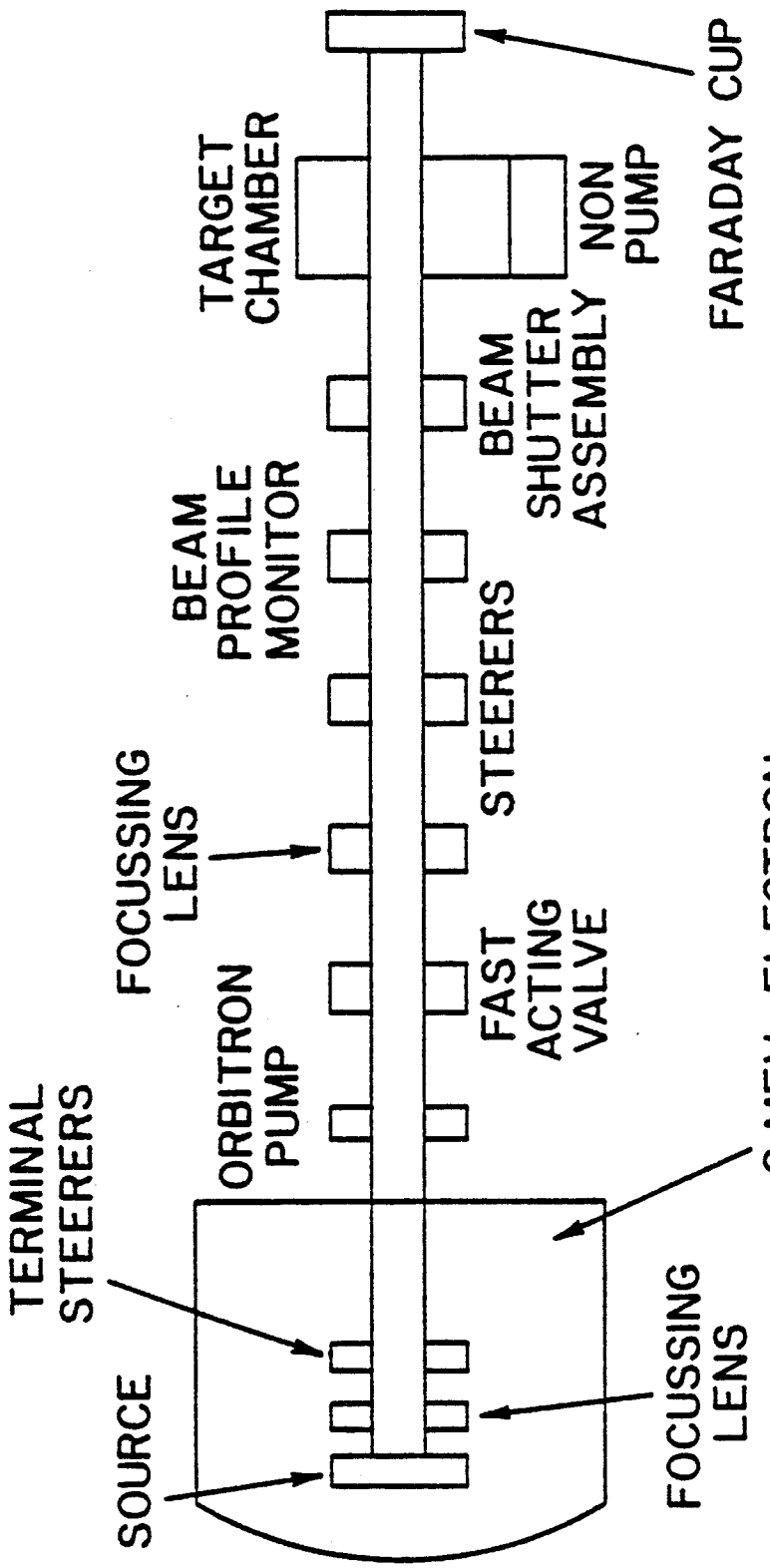

Figure V-10. Main components of the 2 MeV electron irradiation facility.

At the high voltage end, the electron beam originated from a tunsten filament by means of thermal emission. It then passed through an einzel lens to obtain the proper focussing conditions. Two sets of magnetic steerers at the terminal then steered the beam all the way out of the accelerating tube. To control the power to the filament, lens and steerers, four servo motors at ground terminal were used to adjust four independent variacs at the high voltage deck through connecting lucite rods. The beam tube (or accelerating tube) between the high voltage end and ground was made up of six accelerating tube sections each with alternating metal-ceramic rings bonded together. The machine was enclosed in a tank, 4 meters long and 2 meters in diameter. It was pressurized with sulfur hexafloride gas for voltage insulations. A getter ion pump location just outside the tank was used to maintain the beam tube at a vacuum of 10^{-8} torr.

When the beam emerges from the accelerating tube, it encountered a magnetic lens and two more sets of magnetic steerers similar to those at the terminal. This gave a better control of the beam direction in the specimen area. A beam profile monitor was used to display the profile of the beam in both the vertical and horizontal directions on an oscilloscope. At about 15 cm in front of the sample, there was an aperture to define to the beam on target. Immediately behind this aperture was a retractable Faraday cup. A high vacuum rotary feedthrough was used to move the cup into and out of the beam path. Both the aperture and the cup

were capable of measuring beam intensity. Before actually irradiating the specimen, the cup was moved into the beam path. With the current readings on this cup and aperture together with the beam profile display, the beam could be properly tuned. The cup was then removed and the beam reaches the sample. Behind the sample was another Faraday cup and aperture set to provide information of the beam after leaving the sample. A second ion pump (ULTEK 220 liter/sec D-I) was used to evacuate the target chamber to 10^{-8} torr.

The terminal voltage, beam intensity, the two focussing and steering systems and the motion of the retractable Faraday cup were all controlled remotely at the control console.

The temperature of the specimen was to be maintained close to liquid nitrogen temperature during irradiation. Figure V-11 is a sketch of the sample chamber designed for this purpose. The sample was mounted vertically as shown. It was clamped to a copper base-plate with ceramic insulators. The sample holder was connected to a 30 cm diameter stainless steel flange through a 33 cm long, 7 cm diameter thin wall stainless steel tube. Thin wall tube was required to minimize amount of heat transfer. All the joints were either silver soldered or welded to prevent vacuum leak due to temperature cycling. The sample holder was kept at low temperature by maintaining about 7 cm of liquid nitrogen at the bottom of the thin wall tube. This was accomplished by using a liquid nitrogen automatic level controller. The sample holder was

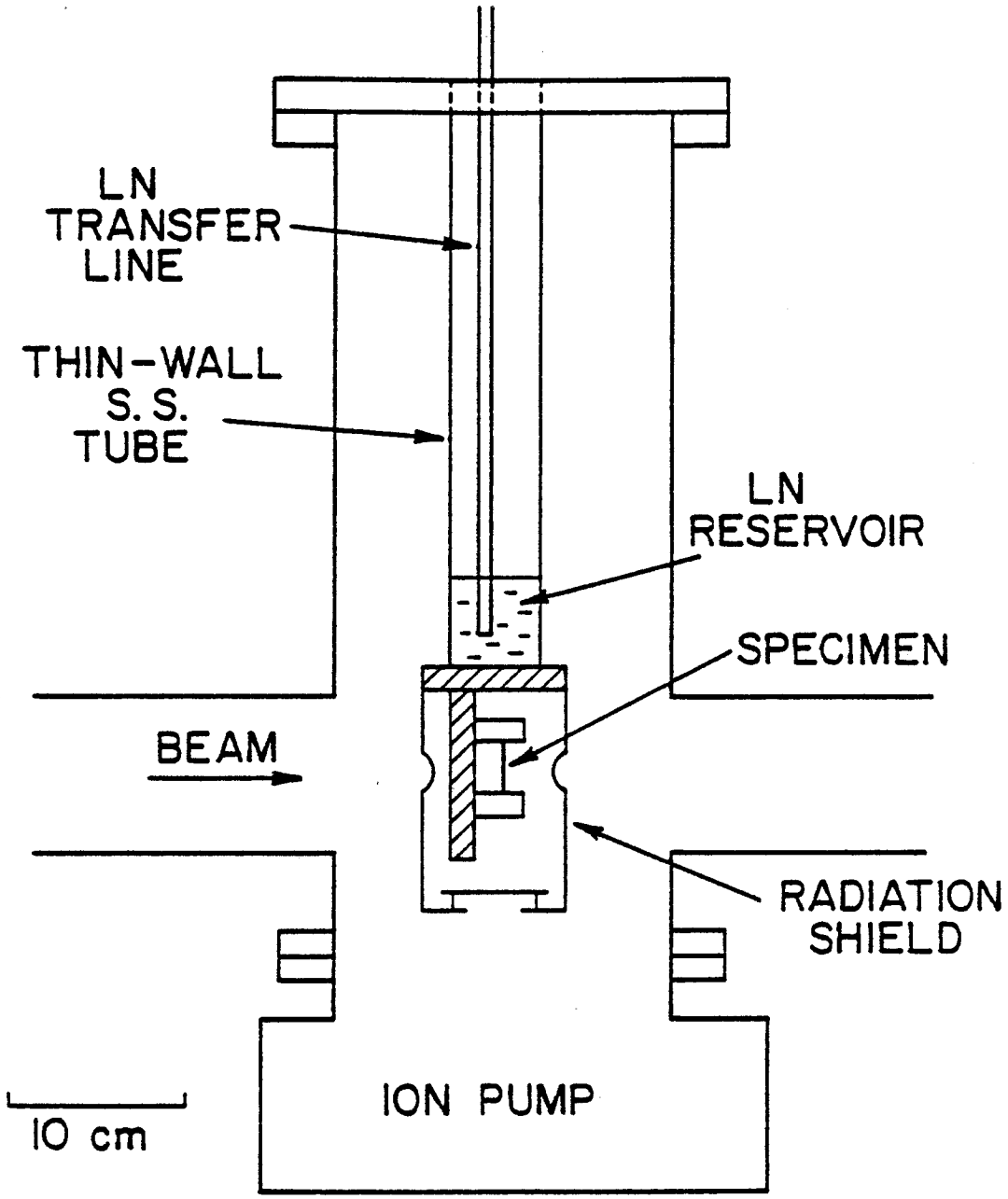

Figure V-11. Sample chamber for low temperature electron irradiation.

enclosed in a 10 cm diameter copper can which served as a radiation shield to reduce heat transfer.

Since the resistivity was a linear function of temperature, the sample temperature rise due to beam heating could be monitored by measuring the resistance of the sample during irradiation. The beam current was maintained at 10 uA/cm^2 during the run so that the maximum temperature did not exceed 100°K.

The resistance of the sample was measured by a 4-point technique. A power supply (HP-6286A) was used to produce current up to 50mA. The exact current was monitored by a 4-1/2 digits ammeter. The voltage drop across the sample was measured by a 4-1/2 digits nanovoltmeter (Keithley 180). It was found that the heating induced by the current became significant only at currents above 35mA. Therefore all the data were taken with current ranging from 2 to 30mA. The readings with both current directions were taken to eliminate any induced emf effect. Each final resistance value was obtained by averaging over 100 data points. This method gave an accuracy better than 0.05%. All the readings were taken at least five hours after each irradiation to ensure the entire system had reached its equilibrium condition.

A post-irradiation annealing experiment was performed from room temperature (23°C) to 200°C at 50°C intervals. After irradiation, the sample was allowed to warm up inside the target chamber to 23°C. After sitting there for 100 hours, it was cooled down to 77°K to measure the resistivity. It was then warmed up and

removed from the target holder and mounted on a separate resistance measurement device for higher temperature annealings. A horizontal furnace was used for the annealing. The sample remained at each desired temperature for thirty minutes. The temperature fluctuation inside thefurnace is $\pm 5°C$. After each annealing, the sample was quenched into liquid nitrogen for a resistance measurement.

VI. EXPERIMENTAL RESULTS

The results of all the experimental work will be presented in this chapter with their significance discussed in the next. Both chapters are divided into three sections, namely: ion, neutron and electron irradiations.

A. Heavy Ion Irradiation

All the samples bombarded with heavy ions used the transmission electron microscopy method to analyze the state of order as well as the damage structure of the materials after irradiated with 14 MeV copper ions. Irradiations had been carried out from room temperature (23°C) to 550°C. It is more convenient to subdivide these results into three groups according to temperature. Group 1 covers the temperature range from 23°C to 110°C (low temperature range); group 2 from 300°C to 550°C (high temperature range) and group 3 from 200°C to 250°C (intermediate temperature range). The result from irradiations at intermediate temperatures is chosen to be discussed last because these are the temperatures at which there is a transition from disordering at low temperatures to reordering at high temperatures.

1. Group 1 (23°C - 110°C)

All the samples in this group were irradiated using the low

temperature aluminum holder. Twenty one samples were irradiated in this group and all were successfully electropolished and analysed on the T.E.M. Table VI-1 gives the temperature, dose rate and total dose in terms of ions/cm^2 and calculated dpa using the Brice code at one micron depth. The order of the as-irradiated state is also given. All these samples were initially ordered. This is the only group in which different doses were used for each temperature so that the approach to the final saturated defect structure can be obtained.

Thirteen initially ordered samples were irradiated at 23°C. Of these, nine of them were irradiated at a higher dose rate ($\sim 10^{-3}$ dpa/sec) than the rest ($\sim 2 \times 10^{-4}$ dpa/sec). The lower dose rate was used only at this temperature (23°C) to study the effect of dose rate if any. However, only a factor of five difference in dose rate is used because of two reasons. First, the unacceptably long irradiation time required to obtain any reasonable dose. Secondly, the beam current intensity is basically controlled by a source which is not designed to operate at too low an output. The samples with higher dose rate were irradiated from 0.05 dpa to 5.0 dpa whereas the ones with lower rate from 0.06 dpa to 1.3 dpa. The results from the higher rate irradiations will be presented first followed by those from the lower one for comparison.

Figure VI-1 gives the damage structure of a sample irradiated at 23°C to 0.64 dpa at a rate of 10^{-3} dpa/sec. The diffraction pattern is included in the insert. This microstructure and its diffraction pattern are representative of those samples irradiated

TABLE VI-1

Summary of Irradiation Parameters For Group 1

Run	Sample*	Irradiation Temp (C)	Fluence 10^{15} ions/cm^2	dpa**	Dose Rate dpa/sec**	Final Damage State
1	1	23	0.13	0.05	1.3×10^{-3}	Ordered and disordered material coexist. (100) superlattice reflection still strong.
1	2	23	0.23	0.09	1.5×10^{-3}	Completely disordered. Saturated with damage colonies.
1	3	23	0.34	0.13	1.3×10^{-3}	Mostly disordered material. Still has weak (100) superlattice reflections.
2	4	23	0.68	0.26	1.3×10^{-4}	(a)
2	5	23	0.71	0.27	1.4×10^{-3}	(a)
2	6	23	1.7	0.64	1.0×10^{-3}	(a)
2	7	23	3.4	1.3	1.0×10^{-3}	(a)
2	8	23	6.8	2.6	9.7×10^{-4}	(a)

TABLE VI-1 (cont.)

Run	Sample*	Irradiation Temp (C)	Fluence 10^{15} ions/cm^2	Fluence dpa**	Dose Rate dpa/sec**	Final Damage State
2	9	23	13	5.1	9.5×10^{-4}	(a)
3	10	23	0.16	0.06	1.8×10^{-4}	Highly ordered. Damage in the form of microtwins.
3	11	23	0.84	0.32	1.9×10^{-4}	(a)
3	12	23	1.7	0.64	1.8×10^{-4}	(a)
3	13	23	3.4	1.3	1.8×10^{-4}	(a)
4	14	67	0.34	0.13	1.5×10^{-3}	Still has a slight trace of order remaining. Very weak (100) superlattice reflections.
4	15	67	2.0	0.76	1.4×10^{-3}	(a)
4	16	67	5.0	1.9	1.3×10^{-3}	(a)
4	17	67	14	5.5	1.4×10^{-3}	(a)
5	18	110	0.50	0.19	1.2×10^{-3}	(a)
5	19	110	2.4	0.90	1.3×10^{-3}	(a)

TABLE VI-1 (cont.)

Run	Sample*	Irradiation Temp (C)	Fluence 10^{15} ions/cm^2	dpa*	Dose Rate dpa/sec**	Final Damage State
5	20	110	5.0	1.9	1.4×10^{-3}	(a)
5	21	110	14.0	5.3	1.3×10^{-3}	(a)

* All the samples in this group are initially ordered.

** At the region of T.E.M. analysis (~one micron from surface) (average value).

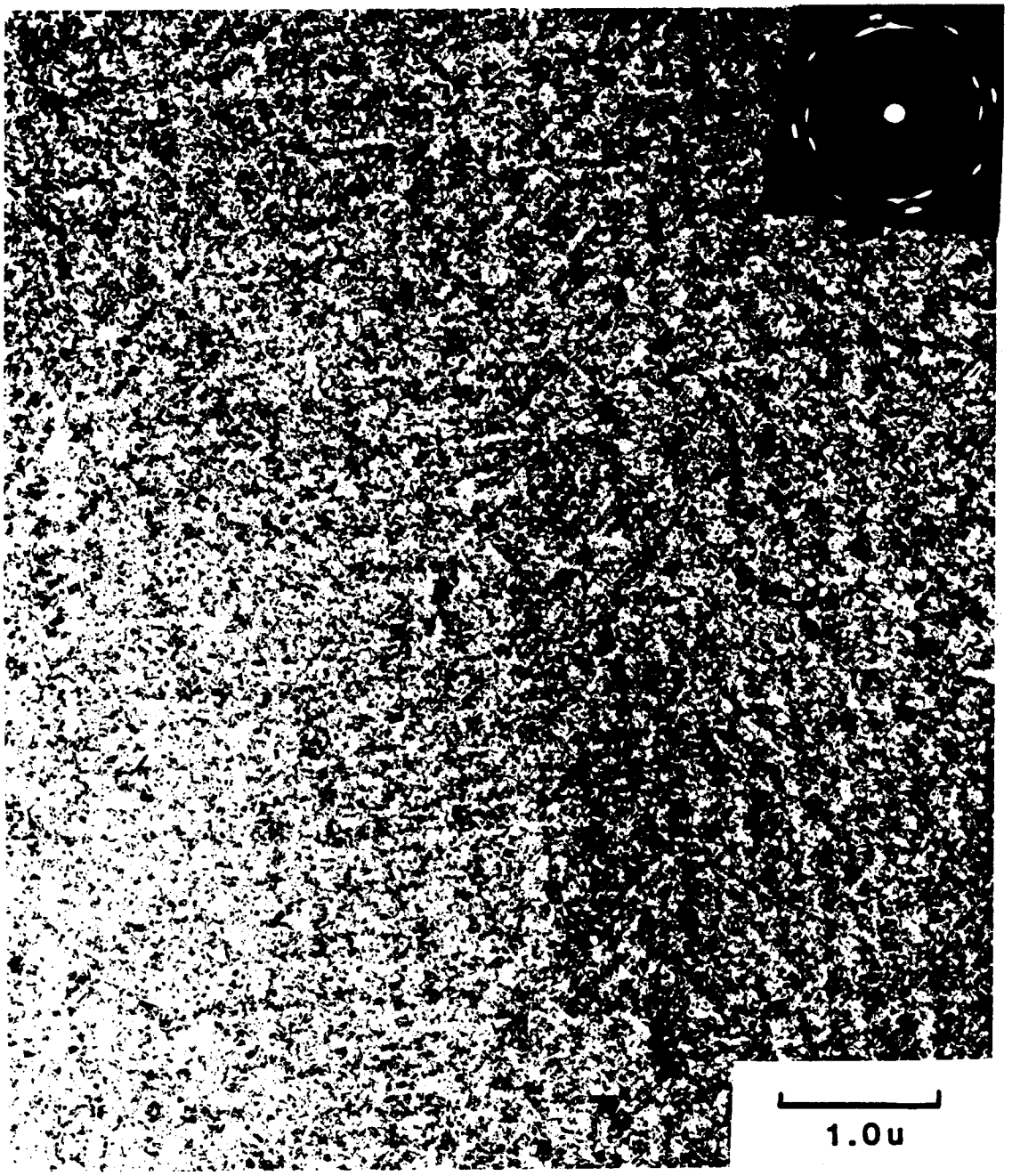

Figure VI-1. Damage structure shown in bright field of an initially ordered CuPd sample irradiated with 14MeV copper ions at $23^{o}C$ to 0.64dpa at a rate of $1.0x10^{-3}$dpa/sec. Selected area diffraction is shown in insert.

under similar conditions but to higher doses (1.3, 2.6 and 5.1 dpa). The set of diffraction spots closest to the transmitted beam has a lattice parameter corresponding to the (100) spacing of the disordered f.c.c. phase as obtained by quenching the alloy from above the transition temperature. This (111) spacing is, of course, the shortest in the reciprocal space for the f.c.c. crystal structure. The next set of diffraction spots has the corresponding (200) spacing also of the disordered α phase. No superlattice spot or any fundamental reflection corresponding to the B2 ordered phase is detected.

The bright field image of the damage in Figure VI-1 shows slight periodicity in alternating dark-white contrast with a spacing of $\sim$0.1 micron. This periodicity effect should give rise to extra spots in the diffraction pattern with a reciprocal length of $\sim 10^{-3}$ $\mathring{A}^{-1}$. However, this length is extremely small and therefore impossible to resolve.

The defect structure is so extensive that little analysis can be performed using the transmitted beam. Therefore, a dark field imaging technique is employed to obtain more detailed analysis. Figure VI-2 shows the bright field image at higher magnification taken from different area of the same specimen as in Figure VI-1. High resolution dark field imaging technique was applied to all the diffraction spots corresponding to the (111) and (200) plane spacings. A set of four representative dark field micrographs are given in Figure VI-3 using diffraction spots A,B,C and D as indicated

Figure VI-2. Same specimen as in figure VI-1. but different area and at a higher magnification.

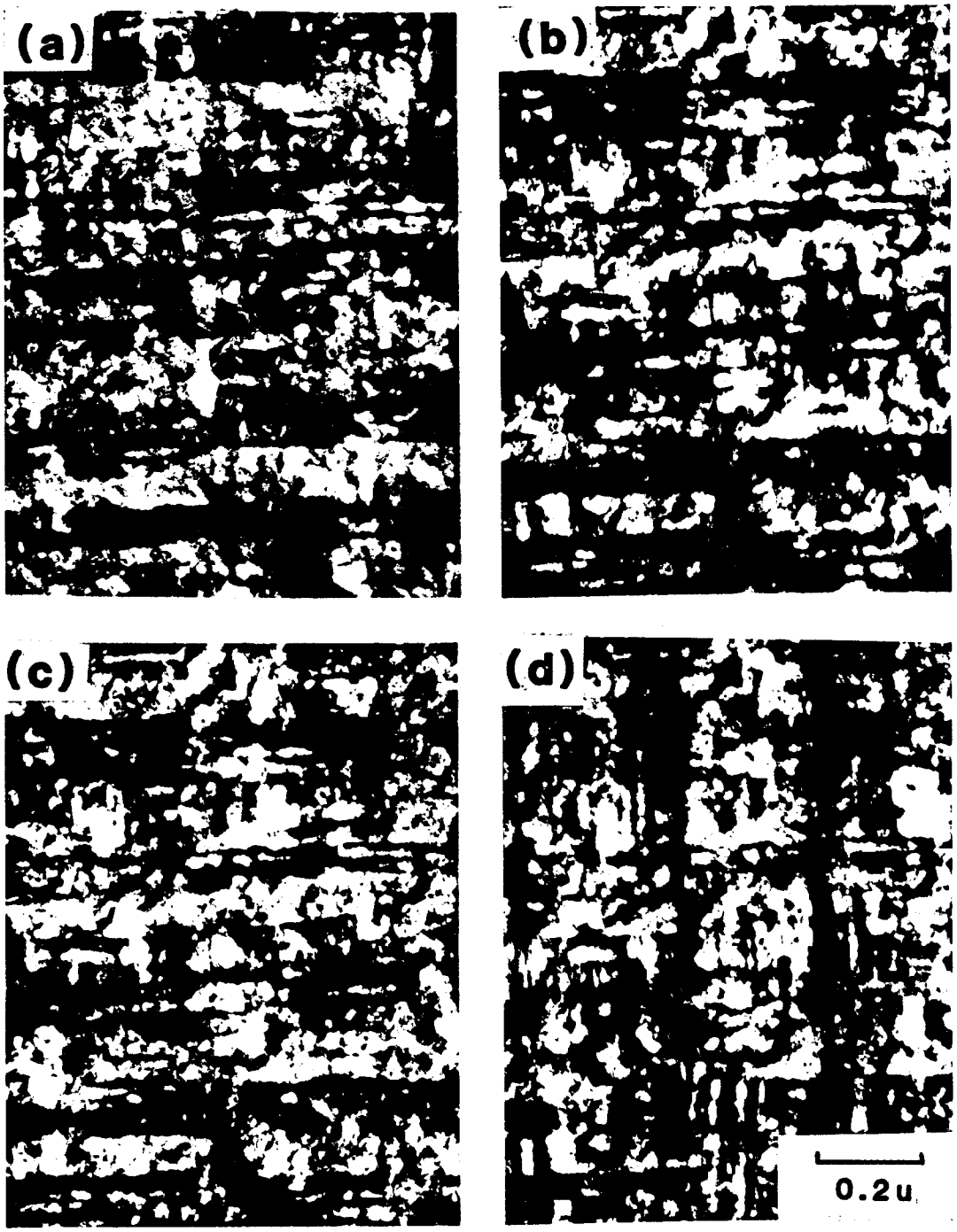

Figure VI-3. High resolution dark field images of the area in figure VI-2 using diffraction spots A,B,C,D as indicated in the diffraction pattern in figure VI-2.

in the diffraction pattern of Figure VI-2. These dark field images were taken from the same area as Figure VI-2. The angle measured between spots A and B is about 20° and about 70° between C and D. The dark field images using spot B is identical to that using spot C but is completely different to all the others. The alternating dark-white regions obtained using spot A are also the exact opposite of those using spot B as shown in Figure VI-3a and b. This indicates that the damage structure has only $\pm g$ symmetry. These dark field images also show that the damage structure seems to be aligned in the direction parallel to the image reflection spot. This alignment between the microstructure and its diffraction pattern can also be found in Figure VI-1. There also exists a periodicity in damage structure with a period of 0.1 micron similar to that observed in Figure VI-1.

The damage structure in Figure VI-2 consists mainly of little "cluster"-like defects of about 0.1 micron in diameter, which will be called "colonies". These small colonies also contain internal damage which resemble microtwinning and internal faulting. This internal damage inside the colonies has an average size of about 40Å. All the diffraction spots in the diffraction pattern are elongated with a major length of about $0.04 Å^{-1}$. Assuming that this elongation in reciprocal space is due to the presence of finite size diffracting zones (shape streak),this elongation corresponds to a size in real space of $\sim$25Å. Very weak diffraction spots can be seen around the center spot in the diffraction pattern. The

spacing of these spots also indicates a periodicity of around 25Å.

These internal faulting and twinning structures are shown in better detail in Figure VI-4. This figure is obtained from a sample irradiated also at 23°C at a rate of 1.3×10^{-3} dpa/sec but only to 0.26 dpa. The overall microstructure is similar to that of the higher dose sample. The diffraction pattern associated with this microstructure appears slightly different than that shown in Figures VI-1 and 2. This is just due to a slight difference in orientation. These diffraction spots are also not discrete but elongated similar to those of the higher dose samples. However, some of the area of the same sample also exhibits descrete diffraction spots as shown in Figure VI-5. The spots arrowed correspond to the diffraction pattern of the disordered f.c.c. phase with a [001] zone axis. The main set of diffraction spots is also labelled. The bright field image giving this diffraction pattern shows that the damage is also very extensive. The damage structure is very much aligned in the [220] direction with a characteristic spacing of 0.1 micron. High resolution dark field analysis using any one of the arrowed spots shows a contrast reversal of the bright field image.

The two different damage states shown in Figure VI-4 and 5 always appear in different grains. Again no superlatttice reflections can be found indicating the material is completely disordered by irradiation. The as-irradiated microstructure of the sample irradiated to 0.27 dpa is identical to that of the 0.26 dpa structure

Figure VI-4. Bright field micrograph showing damage structure of an initially ordered specimen irradiated at 23°C to 0.26dpa at 1.3×10^{-3} dpa/sec including the diffraction pattern.

Figure VI-5. Same as figure VI-4 but taken from a different area.

just discussed.

The last three samples irradiated at 23°C at a rate of $\sim 10^{-3}$ dpa/sec received doses of 0.13, 0.09 and 0.05 dpa at a depth of one micron. The 0.05 dpa sample has a typical diffraction pattern and damage structure as shown in Figure VI-6. The diffraction pattern has the normal disordered elongated spot pattern characteristic of the higher dose samples. However, superimposed are relatively strong discrete spots (spot A). The lattice parameter corresponding to these spots indicates that they are the (100) superlattice reflections of the ordered B2 phase. The bright field image (Figure VI-6) shows that the damage structure is slightly different from that at higher doses in the sense that the disordered colonies are now not as well defined. It is now saturated mainly with an inter-weaving line type damage. Sharp parallel faulting lines with spacing of $\sim$50Å can be seen. These are similar to the internal faulting found in the disordered colonies (Figure VI-4). Figure VI-7 a and b show a set of dark field micrographs of the same area as Figure VI-6 using the (100) superlattice reflection (spot A) and disordered spot B. The bright area in Figure VI-7a is the material that is still highly ordered. The damaged (disordered) area is relatively aligned. The dark field image using disordered spot B is quite similar to that obtained at higher damage level with a well aligned structure parallel to the diffracting g. (Figure VI-3).

The same type of diffraction pattern and microstructure are

Figure VI-6. Bright field micrograph showing damage structure obtained from an initially ordered specimen irradiated at $23^{o}C$ to 0.05dpa at a rate of $1.4x10^{-3}$dpa/sec. The corresponding diffraction pattern is shown in the insert.

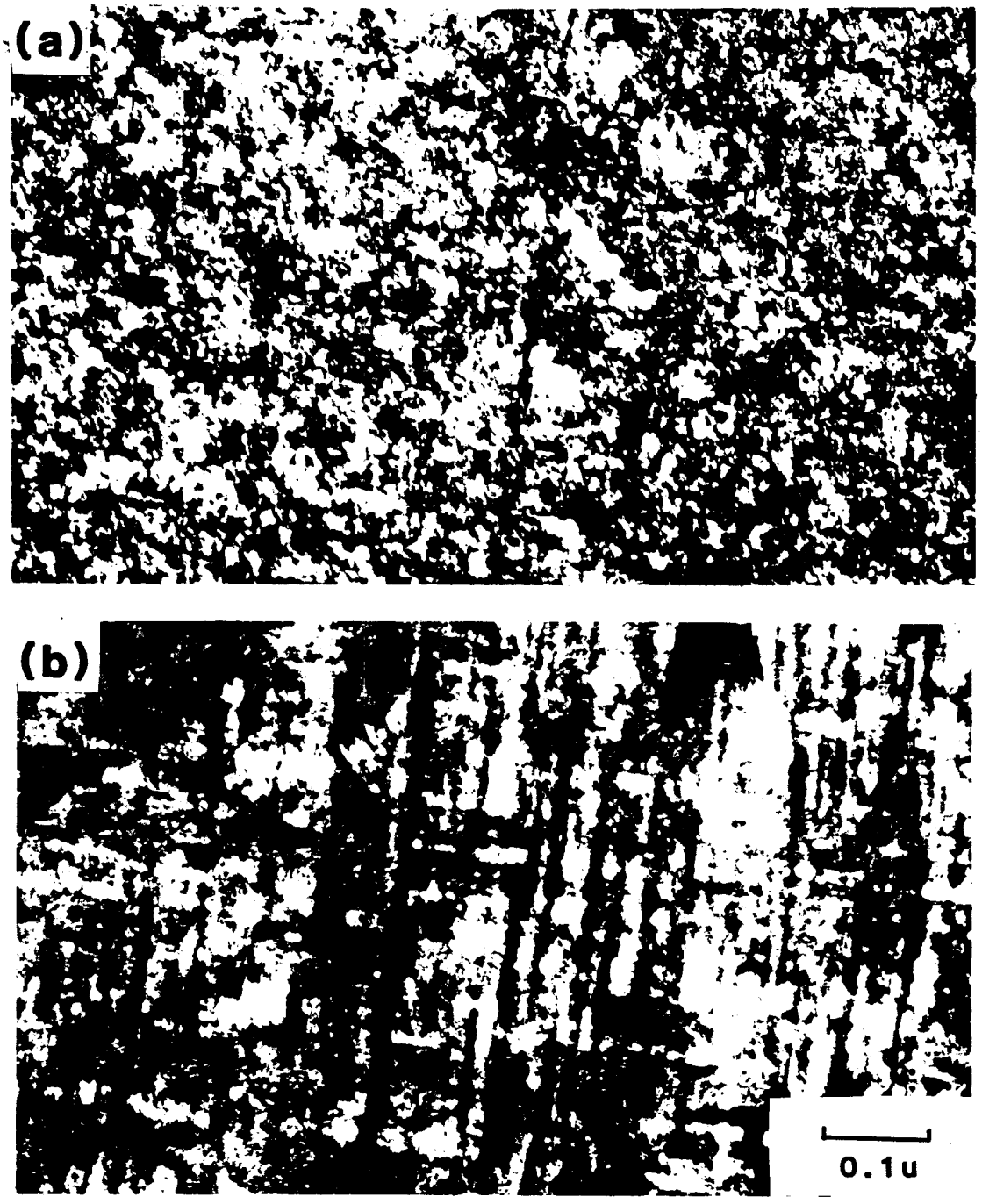

Figure VI-7. High resolution dark field images of the area in figure VI-6 using (a) diffraction spot A and (b) diffraction spot B as indicated in the diffraction pattern.

found in the sample irradiated to 0.13 dpa under similar conditions. However the amount of ordered material remaining is smaller since the intensity of the (100) superlattice reflection is extremely weak. One observation worth mentioning is that there always exists a definite correlation between the superlattice reflection and the disordered pattern as indicated in Figure VI-6.

The sample irradiated to 0.09 dpa on the other hand does not exhibit any superlattice reflection at all. It has all the characteristics of those samples irradiated to saturation doses. This is probably because too much surface is removed in the process of electropolishing. Thus the area of examination actually receives a higher dose than expected.

The results of the samples irradiated at a lower dose rate ($\sim 2\times10^{-4}$ dpa/sec) will now be presented. Four samples are involved in this run with doses of 1.3, 0.64, 0.32 and 0.06 dpa at a depth of one micron from the irradiated surface. The three higher dose samples (0.32 to 1.3 dpa) all show the same saturated damage structure as those irradiated at the higher dose rate. Figure VI-8 shows the microstructure obtained from the 0.64 dpa sample but is also representative of the other two (0.32 and 1.3 dpa). The damage area in this micrograph is selected at a grain boundary. The diffraction pattern associated with this structure is similar to that in Figure VI-1. The diffraction pattern undergoes a rotation when the diffraction aperture is moved across the grain boundary. Figure VI-9 is taken from the same sample but at a higher

Figure VI-8. Bright field image of the damage structure at a grain boundary irradiated at 23°C to 0.64dpa at a damage rate of 1.8×10^{-4} dpa/sec.

Figure VI-9. Same as figure VI-8 but at higher magnification showing detailed disordered structure.

magnification showing the damage in better detail.

The only sample irradiated at 23°C that does not show any disordered spots is that irradiated to 0.06 dpa at 1.8×10^{-4} dpa/sec. The diffraction pattern of this sample is shown in the insert of Figure VI-10. It corresponds to the pattern of the B2 ordered structure with a [001] zone axis. The (100) superlattice reflection (spot A) is very intense indicating that the material is still highly ordered. Notice the satellite reflections about some of the basic spots. Unfortunately, these satellite spots are too weak and all efforts to obtain a dark field image from them failed. Figures VI-10 and 11 show the bright field and dark field images using the (100) superlattice reflection (spot A) of the same area. The bright field micrograph shows that basic damage structure which includes tangled dislocations. The dark field image reveals that the ordered region (bright area) contains uniform parallel striations in the [100] direction. These striations are microtwins that also result in the satellite reflections observed.

Four samples were irradiated at 67°C. They were irradiated at a rate of $\sim 10^{-3}$ dpa/sec to doses of 0.13, 0.76, 1.9 and 5.5 dpa. Samples with doses at the above 0.76 dpa all exhibit similar damage structure as those samples irradiated at 23°C to saturation doses discussed earlier. A bright field micrograph showing the damage state of the sample irradiated to 1.9 dpa is given in Figure VI-12. The shape of the disordered colonies seems to be more uniformly aligned and elongated than that observed

Figure VI-10. Damage structure shown in bright field of an initially ordered sample irradiated at 23°C to 0.06dpa at 1.8×10^{-4}dpa/sec. Spot A of the diffraction pattern is a (100) superlattice reflection.

Figure VI-11. High resolution dark field image of the same area in figure VI-10 using the (100) superlattice reflection.

at lower temperature. The overall size of these colonies and the internal damage within them is similar to that seen at lower temperature. Internal faulting is clearly visible. The insert in Figure VI-13 is a diffraction pattern representative of this group of samples. The two sets of spots closest to the origin possess the correct spacings for the (111) and (200) planes of the disordered f.c.c. phase. Even though this pattern is different from that of Figure VI-1, this is only an orientation effect since the diffraction pattern of the latter can also be obtained by proper tilting.

A high resolution dark field analysis was also performed on this sample. The bright field image of the chosen area is shown in Figure VI-13a. Figures VI-13b and 14a and b give the dark field images using spots A, B and C of Figure VI-13 respectively. These dark field images show the array of colonies which give rise to the diffraction spots. As it is the case in the 23°C irradiation, symmetry exists only for $\pm g$.

Only one sample irradiated at 67°C still contains any trace of order after irradiation. This sample received 0.13 dpa. The slight order remaining is evident by the presence of extremely weak (100) superlattice reflections (arrowed) shown in the insert of Figure VI-15. The basic damage structure of this sample is also shown in this figure. The damage state is quite similar to that found in the one irradiated at 23°C to the same dose.

To complete the dose scan at low temperatures, four samples were

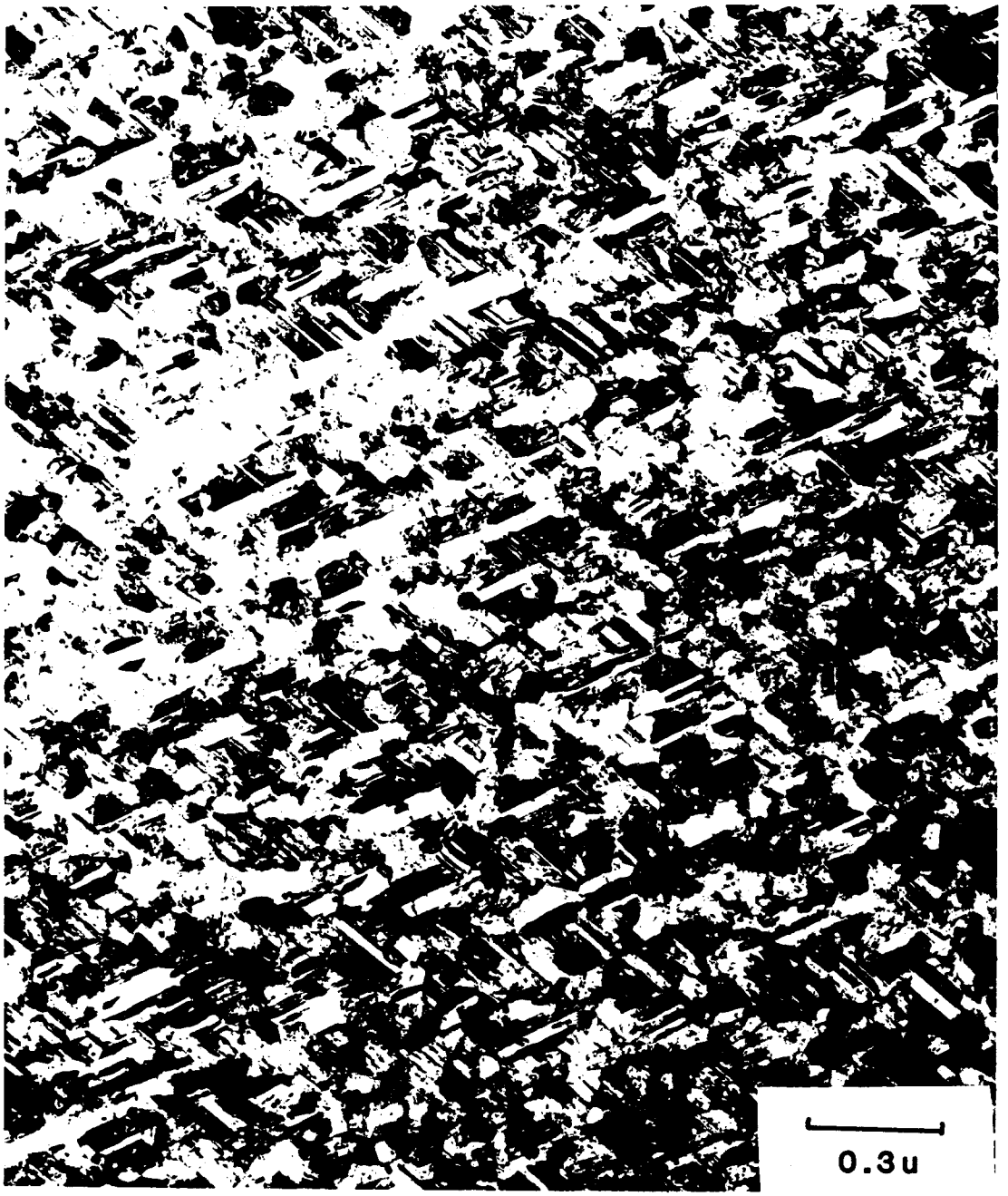

Figure VI-12. Damage structure in bright field of an initially ordered sample irradiated at 67°C to 1.90dpa at a rate of 1.3×10^{-3} dpa/sec.

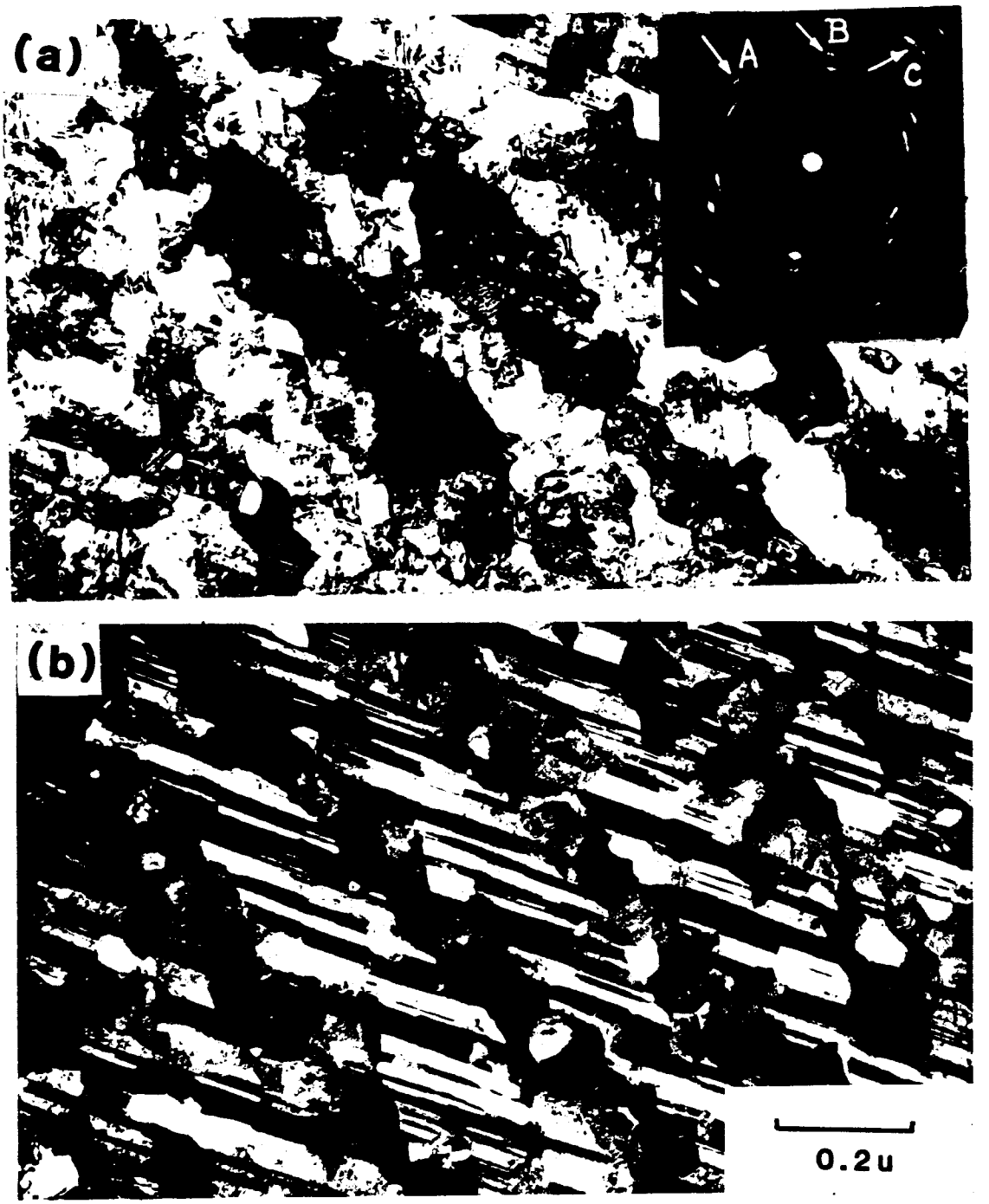

Figure VI-13. Same specimen as in figure VI-12. (a) Bright field image at higher magnification and (b) high resolution dark field image of the same area using diffraction spot A in figure .

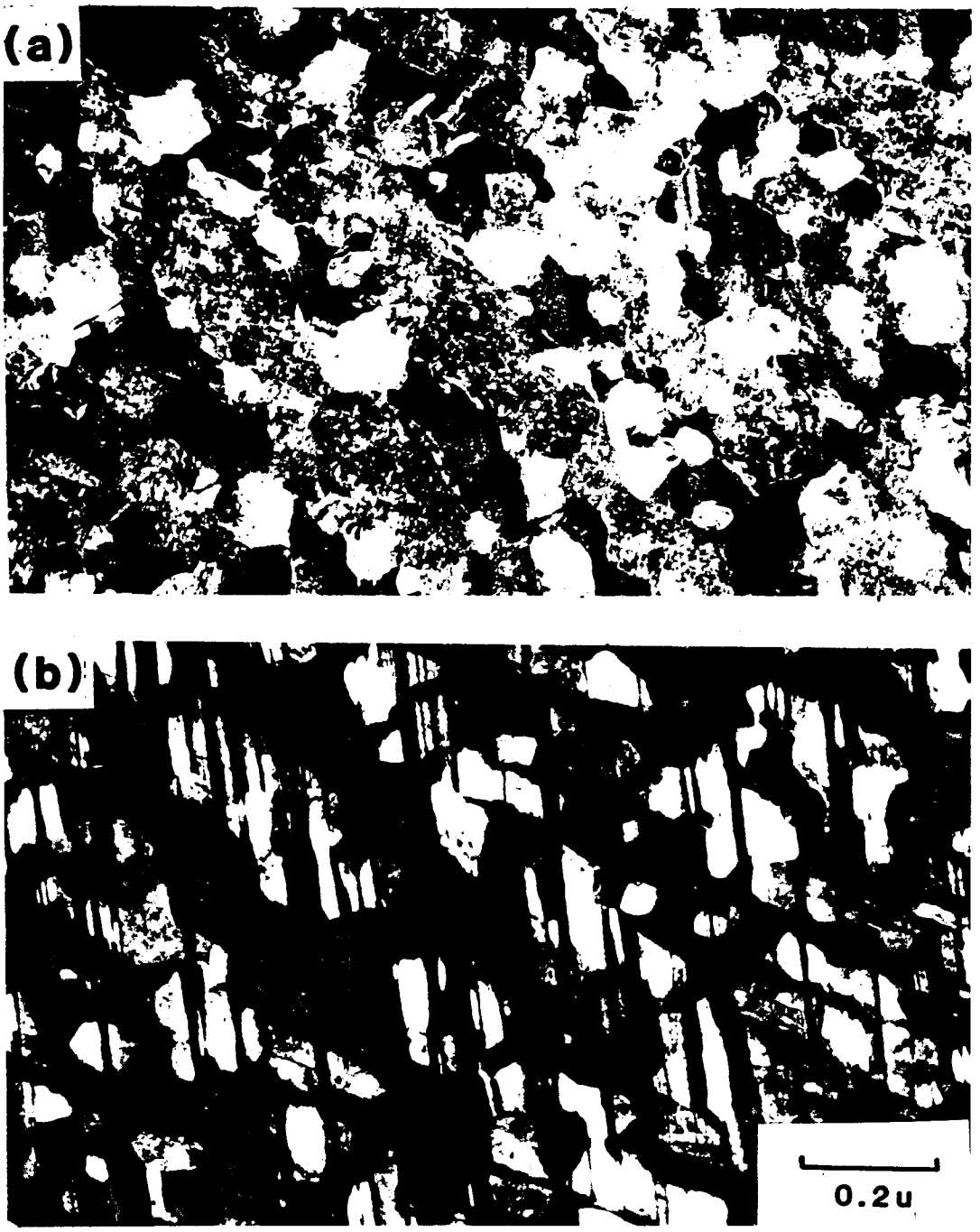

Figure VI-14. Same as figure VI-13b but using diffraction spots (B) and (C).

Figure VI-15. Bright field micrograph of the damage structure of an initially ordered sample irradiated at 67°C to 0.13dpa at 1.5×10^{-3}dpa/sec. The diffraction pattern in insert shows faint (100) superlattice reflection.

irradiated at 110°C to doses of 0.19, 0.90, 1.9 and 5.3 dpa. No superlattice reflection is detected in any of these samples. Their diffraction patterns are all similar to those irradiated to saturation doses at lower temperatures. However, at proper tilting of the specimen, very weak diffuse diffraction streaks appear in addition to the main disordered elongated spots. These diffuse streaks are not seen in any of the lower temperature samples. These are probably shape streak (due to finite size of the colonies). These streaks seem to be breaking up into spots which can be due to the formation of periodic colonies. Parallel streakings are also found around the center spot. These are also shape streaks arising from the same phenomenon just described. Both the streak length and the spacing of the streaks from the center spot indicate the same colony size and periodic spacing are both $\sim$20Å. Figure VI-16 also shows the typical damage microstructure induced in these samples by irradiation.

This concludes the systematic study of the effect of dose and dose rate on the ordered structure at low temperatures (23°C, 67°C and 110°C). The following two groups of irradiation were designed to study the effect of temperature on final damage structure. At each temperature, only one sample was irradiated to a dose that was high enough to obtain such saturation effect.

2. Group 2 (300°C - 550°C)

Six samples, all initially ordered, were irradiated in this

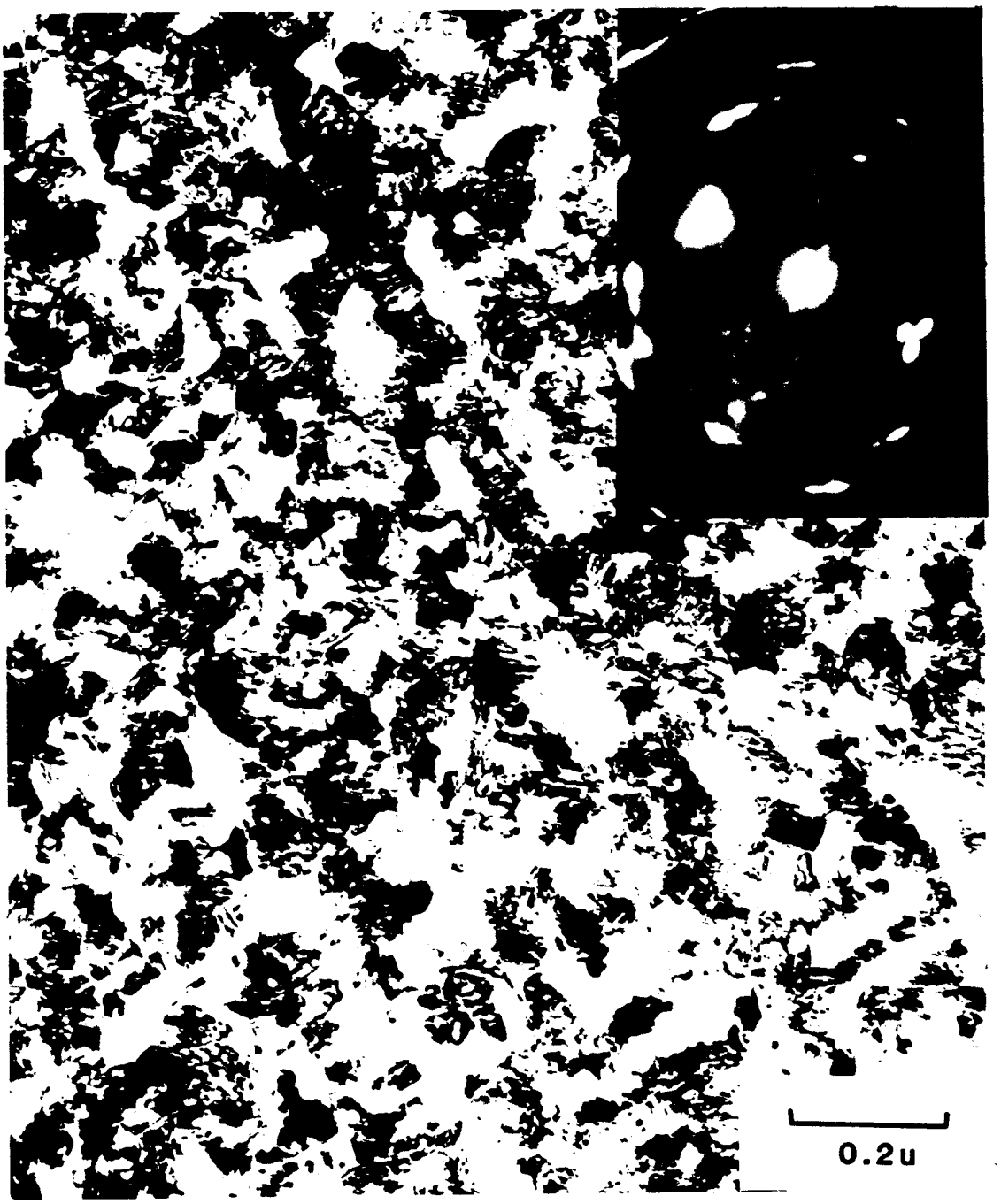

Figure VI-16. Damage structure and the diffraction pattern obtained from an initially ordered specimen irradiated at 110°C to 0.90dpa at 1.3×10^{-3}dpa/sec.

group from 300°C to 550°C in 50°C temperature steps. The upper limit of 550°C is chosen because the long range order-disorder critical transition temperature is 600°C and it is of no interest if the system is already disordered thermodynamically. 300°C is used as the lower limit because this is above the temperature at which vacancies become mobile. This is confirmed by an annealing experiment which will be discussed in the next chapter. Therefore irradiation at this particular temperature range will tell us whether a dose rate of 10^{-3} dpa/sec is high enough to disorder the alloy or the reordering rate is fast enough to reorder the damage produced.

The samples in this group were all irradiated using the high temperature holder to minimize the effect of post-irradiation annealing. Each specimen received the same dose of around 1.6 dpa at a depth of one micron. The damage rate used is about 1.4×10^{-3} dpa/sec.

All six samples have the same final structure. Figure VI-17 shows a particular set of diffraction pattern and micrograph taken from the sample irradiated at 400°C. However it is also a good representative of all the others in this group. The diffraction pattern corresponds to that of the ordered B2 phase with a [001] zone axis. The (100) superlattice as labelled in the diffraction pattern is extremely bright indicating the presence of high degree of long range order. The microstructure is relatively clean. It mainly consists of a homogeneous distribution of dislocations.

Figure VI-17. Dislocation structure and diffraction pattern representative of samples initially ordered and irradiated at 1.4×10^{-3} dpa/sec to 1.60dpa at temperatures above 300^{o}C.

some black spot damage is present which could be loops but they are too small to exhibit any dark-white contrast.

3. Group 3 (200°C - 250°C)

In this group of samples, four discs were irradiated. The irradiation parameters of these samples are listed in Table VI-2. The high temperature holder was used and therefore post-irradiation annealing was kept to a minimum.

Two initially ordered samples were irradiated at 200°C and 250°C to ∿3 dpa each at a dose rate of $\sim 10^{-3}$ dpa/sec. After irradiation at 250°C, the sample remained highly ordered and the microstructure of the material was relatively clean. It is essentially indistinguishible from those samples irradiated to similar dose at higher temperatures (group 2) (see Figure VI-17). However, when the irradiation temperature was lowered to 200°C, the material elongated disordered spots. The damage structure in this case is identical to that found at lower irradiation temperatures (group 1) to similar dose. The readers are referred to Figure VI-1 for diffraction pattern and microstructure representative of this sample.

The other two specimens in this group were also irradiated at 200°C and 250°C to 3 dpa but started out in their disordered state. Contrary to the completely different damage structure of the two initially ordered samples irradiated at 200°C and 250°C, these two initially disordered samples show identical final damage micro-

TABLE VI-2

Summary of Irradiation Parameters For Group 3

Run	Sample	Irradiation Temp (C)	Initial State (S)	Fluence 10^{15} ions/cm^2	dpa*	Dose Rate dpa/sec*	Final Damage State
6	22	250	Order	6.8	2.6	1.1×10^{-3}	Remain highly ordered Homogeneous dislocation structure.
6	23	250	Disorder	7.6	2.9	1.2×10^{-3}	Remain disordered. Black spot damage.
6	24	200	Order	7.6	2.9	1.2×10^{-3}	Completely disordered. Saturated disordered colonies.
6	25	200	Disorder	6.8	2.6	1.2×10^{-3}	Same as sample #23.

* At the region of T.E.M. analysis (~one micron from surface).

structure. Figure VI-18 shows the damage structure and diffraction pattern obtained from the initially disordered sample irradiated at 200°C. This figure is also representative of the 250°C irradiation. The diffraction pattern corresponds to that of the disordered f.c.c. phase with a $[01\bar{1}]$ zone axis. The spots are all very discrete without any elongation. The damage structure is obviously very extensive. It mainly consists of black spots and some structure similar to dislocation tangles. No sign of microtwinning or any stress effect has been observed.

4. Post-Irradiation Annealing

A post-irradiation annealing experiment was performed on two samples from group 1; sample #7 and sample #20 (Table VI-1). Both samples were initially ordered prior to irradiation. They were then irradiated to saturation dose resulting in the same disordered structure. The readers are referred to Figure VI-1 as a reference of the as-irradiated state of these samples. Annealing was carried out in an ultra high vacuum furnace and then the specimens were examined on the T.E.M. Annealing results of these two samples are identical and therefore will be presented together.

The first annealing was carried out at 230°C for ninety minutes. After this annealing, no recovery effect whatsoever was observed. The material was still completely disordered.

After annealing at 260°C for also ninety minutes, nuclei of

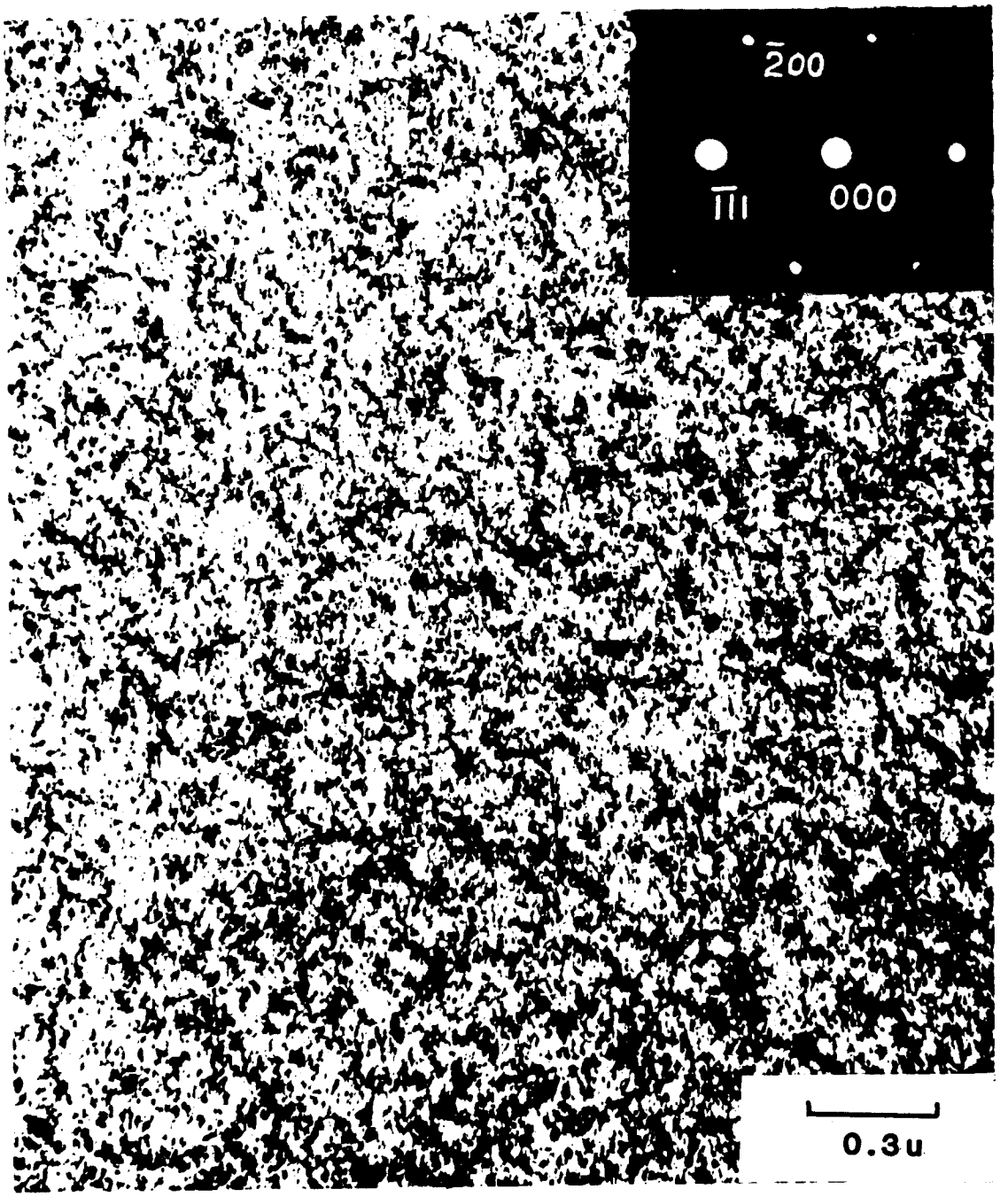

Figure VI-18. Damage structure and the diffraction pattern obtained from an initially "disordered" sample irradiated at 200°C to 2.60dpa at a rate of 1.2×10^{-3}dpa/sec.

ordered material about 0.5 microns in diameter started to form in the thicker area of the material (away from the edge of the hole). The presence of order in this transformed material was confirmed by the presence of superlattice reflection as shown in Figure VI-19. These transformed nuclei are relatively clean containing little or no damage. A sharp boundary divides the ordered (transformed) and the still disordered regions as shown in Figure VI-19. The disordered region still consists of little colonies as prior to annealing and the size of these colonies remains unchanged during annealing. The diffraction pattern from the disordered region is also unaltered. Some small nuclei of ordered material also appear in the disordered matrix (Figure VI-20). No orientation relationship can be found between the ordered nuclei and the surrounding disordered matrix as revealed by absence of any correlation between the two diffraction patterns.

Annealing at 280°C for ninety minutes resulted in a growth of the ordered (transformed) region into the thinner area (towards the edge of the hole). Again a sharp boundary is present separating the two distinctive regions.

A final annealing at 310°C for ninety minutes was performed. This annealing resulted in almost 100% conversion to ordered material. Only a small amount of material right at the edge of the hole remains untransformed as shown in Figure VI-21a. The disordered colonies that remain still have the same size as before annealing. The final ordered grain structure is shown in Figure VI-21b. These

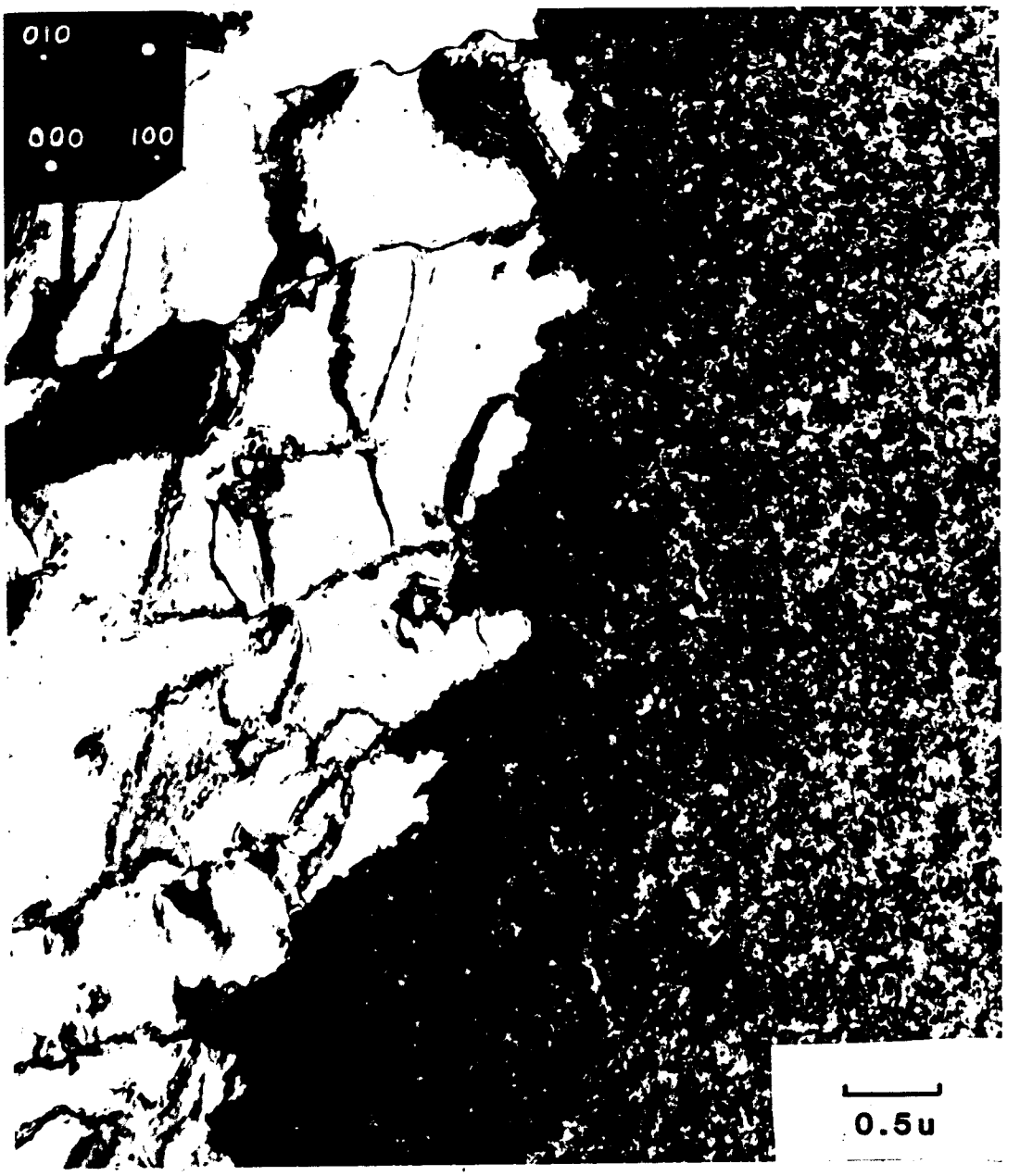

Figure VI-19. Boundary between the recrystallized ordered structure and the disordered matrix after post-irradiation annealing at 260°C for 90 minutes. The sample was initially disordered by irradiation. The inserted diffraction pattern is from the recrystallized grain.

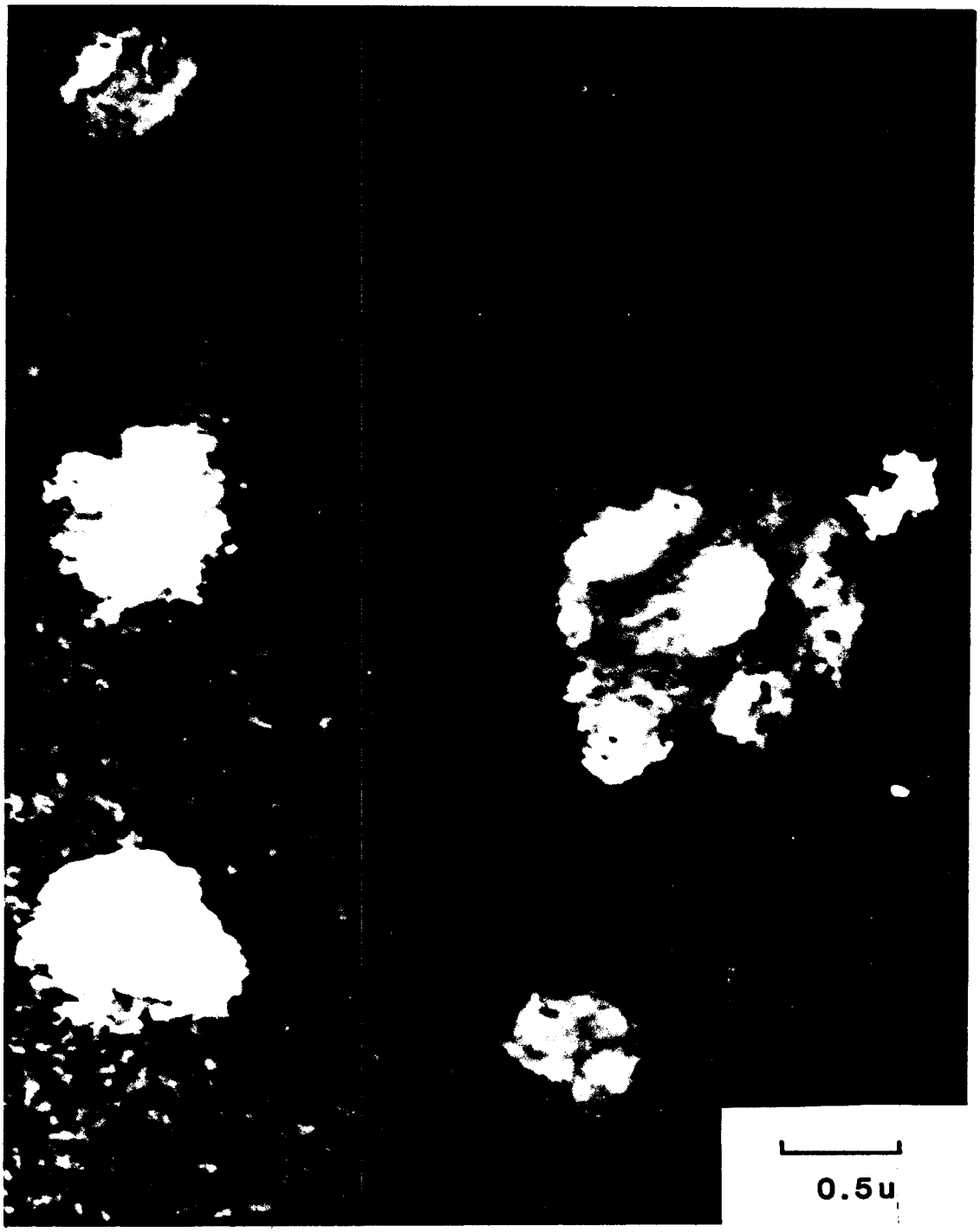

Figure VI-20. Same specimen as in figure VI-19 showing ordered grains nucleated inside the disordered matrix.

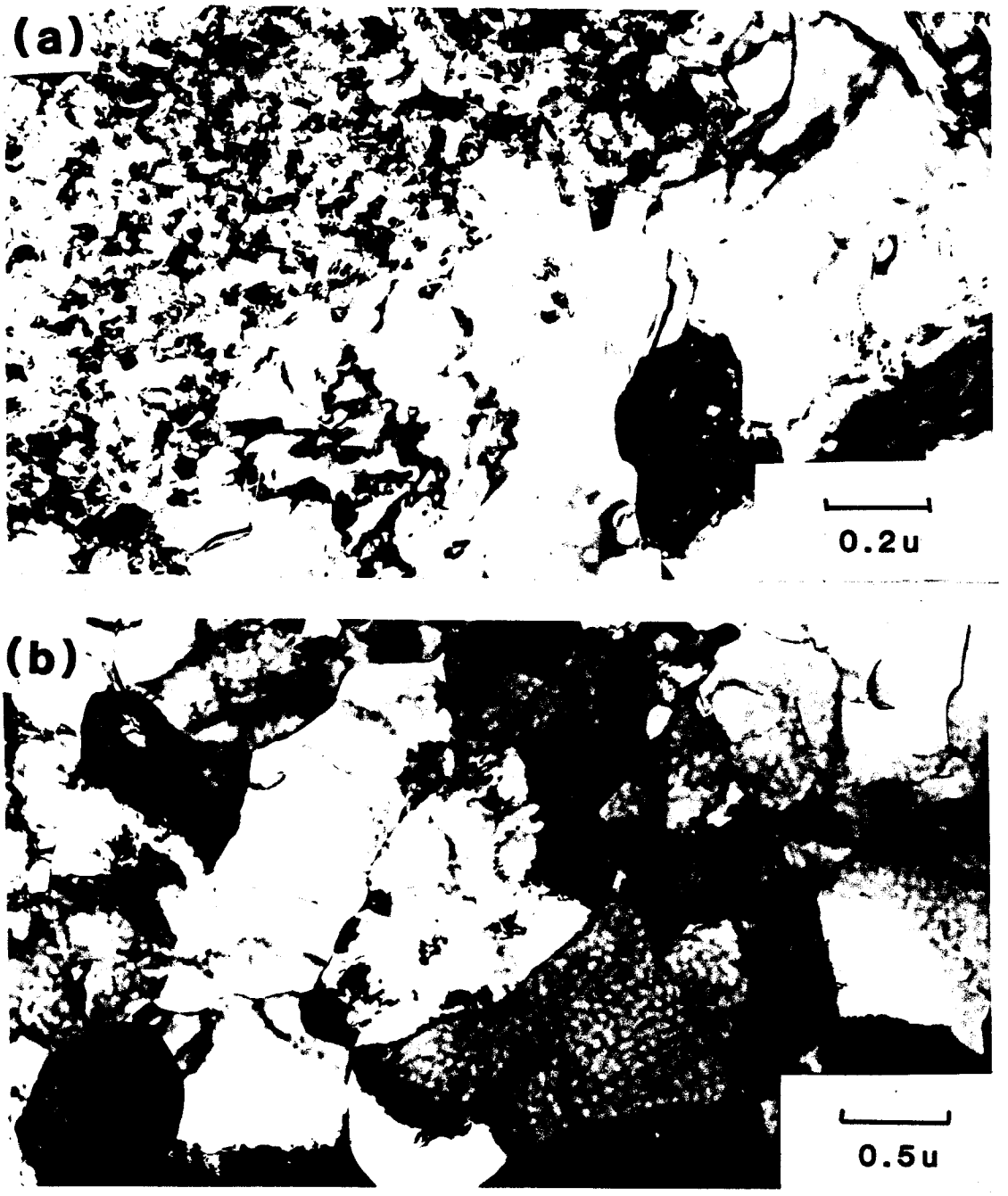

Figure VI-21. Same as figure VI-19 and 20 but after further annealing at 310°C for 90 minutes. The area in (a) is selected close to the edge of the perforation. Final ordered grain structure is shown in (b).

grains have an average size of about one micron.

B. Neutron Irradiation

Two resistivity foils, one ordered and the other disordered, were irradiated at RTNS-II with 14.8 MeV fusion neutrons at liquid helium temperature.

In Figure VI-22, the resistivity value during irradiation of an ordered foil is plotted against neutron fluence. The total neutron fluence on this sample is 1.55×10^{17} neutrons/cm^2 with an average flux of 9×10^{11} neutrons/cm^2/sec. as measured using the neutron activated niobium foils. The resistivity of the sample increases relatively linearly from 1.75 $\mu\Omega$-cm to 2.41 $\mu\Omega$-cm ($\Delta\rho_o^{ord} = 0.66\ \mu\Omega$ cm). Small discontinuities in the slope of this graph can be found at several places. They are due to interruptions of the beam either because of refilling of the liquid helium dewar or sparkings in the machine. It was not unusual for the beam to have drifted slightly after such interruption resulting in a change in neutron flux. The resistivity also increased initially due to beam heating. Before the beam was turned on, the sample temperature was 4.1°K. During irradiation, the temperature increased to 4.33°K. At about midway through the irradiation (8.5×10^{16} neutron/cm^2), a drop in resistivity was recorded (arrowed). This drop is due to a blockage in the liquid helium transfer line thus warming the cold finger up to 35°K for one minute. This mishap

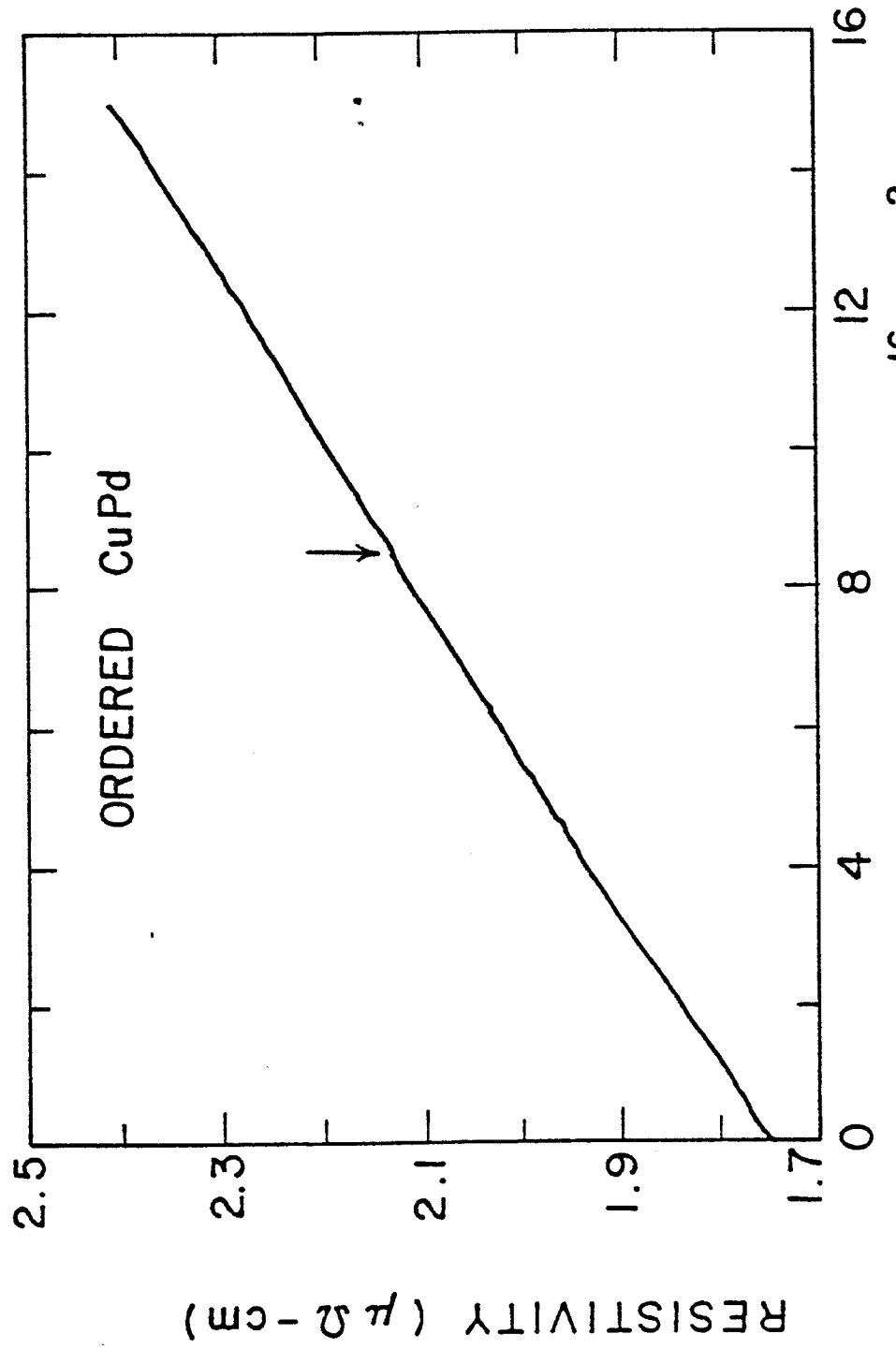

Figure VI-22. Resistivity increase in the ordered CuPd sample during 14.8 MeV neutron irradiation at 4.3°K.

annealed some of the radiation induced defects out. The slope of the curve is related directly to the damage rate in term of resistivity. This gives a value of 4.3×10^{-24} Ω-cm^3/neutron or expressed in term of percent resistivity change, 1.8×10^{-18}%/(neutron/cm^2).

In Figure VI-23, the resistivity of the disordered sample during irradiation is plotted against neutron fluence. In this sample, a total neutron fluence of 1.8×10^{17} neutrons/cm^2 was recorded. The resistivity value increased from 32.46 $\mu\Omega$-cm to 32.64$\mu\Omega$-cm ($\Delta\rho_o^{dis}$ =0.16 $\mu\Omega$-cm). This absolute increase is less than 25% of that observed in the ordered sample. The curve also exhibits an abrupt drop in the middle because of warming of the sample due to accidental blockage of the liquid helium transfer line. The sharp rise in resistivity initially is again because of beam heating. The amount of resistivity increase per neutron fluence calculated using the slope is 1.0×10^{-24} Ω cm^3/neutron (or 2.7×10^{-20}% of the initial resistivity per neutron per cm^2).

After irradiation at liquid helium temperature, both samples were subjected to isochronal annealing up to 23°C. Figure VI-24 shows such annealing result obtained from the ordered foil. The temperature increment from 4 to 40°K is 2°K, 40 to 84°K is 4°K, 84 to 150°K is 10°K and the rest is 20°K. Figure VI-25 represents a simple numerical derivative with respect to temperature of this isochronal. Only one peak is found at $\sim$35°K. The rest of the annealing is relatively continuous all the way up to room

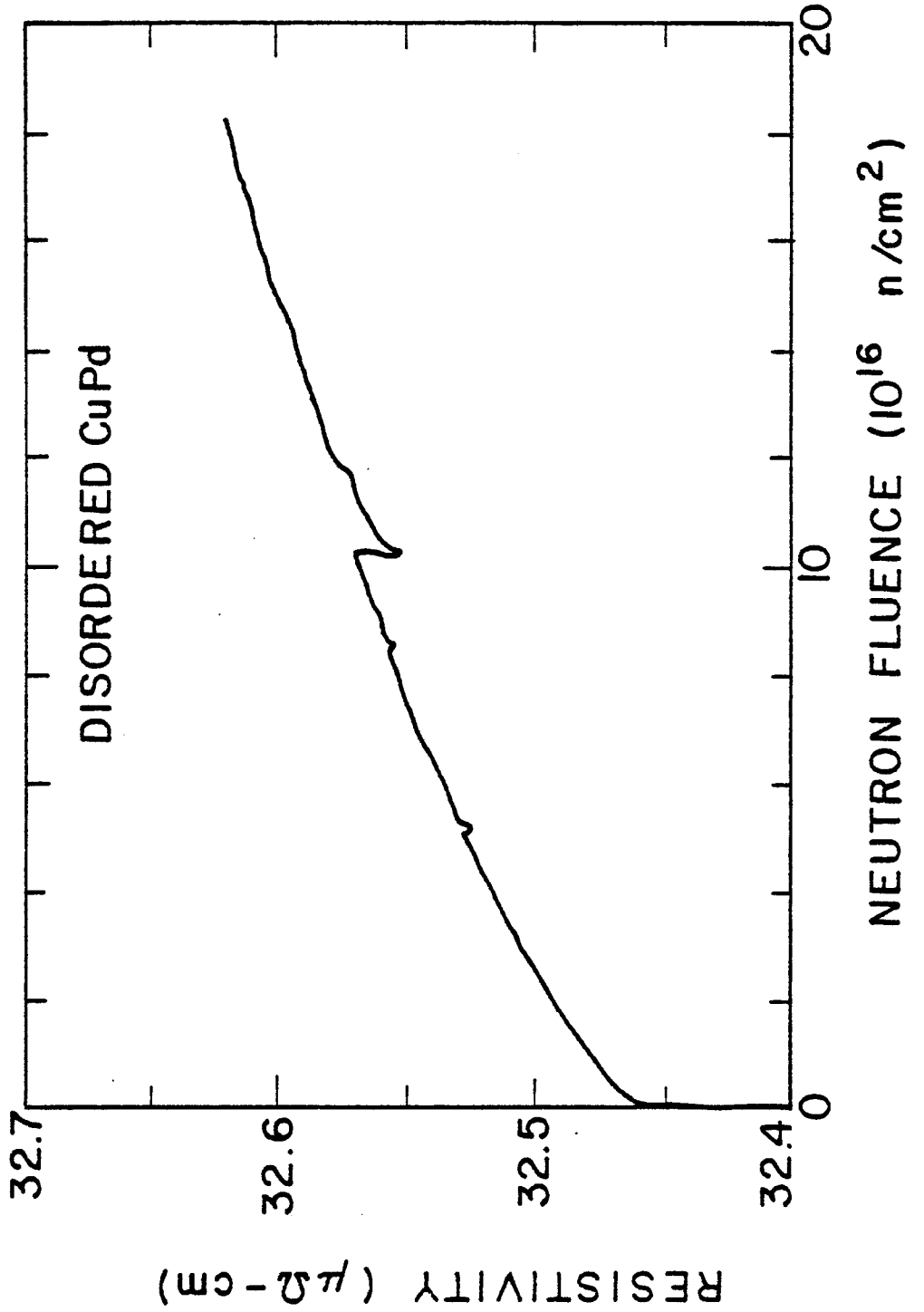

Figure VI-23. Same as figure VI-22 but for disordered CuPd sample.

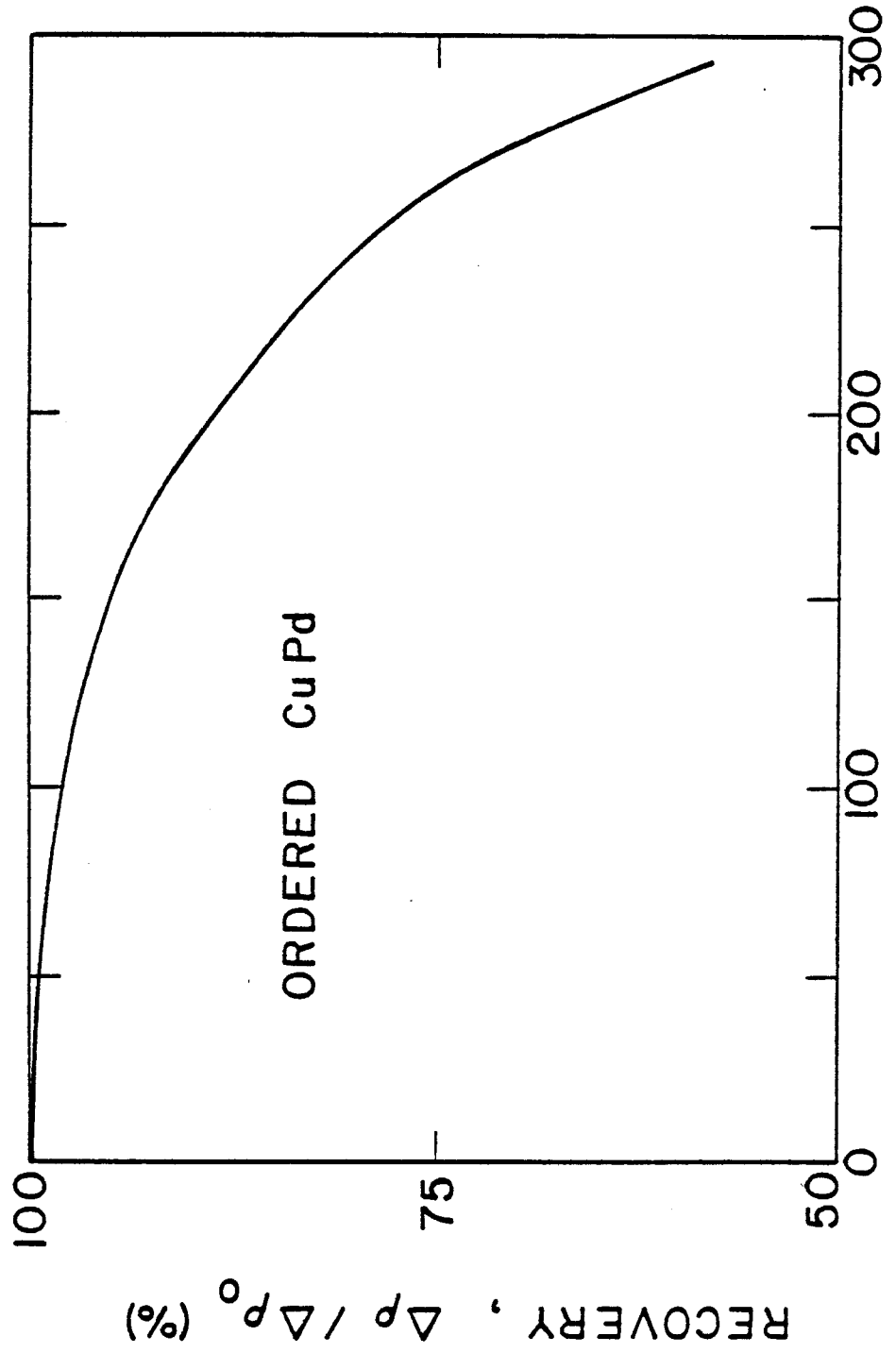

Figure VI-24. Isochronal annealing result of the ordered CuPd sample after 14.8 MeV neutron irradiation.

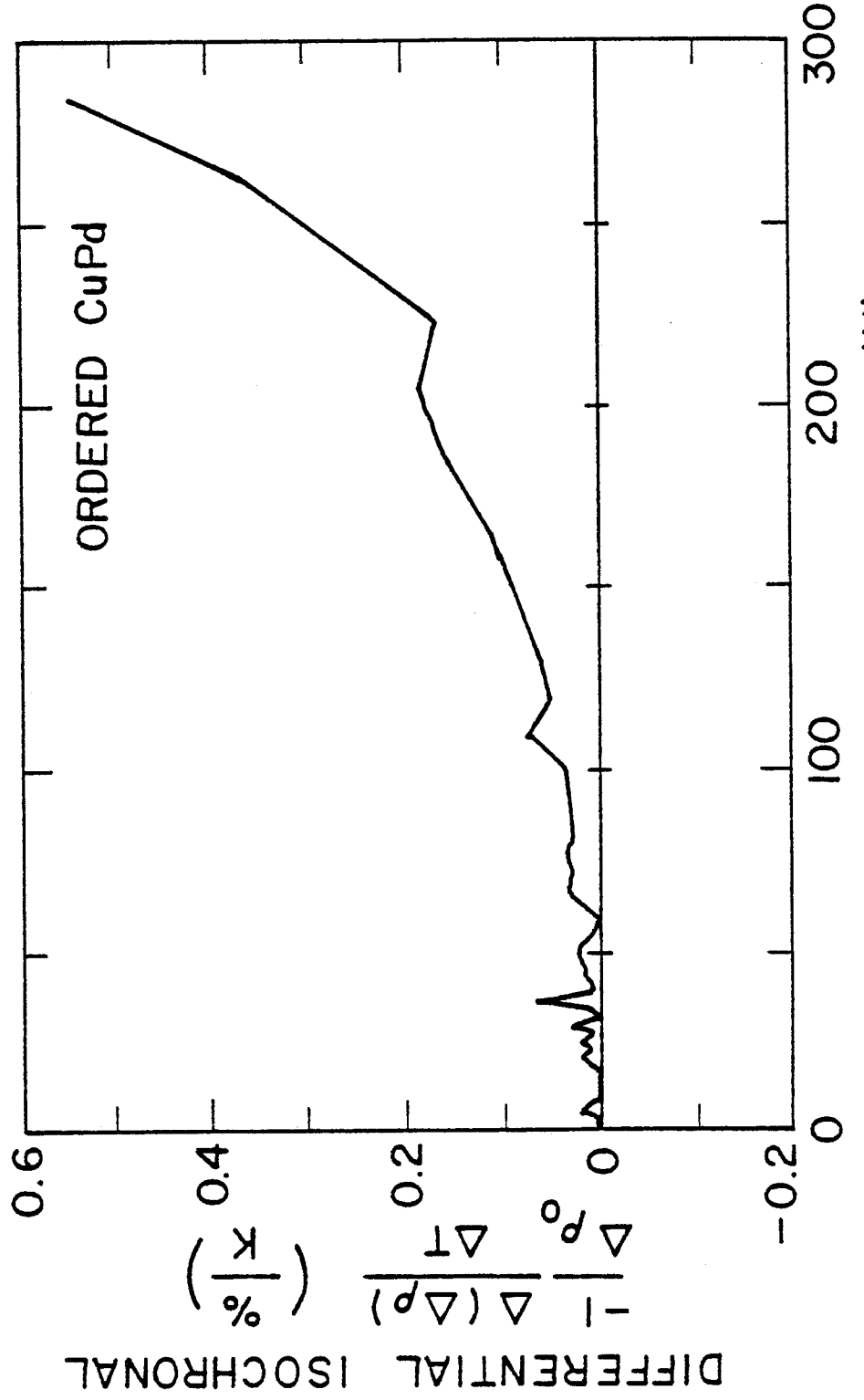

Figure VI-25. Differential isochronal result of the ordered CuPd sample.

temperature. It was found that annealing up to 100°K recovers 2% (or 0.013μΩ cm) of the radiation induced resistivity change. This increases to 16% (0.11μΩ-cm) at 220°K and 41% (0.27μΩ-cm) at 293°K.

The annealing result of the disordered sample is quite different. Figure VI-26, the isochronal curve for this sample, indicates that the resistivity first decreases with increasing temperature as expected. But at ∿ 125°K, the resistivity turns around and increases with temperature. This change is relatively linear all the way to room temperature. From 4 to 125°K, the resistivity drops by 0.075μΩ-cm which is almost 50% of the radiation induced increase. The resistivity then increases by 0.18μΩ-cm from 125 to 295°K.

Similar to the annealing spectrum of the ordered sample, the differential isochronal curve of the disordered one (Figure VI-27) also exhibits a peak at ∿35°K with a magnitude of 9%/K. Above 125°K, the derivative values become negative due to the increase in resistivity with temperature.

Six 3-mm diameter microscopy discs were also irradiated. All of them were initially ordered. They were irradiated to fluences of 4.4×10^{16}, 4.4×10^{16}, 6.5×10^{16}, 6.6×10^{16}, 9.5×10^{16} and 1.26×10^{17} neutrons/cm^2. All of them were successfully electro-polished and examined on the T.E.M. All their results are very similar and therefore will be presented together.

Their microstructure consists of mainly of heterogeneous distribution of dislocations as shown in Figure VI-28a. These

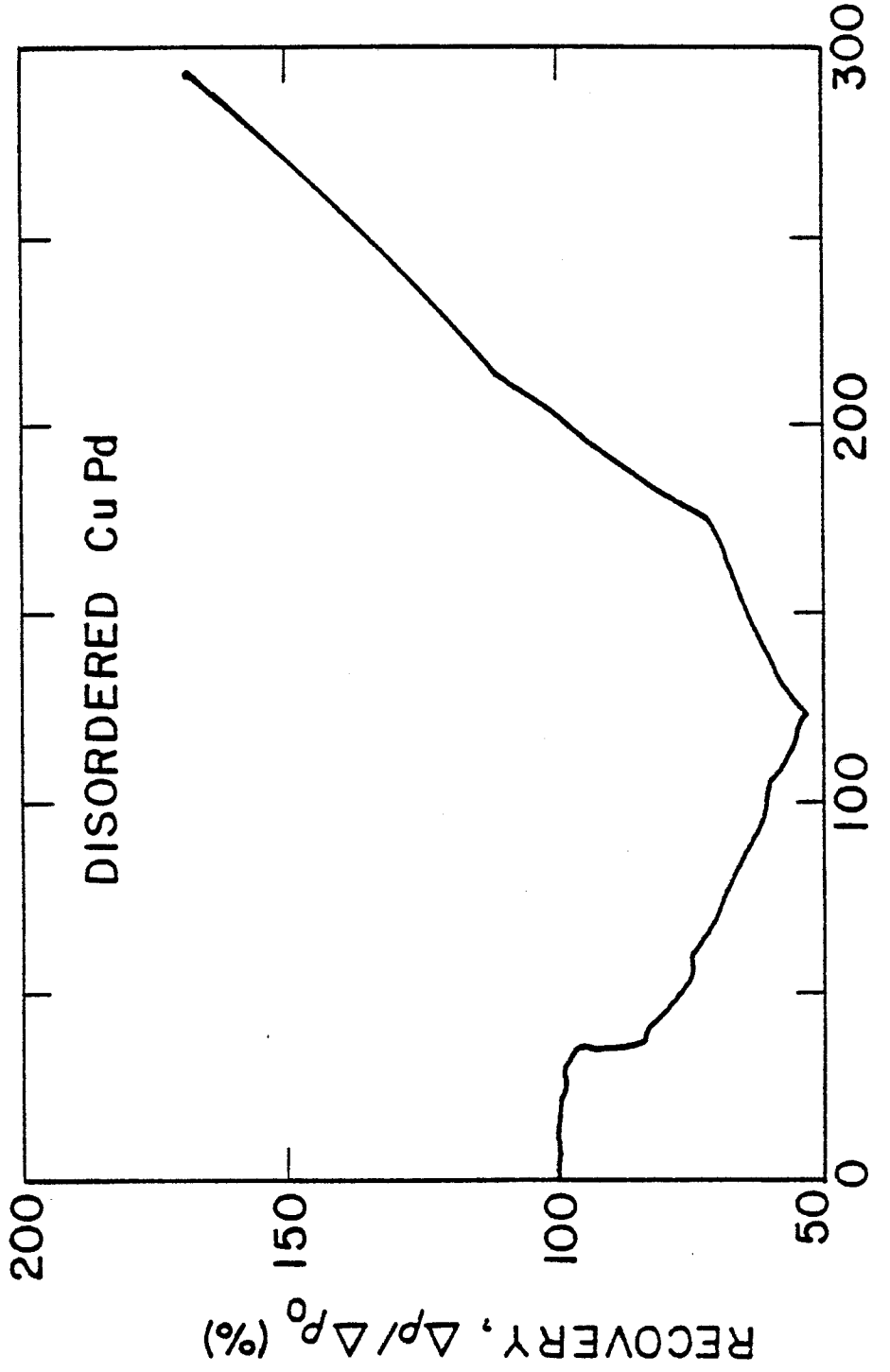

Figure VI-26. Same as figure VI-24 but for the disordered sample.

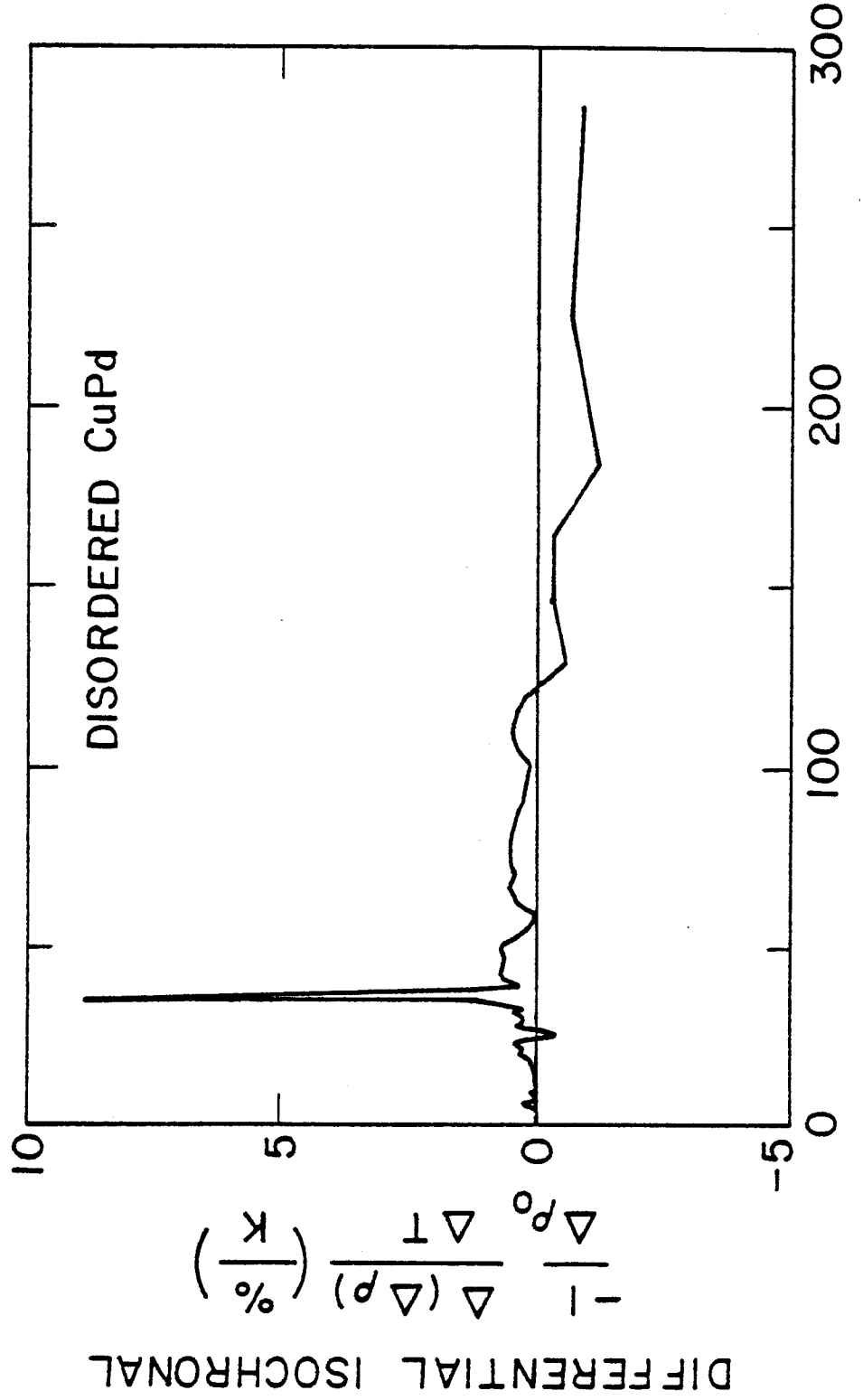

Figure VI-27. Same as figure VI-25 but for the disordered sample.

dislocations seem to pile together to form low angle tilt boundaries. Other than these dislocations, no sign of radiation damage can be detected.

The following analysis has been made to see if any radiation induced disordered zone exists in the material. In a selected area, a sequence of micrographs were taken under different diffraction conditions. Bright field images with g=200 and 110 (both fundamental reflections) together with dark field images of the same area using 100 superlattice and 200 fundamental reflections of the same area were used. A typical example of such analysis is shown in Figure VI-28b and VI-29. Figure VI-28b is a bright field micrograph with a strongly diffracting 200 beam while Figure VI-29a and b are dark field images using the (100) and (200) spots respectively. All the defects observed using the superlattice reflection can also be detected using the fundamental. Since a disordered zone can only be seen using the superlattice reflection, the above observation therefore indicates that no disordered zone exists. This, of course, is limited by the resolution of the microscope which is about 20Å.

C. Electron Irradiation

Only one ordered foil was irradiated with 1.8 MeV electrons using electrical resistivity measurement. This sample was irradiated at 100°K. Figure VI-30 shows the variation in resistivity of the sample in percent as a function of electron

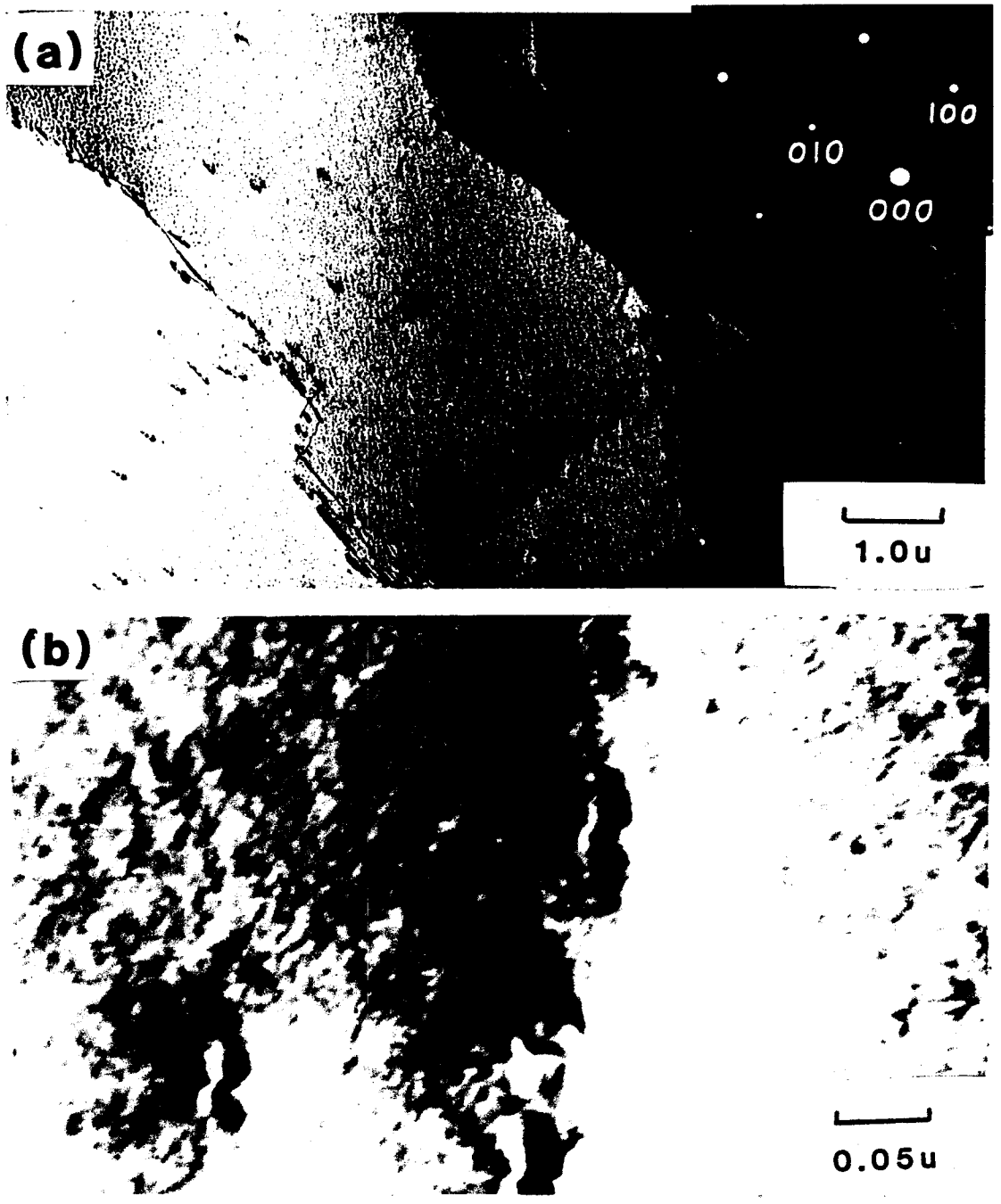

Figure VI-28. Ordered sample irradiated with 14.8MeV neutrons at 4.1°K to a fluence of 9.5×10^{16} neutrons/cm^2 but examined at 23°C showing (a) general dislocation structure and (b) a bright field image at high magnification.

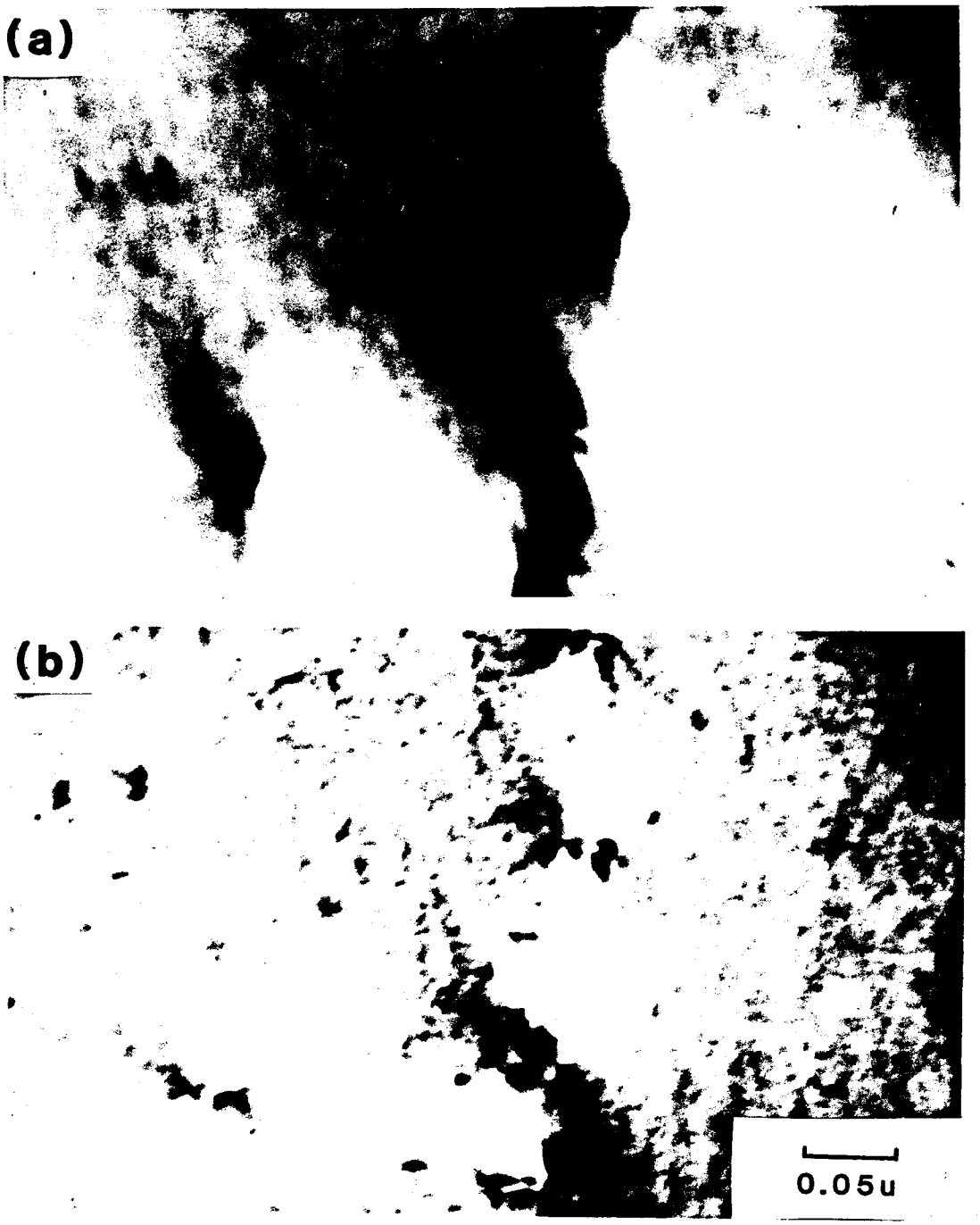

Figure VI-29. High resolution dark field images of the same area as figure VI-28b but using (a) (100) superlattice reflection and (b) (200) fundamental reflection.

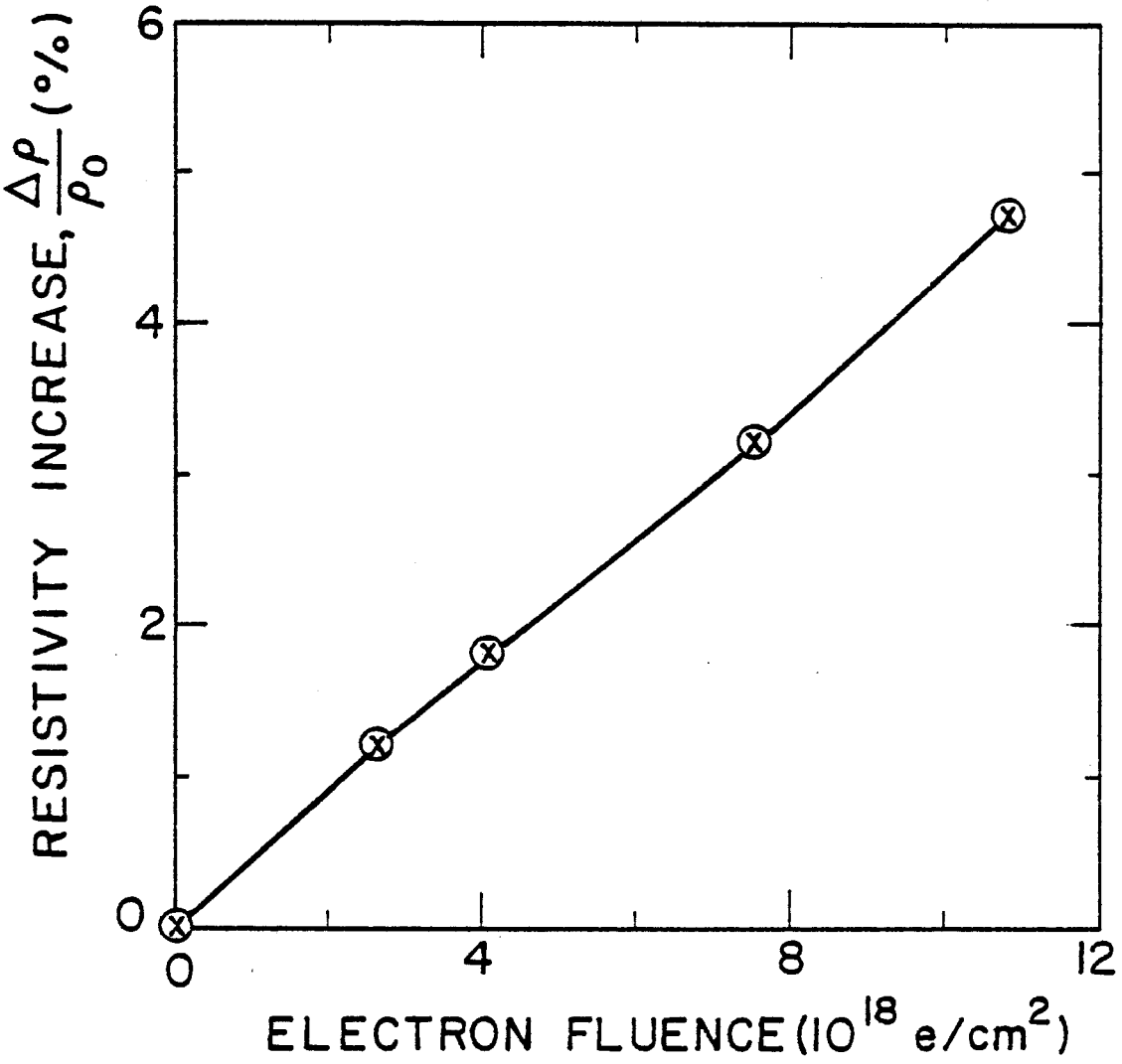

Figure VI-30. Resistivity increase (%) during 1.8 MeV electron irradiation of an ordered CuPd sample.

fluence. The absolute resistivity of the sample was not measured experimentally. However it should be very close to a similar sample irradiated at RTNS-II since they were identical initially Therefore an initial value of 2.0μΩ-cm is used for this sample. Four irradiations were performed with an integrated dose of 1.1×10^{19} electrons/cm^2. Different electron fluxes were used to insure that there was no non-recoverable beam heating effect. The linearity of the result confirms that. The change in resistivity with respect to fluence is given by the slope of this curve and is measured to be 4.3×10^{-19}%/(electron/cm^2) or 8.7×10^{-27} Ω cm^3/electron.

After irradiation, the sample was annealed at room temperature for one hundred hours. The resistivity value drops below the pre-irradiated value (> 100% recovery). Subsequent annealings at ∿50°C steps up to 200°C show continuous excess recovery as shown in Figure VI-31. The overall recovery is about 0.34μΩ-cm which is almost three times the resistivity increase due to irradiation (300% recovery). Since the temperature increment used in the annealing (50°C) is relatively large, no annealing peak can be identified.

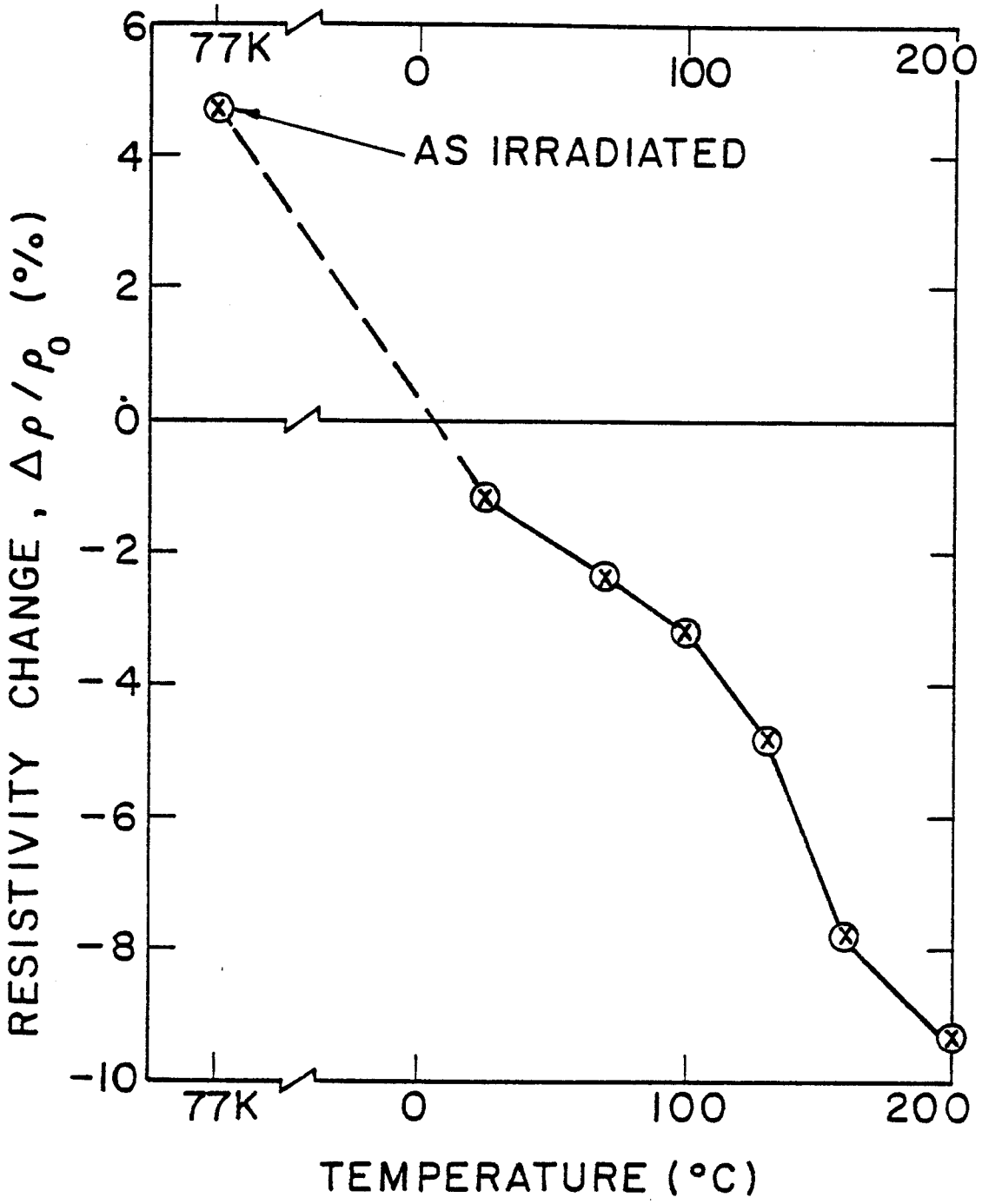

Figure VI-31. Resistivity change during post-irradiation annealing of an electron irradiated ordered CuPd sample.

VII. DISCUSSION

This chapter, as in last, is divided into three separate sections according to the type of irradiating particles. However, inter-sectional discussions will also be used when deemed appropriate.

A. Heavy Ion Irradiation

1. Radiation Disordering

In this experiment, it was found that initially ordered CuPd could be completely disordered by bombardment with 14 MeV copper ions at a rate of $\sim 10^{-3}$ dpa/sec at temperatures between 23°C and 200°C. The saturation dose for defect formation does not depend on temperature. This saturation effect occurs at less than 0.64 dpa at room temperature, 0.67 dpa at 67°C and 0.19 dpa at 110°C. This set of damage values should be treated as the upper limit for the saturation dose. A more definite value would require a more detailed dose scan at various temperatures. Since final defect saturation is established at 0.19 dpa at 110°C, this damage level could be safely regarded as the saturation fluence at temperatures below 110°C.

The damage microstructure and the diffraction pattern (see Figure VI-1), obtained from all the samples exhibiting saturation effect, are very similar. The damage structure mainly consists of a homogeneous distribution of small disordered colonies. These colonies have internal defects which resemble microtwinning

and internal faulting. The average size of these internal defects is around 30Å as revealed by the streaking of the diffraction spots and the excess spots around the center spot. The angle between a particular set of diffraction spot (spots C and D in Figure VI-2) is about 70°. High resolution dark field analysis reveals that these spots come from different diffracting sources. This 70° angle agrees very well to a twinning angle of 71° in a f.c.c. crystal with a (111) twinning plane and a $[11\bar{2}]$ twinning direction. Andrews[99] obtained a diffraction pattern very similar to that in Figure VI-4 and he showed that it was due to the existence of doubly twinned f.c.c. structure.

According to the diffraction pattern, the alloy has completely transformed from a b.c.c. ordered structure (B2) to a random f.c.c. one (A1). This suggests that irradiation under such conditions not only disorders the superlattice structure but also induces a basic crystal structure transformation. Prior to irradiation, the system is ordered because the free energy of the ordered phase is lower when compared to the disordered phase. Irradiation increases its free energy due to a decrease in S as predicted by Liou and Wilkes[87]. In this case, the shift in free energy is large enough resulting in the appearance of the disordered f.c.c. phase due to the establishment of a new balance of free energies.

Since the same saturation structure is obtained at temperatures between 23 and 200°C, diffusion by vacancies can be

assumed to play only a minor role in the disordering and phase transformation processes. This assumption is supported by the result of an annealing experiment. In this experiment, a CuPd wire was quenched from 800°C (disordered region) to 0°C. It was then annealed at different temperatures. The result of its resistance measured at annealing temperature is shown in Figure VII-1. The resistance decreases by 80% between 250 and 300°C. It is generally assumed that vacancy migration is responsible for reordering. Therefore, such a drop in resistance (increase in S) is solid evidence that vacancies do not migrate until the temperature exceeds 250°C. This result also suggests that only radiation disordering needs to be considered. This is in direct agreement with the observation that a completely disordered state can be obtained at low doses at temperatures below 250°C. Since grain boundaries are good sinks for point defects, the area around these boundaries is generally low in defect saturation if the defects are mobile. The fact that Figure VI-8 shows the homogeneity of the damage around one such boundary is also evidence of low vacancy mobility. The mechanism with which the b.c.c. phase transforms into the f.c.c. phase must therefore involve little or no thermal diffusion.

Small disordered colonies are randomly distributed throughout the entire material. These colonies are probably formed by atomic rearrangements induced by irradiation. The presence of an angular relationship of 70° between certain diffraction spots in the diffraction pattern indicates that the material

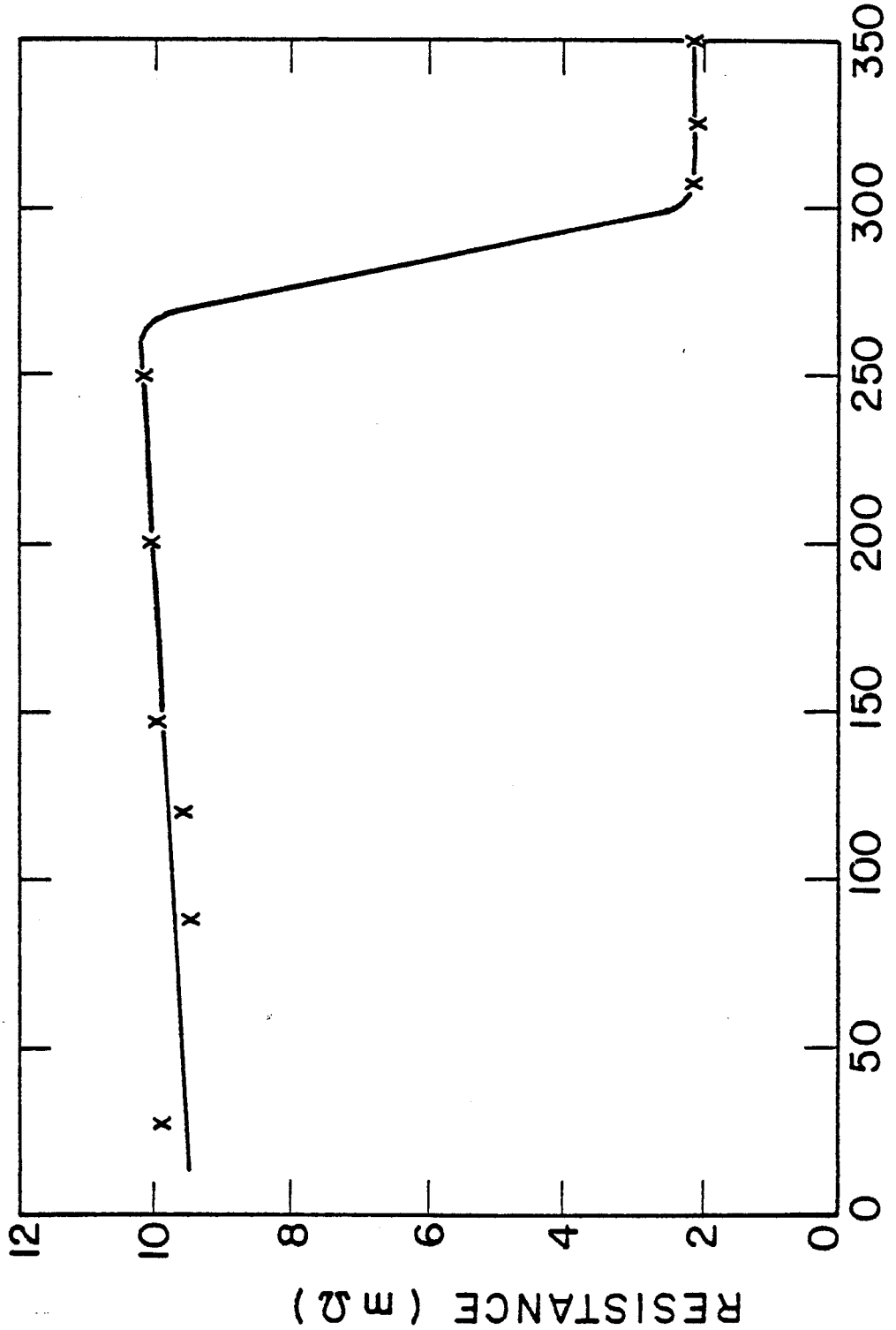

Figure VII-1. Resistance of a quenched (disordered) CuPd sample during annealing at different temperatures. (Measurement made at annealing temperatures).

is heavily twinned. These twins are formed to relieve the stress induced by the volume change associated with the phase transformation.

Three lower dose samples, 0.13 dpa at 67°C, 0.05 dpa and 0.13 dpa at 23°C, possess a mixture of ordered b.c.c. and disordered f.c.c. phases as revealed by the diffraction pattern (Figure VI-6). This diffraction pattern also shows a definite correlation between the orientation of the two phases. This means that the product phase (disordered) "remembers" the parent phase (ordered). The presence of this crystallographic correlation suggests that the ordered material is transformed into a random distribution of disordered colonies in a similar process with which semi-coherent precipitates are formed.

2. Dose Rate Effect

Most of the samples in this experiment were irradiated at a higher dose rate of $\sim 10^{-3}$ dpa/sec. Only four initially ordered samples, all at 23°C, were irradiated using a lower rate of $\sim 2 \times 10^{-4}$ dpa/sec.

The irradiation result of these four samples shows that even at this lower rate, complete disorder can be obtained at a dose as low as 0.3 dpa. The saturation dose corresponding to the higher dose rate is around 0.2 dpa as discussed earlier. Therefore, damage rate has little apparent effect, if any, on the dose required to completely disorder the superlattice system.

However, one sample irradiated to only 0.06 dpa with this lower rate (Figure VI-10 and 11) shows little sign of disordering compared to another sample irradiated to a comparable dose (0.05 dpa) but at a higher rate (Figure VI-6). This low dose, low rate sample still shows no diffraction spot corresponding to the disordered f.c.c. phase and the basic damage is just microtwins. The formation of these microtwins is probably due to the stress induced by the transformation.

At a lower dose rate, the disordering process seems to evolve slower initially. But the transformation to the disordered state seems to occur spontaneously following the initial stage.

3. High Temperature Irradiation

The irradiation results of the initially ordered samples at temperatures between 250 and 550°C show that irradiation even at rates as high as 10^{-3} dpa/sec is unable to destroy the super-lattice structure. One simple explanation for such observation is that at this temperature range, vacancies which are responsible for reordering are extremely mobile and reorder all the damage as fast as it is produced. According to Figure VII-1, vacancies are immobile in the quenched (disordered) structure until above 250°C. Yet, results here indicate that reordering rate in the ordered structure is very high at 250°C. This can be attributed to a difference in migration energies between the ordered and the

disordered structures. This phenomenon will be explored further in the following sections.

4. Irradiation Modified Phase Diagram

With the experimental results presented thus far, a new partial phase diagram for Cu-Pd system as modified by irradiation can be obtained. This is shown in Figure VII-2. This phase diagram, of course, corresponds to a damage rate of 10^{-3}dpa/sec. Due to the fact that vacancy reordering does not occur until about 250°C, the validity of this diagram can probably be extended to a lower dose rate. A very conservative estimate of this lower limit is $\sim 10^{-4}$dpa/sec since disordering has been observed at 23°C at this rate.

5. Effect of Initial State of Order

The irradiation of two initially disordered (quenched) samples shows quite unexpected results. The intention of this experiment was to determine whether irradiation can enhance reordering by generating excess vacancies. These two samples, when irradiated at 200 and 250°C, remain disordered showing that reordering is not enhanced under such conditions. However, similar irradiations were performed on two intially ordered samples. The 200°C irradiation shows that order is completely destroyed by irradiation. This final state agrees with that observed in the initially disordered

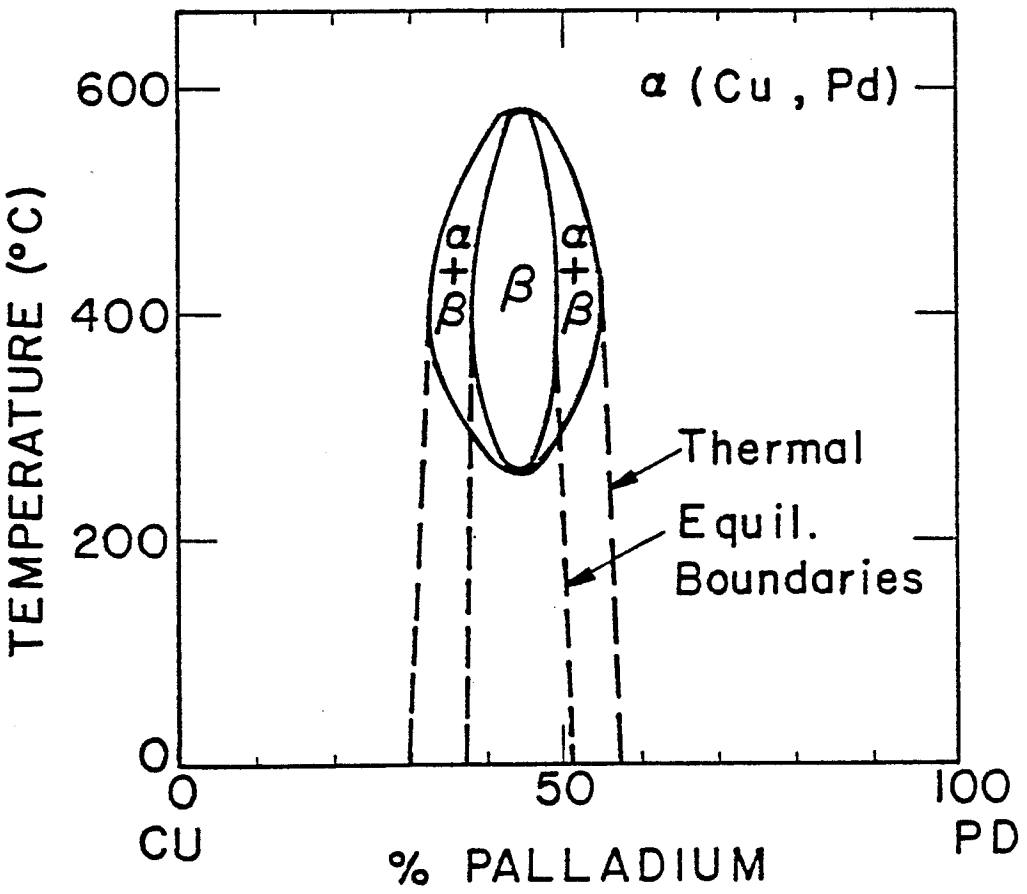

Figure VII-2. Proposed phase diagram of Cu-Od system as modified by irradiation with 14 MeV copper ions at a displacement rate of $\sim 1 \times 10^{3}$ dpa/sec. The thermal equilibrium boundaries (dashed lines) are included for comparison.

sample also irradiated at 200°C. But the result of the irradiation at 250°C of an initially ordered sample shows that this sample remains highly ordered. This means that at 250°C, the ordered sample remains highly ordered and the disordered one disordered. This is in contridiction with most models stating that irradiation should bring the state of order to a single value regardless of the initial state. However, all the models in this area do not take into account of radiation induced phase transformation which is involved in this particular CuPd system. Two explanations can be given to account for the apparent contridiction between theories and this experimental observation. First, experiments in this study have already confirmed that under irradiation the superstructure was destroyed through a crystal structure change. This requires the system to overcome a free energy barrier associated with such a transformation. At this temperature (250°C), irradiation is incapable of providing the necessary energy to overcome such a barrier. Therefore, the structure of the two samples remain unchanged.

An alternative explanation stems from vacancy migration consideration. Even though it is generally believed that the migration energy of vacancies is a function of order S such that[146] $E_m^v(S) = E_m^o(1+kS^2)$, this cannot be applied directly to this situation without further modification. In its ordered state, CuPd has a basic b.c.c. crystal structure which is more open than the disordered close-packed f.c.c. phase. Therefore, in the disordered state, a larger lattice distortion is required for vacancies to migrate or

$[E_m^V(S=0) > E_m^V(S=1)]$. So at 250°C, vacancies in the ordered phase are already very mobile resulting in such a high reordering rate that any disorder caused by irradiation is recovered instantaneously. However, at the same temperature of 250°C, vacancies in the disordered state are still immobile due to a higher migration energy. Thus the system remains random. The result of the annealing experiment shown in Figure VII-1 also indicates that vacancies in the disordered state are quite immobile until above 250°C in agreement with the proposed structure-dependent migration energy effect.

One thing worth mentioning is that the damage structure of the initially disordered sample is quite different from that of the initially ordered one even when both have zero order. The diffraction pattern of the initilly disordered sample after irradiation consists of discrete spots corresponding to the disordered f.c.c. phase (Figure VI-8). But the diffraction pattern of the initially ordered sample after disordered by irradiation (Figure VI-1) shows elongated spots. The microstructures are also quite different between them. This can be explained as follows. The initially ordered sample when disordered, is accompanied by a phase transformation. The microstructure and diffraction pattern observed in such a sample are produced by the stresses and shearings associated with such transformation. On the other hand, the initially disordered sample need not undergo such transformation resulting in a different damage structure.

Figure VII-3 is a plot of the variation in the steady state

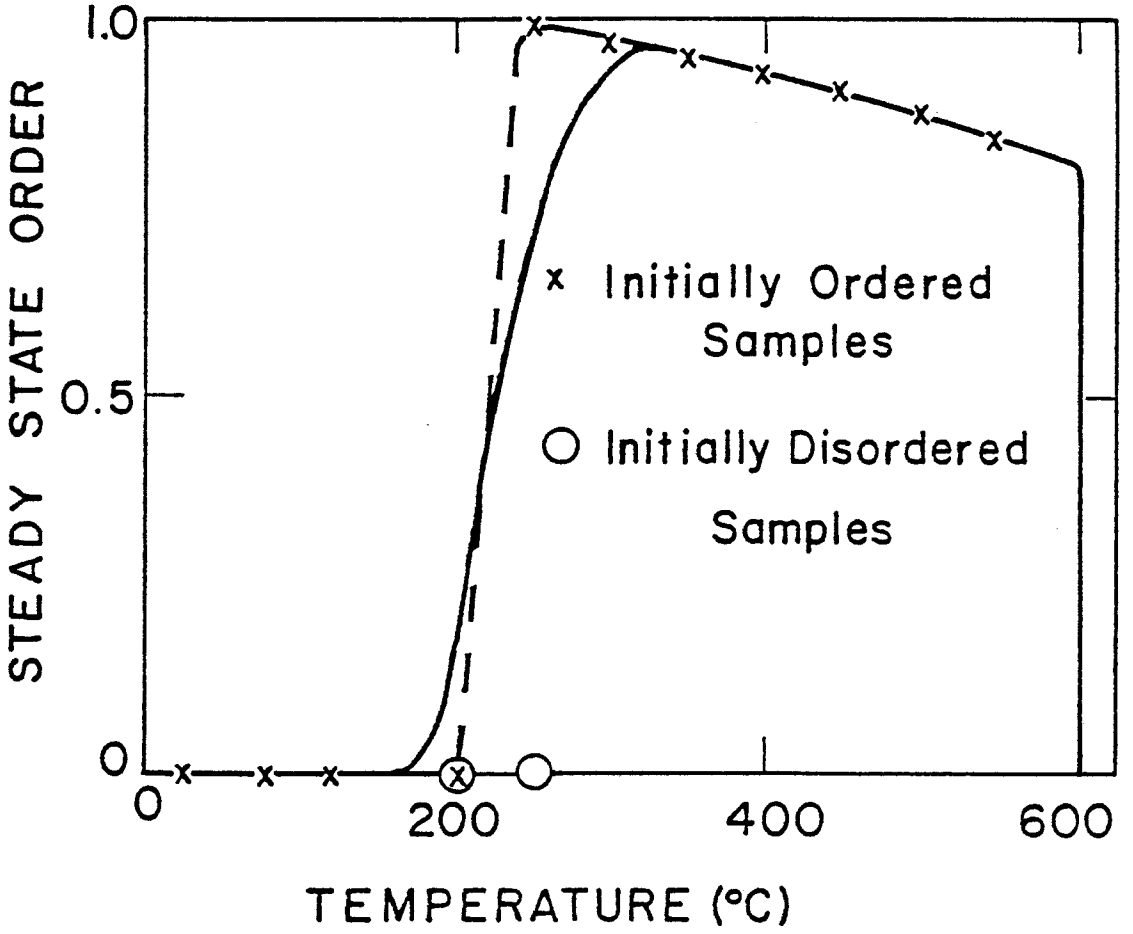

Figure VII-3. Variation of steady state degree of order in CuPd with irradiation temperature. The irradiation conditions are identical to those given in figure VII-2. The solid line represents a fit using the model described in chapter 4 using E_m^V=0.6eV.

degree of order with temperature. The crosses (+) represent data from initially ordered specimens at a damage rate of $\sim 10^{-3}$dpa/sec while the two open circles (o) are the data from the initially disordered samples. The solid line in the same figure represents a data fit to the initially ordered CuPd system using the model developed in Chapter IV. The following parameters are used in the calculation.

Vacancy migration energy	$E_m^v = 0.6$eV
Vacancy formation energy	$E_f^v = 0.9$eV
Vacancy loss fraction	$f_v = 0.95$
Ordering energy	$V_o = 0.48$eV
Displacement rate	$K = 10^{-3}$ dpa/sec.
Replacement to displacement ratio	$\varepsilon = 80$
Sink density	$\rho_d = 10^{12}/cm^2$
Coordination number	$Z_\alpha = Z_\beta = 8$
Atomic fraction	$X_A = X_B = 0.5$

Other parameters used but not listed here can be found in Table IV-1.

Even though vacancy migration energy depends on the state of order as well as the crystal structure, the experimental data obtained from ion irradiation can still be fitted successfully using a single value E_m^v of 0.6 eV as illustrated in Figure VII-3 for the following reason. At temperatures below 250°C, disordering is faster than reordering resulting in a decrease in S and a phase structure change from B2 to random f.c.c. As discussed earlier, this leads to

a higher vacancy migration energy thus reducing the vacancy ordering process even more. This simply results in an acceleration towards the S=0 state. Therefore, the vacancy motion activation energy of 0.6 eV corresponds to that of the ordered state. Also, the higher migration energy in the disordered state would not alter the steady state order shown in Figure VII-3 but would only affect the kinetic approach to this steady state.

6. Post-Irradiation Annealing

The result of the post-irradiation annealing experiment on two radiation disordered samples indicates that reordering is hetergeneous in nature. This conclusion is drawn from the formation of highly ordered nuclei in the disordered matrix (Figure VI-20). The absence of any angular correlation between the ordered grain and the disordered matrix suggests that this nucleation and growth process is similar to recrystallization. During annealing up to 310°C, the amount of transformed (ordered) region grows to almost 100%. But the size of the disordered colonies in the matrix remains unchanged (see Figure VI-21). This also can be attributed to the difference in diffusion rates of the material in its ordered and its disordered state discussed earlier.

B. Neutron Irradiation

1. Radiation Disordering

The resistivity increase in the ordered sample (Figure VI-22) irradiated with 14.8 MeV neutrons at 4.1°K is due to the production of Frenkel pairs as well as disordering. This increase in resistivity is relatively linear since the change in S is quite small and considerably below saturation. The same effect observed in the disordered sample (Figure VI-23) is however, only due to point defect production since S is already zero.

The slopes of these two curves can be used to determine the replacement (disordering) to displacement ratio. Different methods can be used to calculate this ratio. The formulation by Becker[57] will be employed here since it is one of the more thorough treatments.

A 14 MeV neutron can transfer an average energy of about 460 KeV to a copper atom and 270 KeV to a palladium atom. These high energy PKA's are capable of producing cascades. Thesefore the disordering mechanism in this case is mainly cascade mixing.

Becker divided the total observed resistivity change into two components. One is the resistivity increase due to disordering and the other due to point defect production. Using his idea, the following expression can be obtained,

$$\left(\frac{d\Delta\rho}{d\Phi t}\right)_{CuPd} = \left(\frac{dC_F}{d\Phi t}\right)_{CuPd}(\Delta\rho_F)_{CuPd} + \left(\frac{dC_R}{d\Phi t}\right)_{CuPd}(\Delta\rho_R)_{CuPd} \qquad \text{(VII-1)}$$

where $(d\Delta\rho/d\Phi t)$, $(dC_F/d\Phi t)$ and $(dC_R/d\Phi t)$ are the observed resistivity change, Frenkel pair production rate and replacement production rate respectively. $\Delta\rho_R$ and $\Delta\rho_F$ are the resistivities per atomic concentration of replacement and Frenkel pair respectively. By rearrangeing this equation, we obtain the replacement to displacement ratio C_R/C_F as

$$\frac{C_R}{C_F} = \frac{(\Delta\rho_F)}{(\Delta\rho_R)}\left[\frac{(d\Delta\rho/d\Phi t)_{CuPd}}{(d\Delta\rho/d\Phi t)_F} - 1\right] \qquad \text{(VII-2)}$$

where $(d\Delta\rho/d\Phi t)_F$ is the resistivity increase due to point defect production. The value $(d\Delta\rho/d\Phi t)_{CuPd}$ is simply the slope of Figure VI-22 and this is about 4.3×10^{-24} Ω-cm^3/neutron.

$(d\Delta\rho/d\Phi t)_F$ can be estimated by using the slope of the irradiation induced resistivity change in the disordered sample (Figure VI-23). This corresponds to $\sim1.0\times10^{-24}$ Ω-cm^3/neutron. The validity of this assumption can be shown by the following argument. Using damage energies[147,148] of 290 KeV-barn for 14 MeV neutron on copper and 230 KeV-barn for the same neutron on silver (palladium data is not available and silver is next in the periodic table), we can estimate the displacement rate, K, for fusion neutron on CuPd by taking the arithematical mean as follow,

$$K = \frac{1}{2}\{\ 290\text{KeV-barn}\left[\frac{0.8}{2\text{x}34\text{eV}}\right] + 230\text{KeV-barn}\left[\frac{0.8}{2\text{x}50\text{eV}}\right]\} \qquad \text{(VII-3)}$$

$$K = 3\text{x}10^{-21}\ \text{dpa}/(\text{n}/\text{cm}^2)$$

Here we use 34 eV for the displacement energy for copper and 50 eV for palladium. The expression in the brackets comes from the Secondary Displacement Model. The total resistivity increase in the disordered sample can be estimated by assuming that $\Delta\rho_F$ is the same in pure copper and CuPd. Using $\Delta\rho_F = 2.5\text{x}10^{-4}$ Ω-cm (obtained from copper data[149]), we obtain a rate of increase of resistivity with neutron fluence as,

$$\left(\frac{d\Delta\rho}{d\Phi t}\right)_F = K \cdot \Delta\rho_F = 0.8\text{x}10^{-24}\ \Omega\text{-cm}^3/\text{neutron} \qquad \text{(VII-4)}$$

This is in good agreement with the observed slope of the disordered sample under neutron irradiation (Figure VI-23). This agreement also indicates that the values for resistivity per unit concentration of Frenkel pairs in pure copper and CuPd are quite similar. Therefore, $\Delta\rho_F$=2.5x10^{-4} Ω-cm will be used here.

To obtain a value for the resistivity due to replacement, we use the following approach. We write the order parameter S as,

$$S = 1 - \frac{X}{X_m} \qquad \text{(VII-5)}$$

where X is the number of anti-structure atoms (A atoms on β sites) and X_m is the maximum number of such atoms. In this case, X_m=N/4 where N is the total number of atoms. Next, consider exchanging n atoms between the two sublattices (α and β) and following only the A atoms. The number of A atoms that are moved from the β to α sublattice (ordering) is 2nX/N. Similarly, n(1-2X/N) A atoms are transferred from the α to β sublattice (disordering). The net disordering, X, can be obtained by balancing the two,

$$\Delta X = n\left(1 - \frac{4X}{N}\right) \qquad \text{(VII-6)}$$

Using the definition of S and X_m, Equation VII-6 can be rewritten as,

$$\Delta X = n S \qquad \text{(VII-7)}$$

Taking the finite derivative of S with respect to S in Equation VII-5 and using equation VII-7 gives,

$$\Delta S = -\frac{4}{N} n S \qquad \text{(VII-8)}$$

But not all the replacements result in disorder. In the case of cascade mixing as the main disordering event, only half of the replacements will result in disorder giving $n=n_R/2$ where n_R is the total number of replacements including those that do not result in disorder. Therefore,

$$\Delta S = - 2 C_R S \qquad \text{(VII-9)}$$

where C_R ($=n_R/N$) is the replacement concentration.

A relationship between resistivity and order parameter is now required. Many such relationship have been obtained. In this case, due to the disordering nature of neutrons where disordered cascades are generated in an ordered matrix and the difference in crystal structure between the ordered and the disordered materials, Landauer's model would be employed. Landauer[132] considered the problem of conductivity of a body embedded with spherical islands of another homogeneous material. This Landauer's equation can be written in a differential form as,

$$dX_2 = \left(\frac{\sigma_2 + 2\sigma_1}{3\sigma_1} \right) \frac{d\sigma}{(\sigma_2 - \sigma_1)} \qquad \text{(VII-10)}$$

Here σ is the observed conductivity, σ_1 and σ_2 are the conductivities of the matrix and the islands respectively. For this application, σ_1 and σ_2 become the conductivities of the ordered and disordered materials. X_2 is the fraction of the material have conductivity σ_2. X_2 here is the same as (1 - S) . Equation VII-10 can be written in a more convenient form as

$$\Delta S = \left(\frac{\sigma_{dis} + 2\sigma_{ord}}{3\sigma_{ord}} \right) \left[\frac{\Delta\rho}{\rho^2 (\sigma_{dis} - \sigma_{ord})} \right] \qquad \text{(VII-11)}$$

σ_{ord} and σ_{dis} can be obtained from Figures VI-22 and 23 to be

0.42 $(\mu\Omega\text{-cm})^{-1}$ and 0.03 $(\mu\Omega\text{-cm})^{-1}$ respectively. Using this equation and equation VII-9, we obtain $\Delta\rho_R$ as,

$$\Delta\rho_R = \frac{\Delta\rho}{C_R} = -2S\left(\frac{\Delta\rho}{\Delta S}\right)$$

$$\Delta\rho_R = 1.12\ (\mu\Omega\text{-cm})^{-1}\ S\rho^2 \qquad \text{(VII-12)}$$

$$\Delta\rho_R \sim 6\times10^{-6}\ \Omega\text{-cm}$$

This approximation is arrived at using the assumptions that $S\sim1$ and $\rho\sim\rho_{ord}$. These assumptions are quite valid because of the low fluence involved.

Finally, substituting,

$$\Delta\rho_R = 6\times10^{-6}\ \Omega\text{-cm}$$

$$\Delta\rho_F = 2.5\times10^{-4}\ \Omega\text{-cm} \qquad \text{(VII-13)}$$

$$\left(\frac{d\Delta\rho}{d\Phi t}\right)_{CuPd} = 4.3\times10^{-24}\ \Omega\text{-cm}^3/\text{neutron}$$

$$\left(\frac{d\Delta\rho}{d\Phi t}\right)_F = 1\times10^{-24}\ \Omega\text{-cm}^3/\text{neutron}$$

into Equation VII-2, we arrived at a replacement to displacement ratio of

$$\frac{C_R}{C_F} = 140$$

This value should be interpreted with care when compared to the same ratio obtained by some other authors. Some authors define replacement as those events that actually lead to disorder. Whereas in this calculation, all replacement events are considered. If the former definition of replacement is used, then

$$\frac{C_R}{C_F} = \frac{140}{2} = 70 \qquad \text{(VII-15)}$$

This ratio of 70 is very closed to the same ratio of 80 obtained by Kirk and Blewitt[56] in their fast neutron irradiation of Cu_3Au also at 4°K. This means in terms of replacement efficiency, fast and fusion neutrons are relatively similar. Even though 14 MeV neutrons can transfer more energy to the PKA's than 1 MeV neutrons can, this extra energy is more likely to produce many sub-cascades rather then a super-cascade. This is confirmed by the T.E.M. work by English and Jenkins[106] on Cu_3Au irradiated also with 14.8 MeV neutrons where they saw sub-cascade formation.

2. Post-Irradiation Annealing

The isochronal annealing curve of the ordered sample shows only one discrete peak at ∿35°K. This peak is probably due to close-pair recombination. This, of course does not involve any reordering. After this peak, the annealing is rather gradual. A similarly smooth annealing spectrum was found by Takamuro and

Okuda[100] in fast neutron irradiated CuZn (β-brass). They assigned the annealing up to 200°K to reordering produced by interstitial migration. We propose that the same effect is seen here. The amount of recovery in CuZn after this stage is ∿60% as opposed to only ∿12% in this experiment. This is due to the size difference effect. Interstitial migration is not likely to produce reordering if the size difference between the alloy components is very large. This is because of the large amount of energy required to rotate an interstitial dumbell. The size difference between copper and zinc is 17%, between copper and palladium is 28% and between copper and gold is 48%[150]. An identical experiment[151] was performed on Cu_3Au irradiated with 14.8 MeV neutrons and then isochronally annealed up to room temperature. (This experiment was performed together with the CuPd experiment). In this Cu_3Au experiment, a broad peak was observed between 40 and 120°K (Figures VII-4 and 5). This peak is most likely due to interstitial migration. If the difference in atomic size is the main factor controlling the amount of reordering by interstitials, then the amount of recovery after stage I in Cu_3Au must be the smallest and CuZn must be the largest among the three alloys. This exact effect was observed. Up to 200°K, CuZn recovers 60%, CuPd recovers 12% and Cu_3Au only 4% of their respective induced damages.

The higher temperature annealing of CuPd (>200K) is also quite smooth with recovery of 25% in that temperature range. This high temperature recovery is due to vacancy reordering. The same

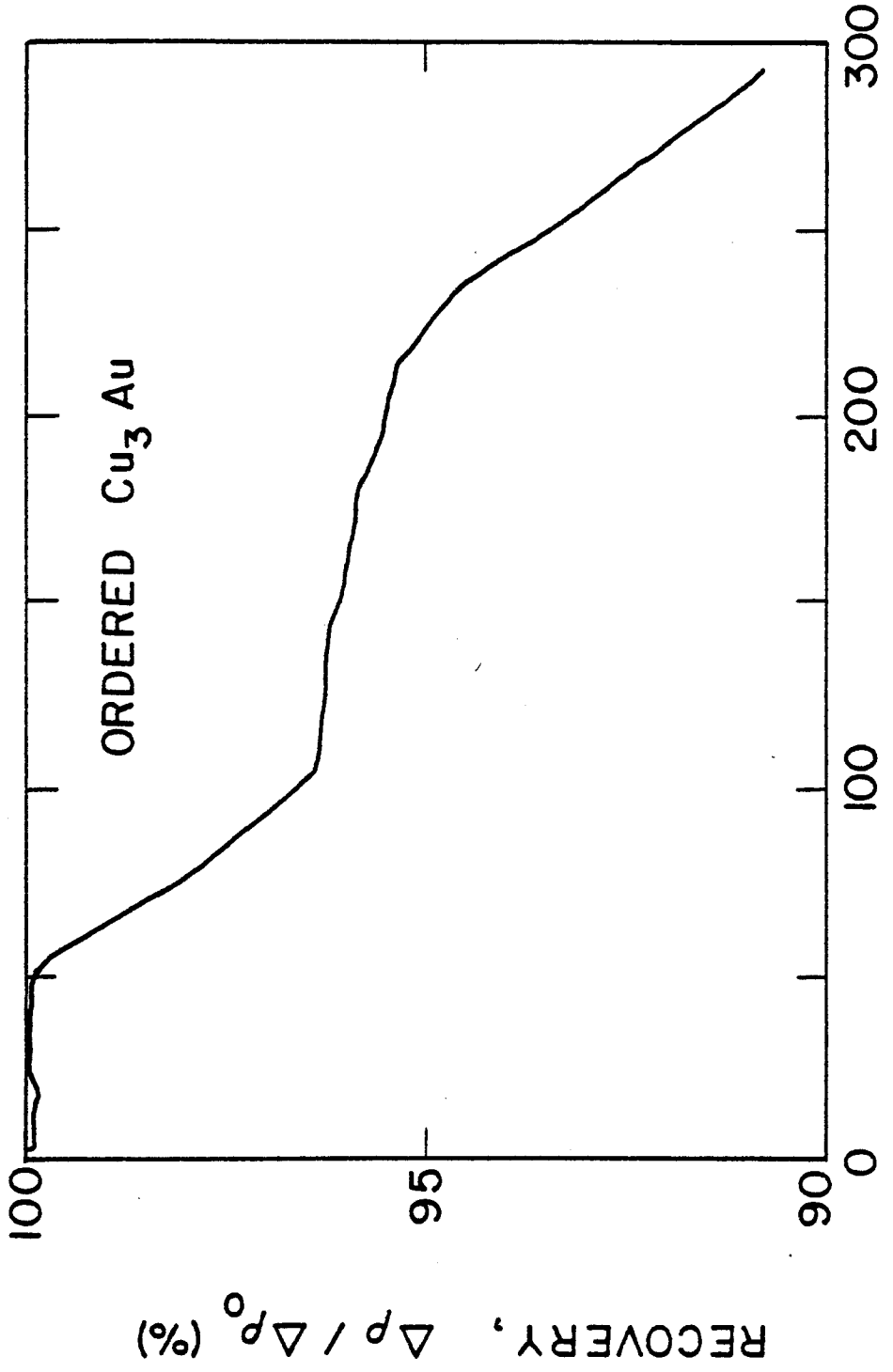

Figure VII-4. Isochronal annealing result of an ordered Cu_3Au sample after irradiated with 14.8MeV neutrons[151].

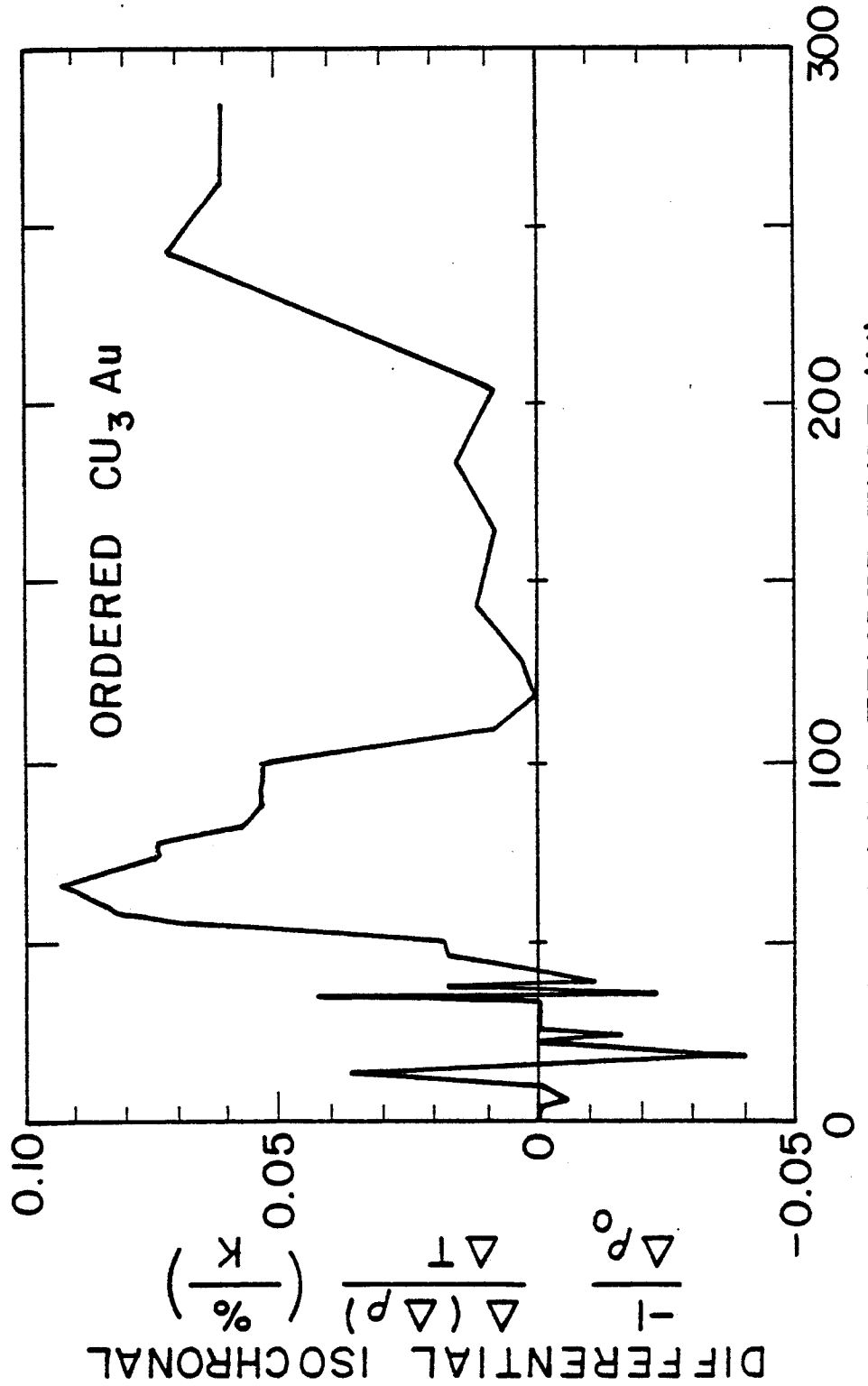

Figure VII-5. Differential isochronal annealing result of order Cu_3Au from figure VII-4.

annealing in Cu_3Au (Figure VII-4 and 5) only recovers 5% of the induced damage. This difference in amount of recovery is due to the fact that copper vacancies in Cu_3Au can migrate in the copper sublattice without doing any reordering whereas in CuPd, an α site is surrounded by all β sites (and visa versa). This latter arrangement restricts the motion of vacancies and enhances the probability of ordering by vacancy migration.

In the disordered alloy, a similar low temperature peak at $\sim$35°K is observed. This again can safely be assigned to interstitial-vacancy close-pair recombination. The annealing at higher temperatures is quite different from normal recovery. The resistivity actually increases at temperatures above 120°K. This effect, however strange is believed to be real. The ordered nuclei in the disordered matrix grow during reordering. When these ordered clusters reach an average size comparable to the wavelength of the conduction electrons in the lattice (in copper, this is about 5Å), these clusters behave as extra scattering centers thus increasing the resistivity dramatically.

3. Transmission Electron Microscopy Analysis

The result of the T.E.M. analysis on the neutron irradiated CuPd indicates that the gross order is not altered by irradiation. This is expected for such low dose irradiation and confirmed by the small amount of resistivity change due to irradiation.

Imaging with (100) superlattice reflection shows no sign

of any disordered zones (Figures VI-28 and 29). This suggests that no disordered zone larger than the resolution of the microscope ($\sim$30Å) exists. Disordered zones are found in a similar experiment on Cu_3Au by English and Jenkins[106]. However annealing experiments discussed earlier shows that the amount of recovery up to room temperature in CuPd is about four times that of Cu_3Au. The disordered zones in CuPd after annealing at room temperature are likely to have shrunk below the 30Å resolution limit of the microscope. In Cu_3Au, the average size of the disordered zones is about 50Å.

C. Electron Irradiation

1. Irradiation Disordering

The resistivity of the ordered CuPd sample increases linearly with electron fluence as shown in Figure VI-30. The rate of such increase can again be used to calculate the replacement to displacement ratio similar to that done for the neutron irradiation. Three modifications have to be considered in this case. Since electrons can only produce isolated Frenkel pairs and disorder by generating replacement collision sequences, the matrix remains quite homogeneous with little or no disordered cluster forming. Therefore, Landauer's model is not applicable. Instead, Muto's theory[131] should be employed. In this situation, we use,

$$\rho = \rho_{dis}\ (78°K) - [\ \rho_{dis}(78°K) - \rho_{ord}(78°K)\ ]\ S^2 \qquad \text{(VII-16)}$$

The values for $\sigma_{dis}(78°K)$ and $\sigma_{ord}(78°K)$ can be obtained from Figure VII-6. This figure gives the variation of an ordered and a disordered wire at different temperatures obtained experimentally. Using the same approach as in the neutron disordering calculation, we get,

$$\frac{\Delta\rho}{\Delta S}\ (\mu\Omega\text{-cm}) \sim -60\,S \qquad \text{(VII-17)}$$

The second modification is related to the fraction of replacements that actually produce disorder. Replacement sequences generally occur in specific crystallographic directions. For simplicity, we assume that these sequences only occur in the <100>, <110> and <111> directions. Of these three fundamental sequences, only the <111> type sequences will result in disorder in the B2 superlattice structure. The fraction of the <111> sequence is 4/13. We further assume that the displacement energies along all these directions are the same. Then, the fraction of replacements that will result in disorder is simply 4/13 (or $n=4/13n_R$). Equation VII-9 should therefore be modified to

$$\Delta S = -\frac{16}{13}\,C_R\,S \qquad \text{(VII-18)}$$

and Equation VII-12 becomes,

$$\Delta\rho_R = 7\text{x}10^{-5}\ \Omega\text{-cm} \qquad \text{(VII-19)}$$

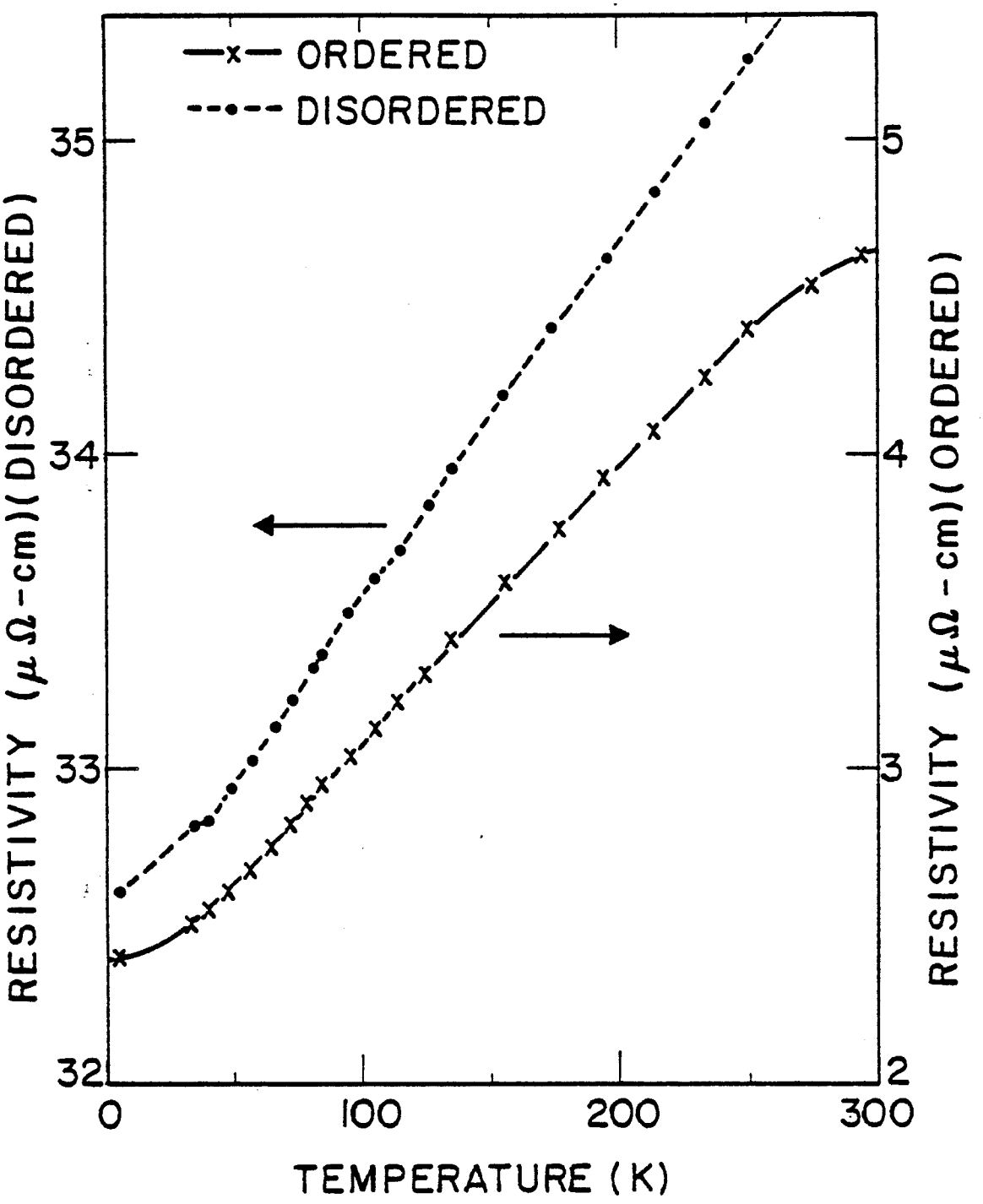

Figure VII-6. Resistivity values of an ordered and a disordered CuPd sample as a function of temperature.

A third modification is related to the irradiation temperature. At 100°K, the interstitials are quite mobile. The impurity contents in the alloy is quite high since no attempt has been made to purify the alloy. Even before melting the alloy, the pure materials contains about 100 atomic parts per million of impurity atoms and this level would become a lot higher after melting. The overall displacement produced in this irradiation is only $\sim 10^{-4}$ dpa. Therefore, it is quite likely that most if not all the interstitials produced will be trapped at impurity clusters. The addition of interstitials to these clusters has little effect on the resistivity value. So, we can express $(d\Delta\rho/d\Phi t)$ for point defect production simply as

$$\left(\frac{d\Delta\rho}{d\Phi t}\right)_F = \left(\frac{d\Delta\rho}{d\Phi t}\right)_{Vacancy} = \sigma_d \cdot \Delta\rho_v \qquad \text{(VII-20)}$$

where $\Delta\rho_v$ is the resistivity per unit concentration of vacancy and σ_d is the total displacement cross section. We express σ_d as a linear combination of displacement cross sections of copper and palladium. Using secondary displacement cross sections of 36 barns and 18 barns for copper and palladium respectively as calculated by Oen[32,33], we obtain $(d\Delta\rho/d\Phi t)Vac=4\times10^{-27}$ Ω-cm^3/electron. A value of $\Delta\rho_v=1.5\times10^{-4}$ Ω-cm is used in this calculation[152]. With the measured slope of Figure VI-30 and the parameters obtained above, we arrive at a replacement to displacement ratio of

$$\frac{C_R}{C_F} = 2.5 \qquad \text{(VII-21)}$$

This value agrees very well with 2.2±2.2 obtained by Becker[57] in electron irradiated Ni_3Mn.

2. Post-Irradiation Annealing

The post-irradiation annealing result (Figure VI-31) indicates that annealing at room temperature results in 120% recovery. This recovery increases to over 300% by 200°C. This recovery is a lot higher than that observed in the neutron irradiated sample which only recovers 40% by room temperature. A similar effect has been observed in Cu_3Au as well as CuZn. For instance, Adam and Dixon found "excess" reordering in Cu_3Au after post-electron irradiation annealing up to 130°C. Gilbert et. al[102] observed that annealing up to room temperature in an ordered Cu_3Au sample irradiated with 1.5 MeV electrons recovered over 100% whereas in a similar experiment using 14.8 MeV neutrons only recovered 10%[151]. In CuZn, Koczak[107] also found over 100% recovery in resistivity after post-electron irradiation annealing up to 180°K while Takamura and Okuda[100] found less than 50% recovery after neutron irradiation.

These effects can be explained by the difference in damage characteristics. Electrons produce isolated Frenkel pairs. At

temperatures where vacancies are mobile, they reorder the disorder sequences very effectively. But in neutron irradiation, most of the vacancies are tied up in cascades. A much higher temperature is required to detrap the vacancies from these vacancy-rich clusters. Until then, only a small fraction of these vacancies can escape to reorder the lattice.

A higher degree of order obtained after post-electron irradiation annealing (>100% recovery) is due to enhanced diffusion caused by supersaturation of vacancies induced by irradiation.

III. CONCLUSIONS

It is convenient to divide the conclusions of this work into two areas; order-disorder model and specific results on CuPd.

A. Model For Radiation Induced Order-Disorder Transformation

i) The radiation order/disorder model developed in this study has been shown to successfully fit all available data for fast and thermal neutron irradiations of Cu_3Au.

ii) The critial parameters for the model are:

E_m = 0.8 eV for vacancy motion

E_m^o = 0.84 eV for ordering vacancy jumps

The ratio of replacements to displacements, ε, is 80 for fast neutrons and 20 for thermal neutrons. For the former, a survivial rate for free vacancies is 5%, and for the latter 100%.

iii) The initial resistivity transient in the fast neutron irradiation studies of Kirk and Blewitt can be fitted by an increasing sink density. This variation allows a longer vacancy lifetime in early stages which in turn, results in excess reordering.

iv) The vacancy reordering efficiency of thermal neutron irradiation is higher in the beginning due to replacement collision sequences. The reordering rate then approaches the normal value when these sequences start overlapping.

v) Steady state degree of order can be predicted for a given set of irradiation parameters.

vi) Interpretations of experiments which measure ordering rates and then directly obtain activation energies are unreliable. The present model gives better agreement over a wider range of irradiation conditions.

B. Experimental Studies of Radiation Effect on CuPd

This systematic study of radiation effect on the order-disorder transformation in CuPd leads to the following conclusions.

i) Initially ordered CuPd can be completely disordered by 14 MeV copper ion irradiation at a displacement rate of $\sim 10^{-3}$ dpa/sec to doses as low as $\sim$0.3 dpa at temperatures below 200°C. The high disordering rate observed in this temperature range is due to low vacancy mobility.

ii) The radiation induced disordering process is accompanied by a phase change from b.c.c. to f.c.c.

iii) The disordered structure is heavily twinned in order to relieve the stress induced by the crystal structure change.

iv) The transformation from the ordered to the disordered state resembles the formation of semi-coherent precipitates.

v) Dose rate (from $\sim 10^{-4}$ to $\sim 10^{-3}$ dpa/sec) has little effect on the fluence required to disorder the superlattice system at room temperature. However, a lower dose rate does retard the initial stages of the transformation.

vi) At temperatures above 250°C, irradiation up to

$\sim$3 dpa at a displacement rate of $\sim 10^{-3}$ dpa/sec is unable to disorder the superstructure system due to rapid vacancy diffusion.

vii) At 250°C, initially ordered samples remain ordered and disordered samples remain disordered. This is probably due to difference in vacancy migration energies of the two states.

viii) Activation energy for vacancy diffusion is higher in the f.c.c. random structure than in the ordered B2 because of the difference in crystal structure. A value for the vacancy migration energy in the ordered state is found to be 0.6 eV by fitting the experimental data using the model developed in this thesis.

ix) A new partial phase diagram for the CuPd system, as modified by ion irradiation, was proposed and it revealed a reduction in the extent of the β phase.

x) Results from the post-irradiation annealing experiment show that the reordering process proceeds by classical nucleation and growth of ordered domains in the disordered matrix. This ordering process occurs at above 260°C within ninety minutes.

xi) From 14.8 MeV neutron irradiation, a value of 70 is obtained for ε, the replacement to displacement ration. The value of ε in 1.8 MeV electron irradiation is about 2.5. Both values are in good agreement with the literature.

xii) No disordered zones of size larger than 20Å or a density higher than $10^{12}/cm^3$ can be found by T.E.M. examination in the ordered CuPd samples irradiated with fusion neutrons. Disordered zones have probably been reduced below the resolution of

the microscope due to reordering.

xiii) Isochronal annealing after fusion neutron irradiation up to room temperature results in the recovery of 41% of the induced damage. It also indicates that interstitials are responsible for some reordering. When compared to other experiments, it is found that the amount of reordering caused by interstitial motion is related to the size difference factor in a reversed manner (larger size difference results in less interstitial reordering).

xiv) Isochronal annealing after electron irradiation recovers >100% of the damage at room temperature and 300% at 200°C. This recovery is much larger than that observed after neutron irradiation. This is probably due to the difference in damage characteristics, Isolated vacancies produced in electron irradiation are much more effective in reordering than the trapped vacancies in the cascades generated in neutron irradiation.

xv) A higher state of order can be obtained by annealing after electron irradiation due to radiation enhanced vacancy diffusion.

REFERENCES

1. von G. Borelius, C. H. Johansson and J. O. Linde, Ann d. Physik 86, 291 (1928).

2. von G. Borelius, C. H. Johansson and J. O. Linde, Ann d. Physik 82, 449 (1927).

3. E. Passaglia and W. F. Love, Phys. Rev. 98, 1006 (1955).

4. R. Mitchell, H. G. Paris and B. G. Leferre, Met. Trans. 4, 833 (1973).

5. L. Nowack, Zeits f. Metallkunde 22, 94 (1930).

6. E. M. Schulson, G. J. C. Carpenter and L. M. Howe, Journal of Nuclear Materials 82, 140 (1979).

7. E. M. Schulson and M. L. Swanson and S. R. Macewen, Phil. Mag. A 37 (5), 575 (1978).

8. E. M. Schulson, Journal of Nuclear Materials 66, 322 (1977).

9. G. Ischenko, H. Adrian, S. Klaumunzer, M. Lehmann, P. Muller, H. Neumuller and W. Szymczak, Phys. Rev. Lett. 39 (1) 43 (1977).

10. A. R. Sweedler, D. E. Cox and S. Moehlecke, Journal of Nuclear Materials 72, 50 (1978).

11. G. J. Dienes, Acta Met. 3, 549 (1955).

12. M. W. Thompson, Defects and Radiation Damage in Metals, (Cambridge Press) (1969).

13. P. Lucasson, Proceedings of Fundamental Aspects of Radiation Damage in Metals, Gatlinburg, TN., Oct. 1975, Vol 1, 42. CONF-751006.

14. I. M. Torrens and M. T. Robinson, Interatomic Potentials and Simulation of Lattice Defect, P. C. Gehlen, J. R. Beeler and R. I. Jaffe (eds.) Plenum Press, 423 (1972).

15. G. H. Kinchin and R. S. Pease, Reports on Progress in Physics, 18, 1 (1955).

16. D. G. Doran, J. R. Beeler, N. D. Dudey and M. J. Fluss, HEDL-TME-73-76 (1973).

17. D. G. Doran and N. J. Graves, HEDL-TME-76-70 (1976).

18. A. D. Brailsford and R. Bullough, J. Nucl. Matls. 44, 121 (1972).

19. J. Lindhard, M. Scharff and H. E. Schiott, Mat. Fys. Medd. Dan. Vid. Selsk 37,14 (1963).

20. K. B. Winterbon, P. Sigmund and J. B. Sanders, Mat. Fys. Medd. Dan. Vid. Selsk 37,14 (1970).

21. J. Lindhard and M. Scharff, Phys. Rev. 124, 128 (1961).

22. I. Manning and G. P. Mueller, Com. Phys. Comm. 7, 85 (1974).

23. J. Lindhard, V. Nelson, M. Scharff and P. L. Thompson, Mat. Fys, Medd. Dan. Vid. Selsk 33, 10 (1963).

24. M. T. Robinson, Nuclear Fusion Reactors, British Nuclear Energy Society, 410 (London 1971).

25. D. K. Brice, SAND-7500622, Sandia Lab., Albuquerque, New Mexico (1977).

26. N. F. Mott, Proc. Roy. Soc. A124, 426 (1929).

27. N. F. Mott, Proc. Roy. Soc. A135, 429 (1932).

28. N. F. Mott and H. S. W. Massey, Theory of Atomic Collision, Oxford Press.

29. P. M. Dirac, Proc. Roy. Soc. A117, 610 (1928).

30. W. McKinely and H. Feshback, Phys. Rev. 74, 1759 (1948).

31. R. M. Curr, Proc. Phys. Soc. London A68, 156 (1955).

32. O. S. Oen, ORNL-3813.

33. O. S. Oen, ORNL-4897.

34. E. C. Bain, Chem. & Met. Eng. 28, 65 (1923).

35. G. Phragmen, Stahl U. Eisen 45, 299 (1925).

36. C. H. Johansson and J. O. Linde, Ann d. Physik 78, 439 (1925).

37. Proceedings of 3rd Bolton Landing Conference on Ordered Alloys, Structural Application and Physical Metallurgy, B. H. Kear, C. T. Sims, N. S. Stoloff and J. H. Westbrook (Sept 1969).

38. Proceedings of the International Symposium on Order-Disorder Transformation in Alloys, H. Warlimont, ed., 1974.

39. J. H. Westbrook, Intermetallic Compound.

40. F. C. Nix and W. Shockley, Review of Modern Physics 10 (1), 1 (1938).

41. L. Guttman, Solid State Physics 3, 145 (1956).

42. W. L. Bragg and E. J. Williams, Roy. Soc. London A145, 699 (1934).

43. W. L. Bragg and E. J. Williams, Roy. Soc. London A151, 199 (1935).

44. H. A. Bethe, Roy. Soc. London A150, 552 (1935).

45. R. Peierls, Roy. Soc. London A154, 207 (1936).

46. J. G. Kirkwood, J. Chem. Phys. 6, 70 (1938).

47. W. Shockley, J. Chem. Phys. 6, 130 (1938).

48. F. N. Jones and C. Sykes, J. Inst. Metal 65, 419 (1939).

49. N. F. Mott, Proc. Phys. Soc. 49, 108 (1937)

50. B. R. Coles and W. Hume-Rothery, J. Inst. Metal 80, 85 (1951).

51. R. A. Oriani and W. K. Murphy, J. Phys. Chem. Solid 6, 227 (1958).

52. C. Sykes and H. Evans, J. Inst. Metal 58, 255 (1936).

53. C. Sykes and H. Wilkinson, J. Inst. Metal 61 (1937).

54. B. D. Cullity, Element of X-Ray Diffraction, Addison-Wesley Publishing Company, p383 (1978).

55. G. J. C. Carpenter and E. M. Schulson, J. Nucl. Matls 23, 180 (1978).

56. M. A. Kirk and T. H. Blewitt, Met. Trans. 9A, 1728 (1978).

57. D. Becker, F. Dworschak, C. Lehmann, K. T. Rie, H. Schuster, H. Wollenberger and J. Wurm, Phys. Stat. Sol. 30, 219 (1968).

58. T. H. Blewitt and R. Coltman, Phys. Rev 85, 384 (1952).

59. H. L. Glick, F. C. Brooks, W. F. Witzig and W. E. Johnson, Phys. Rev. 87, 1074 (1952).

60. J. Adams, A. Green and R. A. Dugdale, Phil. Mag. 43, 1216, (1952).

61. E. P. Butler and P. R. Swann, Proc. Fifth Int. Conf. on High Voltage Electron Microscopy, Kyoto, 555 (1971).

62. C. Kinoshita, T. Mukai and S. Kitajima, Proc. Fifth Int. Conf. on High Voltage Electron Microscopy, Kyoto, 551 (1971).

63. P. Okamoto and G. Thomas, Proceedings of 3rd Botlon Landing Conference on Ordered Alloys, Structure Application and Physical Metallurgy, edt. B. H. Kear, Sept 1969, p.297.

64. H. N. Southworth and B. Ralph, The Mechanism of Phase Transformations in Crystalline Solids, p.224 (1968).

65. D. W. Clegg and R. A. Buckley, Metal Science Journal 7, 48 (1973).

66. R. A. Buckley, Metal Science 9, 243 (1975).

67. M. Rajkovic and R. A. Buckley, Metal Science 15 (1), 21 (1981).

68. M. J. Marcinkowski and L. Zwell, Acta. Meta 11, 373 (1963).

69. H. C. Tong and C. M. Wayman, Acta Met. 21, 1381 (1973).

70. M. Hirabayashi and S. Weissmann, Acta Met. 10, 25 (1962).

71. G. C. Kuczynski, R. F. Hochman and M. Doyama, J. Applied Phys. 26, 871 (1955).

72. G. Lutjering and H. Warlimont, Acta Met. 12, 1460 (1964).

73. R. S. Lrani and R. W. Cahn, Metallorgr. 4, 91 (1971).

74. P. Assayag and M. Dode, C. R. Acad. Sci., Vol. 239, 762 (1954).

75. J. R. Wolfe, UCRL-7210 (1963).

76. A. S. Nowick and L. R. Weisberg, Acta Met 6, 258 (1958).

77. J. Rothstein, Phys. Rev. 94, 1429 (1954).

78. G. H. Vineyard, Phys. Rev. 102 (4), 981 (1956).

79. G. J. Dienes, J. Applied Physics 22 (8), 1020 (1951).

80. L. R. Weisberg and S. L. Quimby, Phys. Rev. 110 (2), 338 (1958).

81. M. A. Kirk and J. B. Cohen, Met. Trans. A, 7A, 307 (1976).

82. J. A. Brinkman, C. E. Dixon and C. J. Meechan, Acta Met. 2, 38 (1954).

83. P. S. Rudman, Intermetallic Compound, Chapter 21.

84. D. Turnbull, Solid State Physics 3, 226 (1956).

85. S. Siegel, Phys. Rev. 75, 1823 (1949).

86. E. M. Schulson, J. Nucl. Matls. 83, 239 (1979).

87. K. Y. Liou and P. Wilkes, J. Nucl. Matls. 87, 317 (1979).

88. R. H. Zee and P. Wilkes, Phil. Mag. A, 42 (4), 463 (1980).

89. R. H. Zee and P. Wilkes, J. Nucl. Matls. 97, 179 (1981).

90. R. H. Zee and P. Wilkes, Proceeding of the Symposium on Radiation Induced Phase Stability of the Fall Meeting of AIME, Pittsburgh, PA, 1980.

91. E. P. Butler, Rad. Eff. 42, 17 (1979).

92. E. A. Guggenheim, Mixture (Oxford Univ. Press) (1952).

93. E. A. Guggenheim and R. H. Fowler, Proc. Roy. Soc. A174, 189 (1940).

94. Y. Takagi, Proc. Phys. Math. Soc. Japan 23, 44 (1941).

95. M. L. McGlashan, Thesis, Reading University (1951).

96. R. Feder, M. Mooney and A. S. Nowick, Acta Met. 6, 266 (1958).

97. T. H. Blewitt and R. Coltman, Acta Met. 2, 549 (1954).

98. L. G. Cook and R. L. Cushing, Acta Met. 1, 539 (1953).

99. K. W. Andrew, D. J. Dyson and S. R. Keown, Interpretation of Electron Diffraction Patterns. (Adam Hilger Ltd) p. 224 (1971).

100. S. Takamura and S. Okuda, Rad. Eff. 17, 151 (1973).

101. C. E. Dixon, C. J. Meechan and J. A. Brinkman, Phil. Mag. 44, 449 (1953).

102. J. Gilbert, H. Herman and A. C. Damask, Rad. Eff. 20, 37 (1973).

103. C. E. Dixon and D. B. Bowen, Phys. Rev. 94, 1418, (1954).

104. M. L. Jenkins, K. H. Katerban and M. Wilkens, Phil. Mag. 34 (6), 1141 (1976).

105. M. L. Jenkins and M. Wilkens, Phil. Mag. 34 (6), 1155 (1976).

106. C. A. English and M. L. Jenkins, Harwell Report AERE-R9695 (1980).

107. M. J. Koczak, H. Herman and A. C. Damask, Acta Met. 19, 303 (1971).

108. R. R. Eggleston and F. E. Bowman, J. Applied Physics 24, 229 (1953).

109. W. J. Weber, Ph.D. Thesis, Univ. of Wisconsin (1977).

110. L. R. Aronin, J. Applied Physics 25, 344 (1954).

111. L. M. Howe and M. H. Rainville, J. Nucl. Matls. 68, 215 (1977).

112. L. M. Howe and M. H. Rainville, Phil. Mag. A 39 (2), 195 (1979).

113. L. M. Howe and M. H. Rainville, Rad. Eff. 48, 151 (1980).

114. R. W. Carpenter and E. A. Kenik, 35th Annual Proc. Electron Micorscopy Society Amer., p. 48 (1977).

115. R. W. Carpenter and E. A. Kenik, Proc. Fifth Int. Conf. on High Voltage Electron Microscopy, Kyoto, 577 (1977).

116. G. Van Tendelon, J. Van Landuyt and S. Amelinckx, Rad. Eff. 41, 179 (1979).

117. J. P. Riviere and J. Grilhe, Private Comm.

118. J. Pauleve, A. Chamberod, K. Krebs and A, Bourret, J. Applied Physics 39 (2), 989 (1968).

119. G. J. C. Carpenter, Private Comm.

120. B. Bethune, J. Nucl. Matls 31, 48 (1969).

121. B. Bethune, J. Nucl. Matls. 40, 205 (1971).

122. D. G. Walker, J. Nucl. Matls. 37, 48 (1970).

123. B. S. Brown, R. C. Birthcher, R. T. Kampwirth and T. H. Blewitt, J. Nucl. Matls. 72, 76 (1978).

124. A. I. Skvortsox, Y. V. Shemeljor, V. E. Klepatski and B. M. Levitski, J. Nucl. Matls. 72, 198 (1978).

125. T. L. Francavilla, B. N. Das, D. U. Gubser and R. A. Maussner, J. Nucl. Matls. 72, 203 (1978).

126. A. R. Sweedler and D. E. Cox, Phys. Rev. B 12 (1), 147 (1975).

127. V. S. Polenok, Fizkia Metall. 36, 195 (1973).

128. A. Brailsford and R. Bullough, J. Nucl. Matls. 44, 121 (1972).

129. G. Oleownik and W. Schule, Fundamental Aspects of Radiation Damage in Metals, Gatlinburg, Tn., Oct. 1975, Vol. 1, p341. CONF-751006.

130. A. C. Hindmarsh, J. D. Byrne, Numerical Methods for Differential Systems, ed. L. Lapidius and W. E. Scheisser (Academic Press) p.147.

131. T. Muto, Inst. Phys. Chem. Res. Sci. Tokyo 20, 99 (1936).

132. R. Landauer, J. Applied Physics 23, 779 (1952).

133. M. A. Kirk and T. H. Blewitt, Private Comm.

134. D. T. Keating and B. E. Warren, J. Applied Physics 22, 286 (1951).

135. N. L. Peterson, J. Nucl. Matls. 70, 3 (1978).

136. H. Wollenberger and U. Theis, J. Nucl. Matls. 88, 121 (1980).

137. M. H. Yoo and J. O. Stiegler, Phil. Mag. 36 (6), 1305 (1977).

138. N. M. Ghoneim and D. D. Cho, Phys. Stat. Sol. (a) 54, 171 (1979).

139. M. H. Yoo, J. Nucl. Matls. 68, 193 (1977).

140. P. M. Hansen, Constitution of Binary Alloys, Materials Science and Engineering Series, (McGraw Hill) 612 (1958).

141. The author would like to thank Dr. M. W. Guinan for performing the neutron irradiation at RTNS-II.

142. H. V. Smith Jr., Nucl. Inst. Method 143, 125 (1977).

143. J. H. Billen and H. T. Richards, Proc. of Symposium of Northwest Accel. Personnel, ORNL. p. 137 (1978).

144. The author would like to thank S. K. McLaurin for providing the low temperature specimen holder for this work.

145. The author would like to thank R. W. Knoll for providing the high temperature specimen holder for this work.

146. L. A. Girifalco, J. Phys. Chem. Solids 24, 323 (1964); see also Ref. 12, p. 44.

147. C. M. Logen and E. W. Russell, UCRL-52093 (1973).

148. R. A. Van Konynenburg, M. W. Guinan and J. H. Kinney, UCID-18938 (1981).

149. R. R. Coltman, C. E. Klabunde, J. K. Redman, Phys. Rev. 156 (3), 715 (1967).

150. H. W. King, J. Materials Science 1, 79 (1966).

151. M. W. Guinan, A. C. Damask, J. H. Kinney and R. A. Van Konynenburg, Private Comm. (1981).

152. F. J. Blatt, Solid State Physics 4, 322 (1957).

153. Experimenter's Guide, Rotating Target Neutron Source II Facility, LLL-M094.